POLARISED LIGHT IN CIRCULAR AND ELLIPTICAL OPTICAL FIBRES

by

Vincent Andrei Handerek B.Sc.(Eng.) A.C.G.I.

September 1982

A thesis submitted for the degree of Doctor of Philosophy of the University of London and for the Diploma of Imperial College.

Dept. of Electrical Engineering
Imperial College
London, SW7 2BT
England.

POLARISED LIGHT IN CIRCULAR AND ELLIPTICAL OPTICAL FIBRES

V. A. Handerek

Abstract

The potential application of single mode optical fibre to polarimetric sensing is investigated with special reference to Faraday Effect e.h.t. current sensors. Many 'single' mode fibres produced by CVD possess non-uniform birefringence which limits the accuracy of this sensing technique. Evidence is presented for the existence of length-dependent birefringence in double crucible drawn 'single' mode fibre also. Such fibre must be regarded as having not one, but two, fundamental modes which propagate with orthogonal polarisations. The causes of coupling of energy between these polarisations are briefly considered after the need for two new types of optical fibre is identified; the first type should be inherently isotropic for transducer applications and the second should be capable of transmitting a particular, fixed polarisation between transducers and source/detector packages.

One way of producing the second fibre type is to produce a highly birefringent fibre which suppresses coupling between the orthogonally polarised modes. Elliptically cored fibres can exhibit high birefringence due to core shape. Perturbation theory is used to show that the birefringence is proportional to the square of the index difference in these fibres. Comparison with the exact theory of elliptical dielectric waveguides supports the evidence for this relationship and also predicts the frequency dependence of the birefringence.

Tests are described for beat length, radiation pattern and mode coupling in fibres with solid elliptical cores. Liquid cored elliptical fibres were chosen to test the accuracy of the theoretical birefringence predictions because of the freedom from stress in these guides. The production technique for short lengths of hollow elliptical bore Pyrex tube is described in detail. Tests are described for both the frequency and index difference dependences of the birefringence of liquid cored fibres made from these tubes. Results are shown to be in reasonable agreement with theory.

FOREWORD

This thesis describes work which I carried out largely between October 1976 and February 1980. Since roughly mid-1979, the subject area of polarisation in 'single' and low moded fibres has enjoyed growing attention from an increasing number of research groups around the world. This growth of interest in the subject continues even now and, for completeness, I have endeavoured to integrate into this thesis the most important recent discoveries where these are directly relevant to subjects I have treated. As each chapter is relatively self-contained, references to each chapter are grouped at the end of that chapter.

It may be worth emphasising which are the more original parts of this thesis. Most importantly the idea itself for the polarisation maintaining elliptically cored fibre appeared to begin with as an attempt to explain some of my observations on double crucible drawn fibre. The measurements themselves are, to my knowledge, the only birefringence measurements which have been made on samples of this type of fibre. The observations of elliptical radiation patterns from elliptically cored fibre appearing in Chapter IV are the first example of their type ever made. The relationship of inverse proportionality between the ellipticity and peak normalised birefringence of elliptically cored fibres has not, as far as I know, been noticed or published before. Although it has only limited application, the production of controlled ellipticity single mode size tubes has not been previously achieved. The existence of these tubes made possible the production in turn of reliably stress free elliptical core fibres, and in that very important sense the optical tests described in Chapter VI are unique.

I cannot end this foreword without paying extensive tribute to the many people who helped me along the path to the production of this thesis. Professor Eric Laithwaite inspired and guided my very first steps in research work, while Professor John Brown's personal help brought me into optical fibres. Janet O'Loughlin of Chelsea College was instrumental in assisting my search for refractive index

liquids. For countless lively technical discussions, practical help and moral support I owe a great debt to fellow students Bimal Nayar, Noori Nourshagh, Sumaia Al-Shukri, Sourin Bose and Nick Whitehead. Bimal Nayar was especially helpful in providing me with major subroutines for the calculations of Chapter IV.

There is no way to express the debt I owe to Dr. John Cozens and Dick Dyott. I am very grateful for their combined support, from which I learned so very much. They also deserve very special thanks for patiently putting up with my sometimes highly eccentric ways.

Enid Mattison's battle with my manuscript under arduous conditions earns my deep gratitude. My own wife Faith's tireless effort in drawing the figures and being so understanding of my late nights is far better than I deserve.

C O N T E N T S

Contents contd.

Contents contd.

Contents contd.

LIST OF FIGURES

List of Figures contd.

List of Figures contd.

LIST OF TABLES

CHAPTER I

COMMUNICATION AND MEASUREMENT BY OPTICAL FIBRES CARRYING POLARISED LIGHT

This chapter begins by surveying the possible uses of guided, polarised light in optical communication and instrumentation. A detailed study is then made of the use of the Faraday Effect EHT current monitor. From this study, conclusions are drawn regarding the utility of particular types of optical fibre in polarisation sensitive applications. Finally, the usefulness of such fibres is illustrated by a proposal for their employment in a new design for a Faraday monitor.

1.1. The importance of polarised light to optical communication

Existing optical fibres possess some unique advantages for the transmission of information. Their immunity to electrical interference and lack of stray field make them prime candidates for secure communication systems. In addition, the optical link provides complete electrical isolation between stations and the light output from fibres is unlikely to drastically interfere with the fibre's immediate surroundings. This makes the optical fibre useful for taking signals into and out of potentially hazardous environments.

Some of these considerations can alone dictate the use of optical fibres for communication as, for example, in aircraft, military vehicles and chemical works. However, suitably designed fibres possess yet another advantage over electrical cable communication. This lies in their potential bandwidth. Early fibres of the step index multimode variety could not compete with good coaxial cable links for transmission distances measured in kilometres. But today, with graded index fibre and semiconductor laser light sources, optical links with performance comparable to coaxial systems are operating commercially.

The situation is amenable to further development, since advances can be expected in both sources and fibres, but present commercial aims seem to lie at systems operating at 140 Mbits per second information rate with repeater spacings of up to 9 km[1]. The bandwidth limit is set at present by the waveguide dispersion characteristics. Typically 1 ns/km pulse broadening is attainable with graded index fibre, and this in turn is limited by the accuracy with which the refractive index of the core can be graded[28].

To gain a significant improvement in bandwidth, it is very likely that single mode fibre will be used. This is partly because of the widely expected difficulty in improving graded index fibre manufacturing techniques; the use of single mode fibre may well provide a very dramatic improvement in performance with less technical development effort. It has been estimated[2] that single mode guides could offer an improvement of between ten and a hundred times the information rate possible with current fibre optic systems. A further advantage of single mode communication is that it would facilitate totally optical methods of signal processing on 'integrated optics' chips by improving the coupling of light from fibres onto these chips, which themselves normally operate in the single mode condition.

It is in the latter respect that polarisation of light becomes important. Since integrated optics devices are of rectangular design and function correctly for only one polarisation, an unpolarised light input would need to be polarised by filtering before launching, thus suffering a 3 dB attenuation on coupling into an integrated optics chip. Since present losses for fibre optic cables are about 0.5 dB/km, this would necessitate a considerable cut in repeater station spacing in cases where loss is the limiting factor in the system.

Another application of optical fibres where polarisation behaviour is a limiting factor is the possible use of fibres themselves as light sources. Optical fibre Raman oscillators have been built[20] and have also been proposed as aids in assessment of materials and devices for integrated optics. In addition, they are useful tools for investigation of the fibres themselves. However, unless

polarisation can be maintained over long lengths in such fibres, the optical gain can be cut by as much as 3 dB, thus raising the oscillation threshold. This occurs because the pumping and stimulated fields should have the same polarisation for efficient amplification of the stimulated field[33].

1.2 Polarisation sensitive applications of optical fibres to instrumentation

Quite apart from telecommunications, there is another field of application for optical fibres in the world of measurement. Optical fibres have already extended optical observation of events in previously inaccessible areas by providing remote imaging and recently by facilitating use of Doppler techniques[34]. If it were possible to preserve a single phase velocity of light in a guide, the range of remote measurements could be extended to include remote interferometry and polarimetry. Unfortunately, the phase velocity of light in existing guides is polarisation sensitive, both because of the inherent characteristics of practical fibres and because of the influences which affect them in practical applications. Both of these aspects will be examined more fully in later chapters.

Despite these problems, several attempts to extend the range of fibre optic measurements to interferometry have already been made. The case where polarisation is not changing with time (but may change with position along the fibre) is simplest and has been used to produce a fibre ring interferometer or 'laser gyroscope'[3,4] and also a strain gauge and an interferometric acoustic sensor[5]. Work is also in progress to develop techniques for remote holography[35], but all these instruments are reported to be severely affected by vibrations and general movement of the fibre used, these influences causing variations in the output of the devices.

In the medical field, it is possible that polarisation preserving fibres might be useful as an aid for the diagnosis of, for instance, arthritis in joints. It has been proposed that such fibres might be used in vivo for reflection polarimetry of the small birefringent crystals which are a symptom of the disease.

For reasons which will be dealt with in detail later, the problems of using interferometric and polarisation sensitive techniques become far worse when the polarisation state at a point in the guide is not static. Considerable attention has recently been given to the investigation of applications where this is the case. In particular, the original aim of this project was to investigate the feasibility of using optical fibres as the transmission and sensor medium for a current-measuring system employing the Faraday magneto-optic effect.

Such a device poses many problems of manufacture, but also offers great potential advantages when compared with existing current measurement systems in electrical power distribution networks. The following sections describe the reasons for attempting to build a Faraday Effect current monitor and identify the problems associated with the construction and operation of these instruments. The application is explored here in detail as a case study because it involves most of the major advantages and disadvantages connected with using optical fibres to guide polarised light in a real application.

1.3 Case Study: Faraday Effect measurement of electric current

1.3.1 EHT current transformers

At present, current measurement in EHT power distribution systems is made by the use of current transformers. A typical specification for such a transformer is shown below:

CONSTRUCTION: Iron cored single phase transformer

OPERATING VOLTAGES: (i) Primary coil: at system operating voltage. Anything from 0 - 1500 kV.

(ii) Secondary coil: at or near ground potential.

CURRENT RATING: Short term rating is set by inter-conductor force during maximum fault currents. On a large system, this can be > 150 kA and is often 80 - 100 x rated continuous current.

ACCURACY: Amplitude error ± 0.3 - 0.6% for metering from 10% up to 120% continuous rated current. Phase error < 20° for same range. ± 10% for protection at maximum fault levels.

TEMPERATURE RANGE: In Great Britain -25°C to +45° C but in foreign lands much wider variations must be accommodated. For example, Canadian Standards require operation between -55°C and +55° C.

FREQUENCY RESPONSE: For simple metering 1 kHz is adequate. For protection and fault diagnostics d.c. to 10 MHz is desirable. The output should also include an indication of current direction.

OUTPUT: There should be a capability for direct driving of protection equipment.

(see also reference 22 for British Standard requirements)

1.3.2 Disadvantages of conventional current transformers

Unfortunately, these transformers have several defects which degrade their accuracy and reduce their usefulness as part of a measurement and protection system. First, the soft-iron cores suffer from hysteresis and saturation, both of which make for non-linearity in the amplitude response to input current. Second, the magnetisation current taken by the device limits the accuracy of the output for small currents in the primary. This second fault is partly due to the fact that current transformers must be very conservatively designed in order to withstand fault conditions where currents and voltages may rise orders of magnitude above normal operating levels. During such

faults, current transformers may also produce misleading outputs due to their limited frequency response. Some types of fault will produce large but slowly varying currents lasting several seconds which can only produce small changes in the output due to their extremely low frequency. These changes may not be detectable when superimposed on a normal output waveform. At the high frequency end, the current transformer's response is limited by winding capacitance to a few kilohertz. This is totally inadequate for efficient protection against lightning strikes, for instance, where massive currents build up in microseconds.

Current transformers are necessarily large because saturation problems must be minimised. In addition, heavy insulation is needed to isolate the input and output coils and these two requirements combine to make EHT current transformers very large indeed. As a result, present devices are expensive to build and transport, require much costly substation ground space and are physically difficult to handle. These problems all increase sharply as line voltage is raised, and make the use of current transformers in 1 MV distribution systems almost impossible to contemplate.

1.3.3 Basic considerations in applying new solutions to the problem of EHT current measurement

The disadvantages of current transformers described in the preceding section have stimulated research into the use of radical alternatives in EHT current measurement. In order to avoid the necessity for large amounts of insulation, techniques not involving earthed conductors close to EHT lines are attractive. This then either requires that any conductors used in the sensor are continuously at line potential or that a totally passive sensor not employing conductors be used. Sensors of the former type are being developed, but are unreliable and suffer from the additional disadvantage that power must be supplied to the sensor head.

Sensors of the passive type are attractive for their simplicity and attendant long term reliability. To avoid electrical contact with such a sensor, the most obvious possibility is the use of radiation either generated spontaneously by the sensor or supplied from and reflected back to a ground station. The Faraday Effect, involving the action of magnetic fields on electro-magnetic waves in a material, provides an elegant method of current measurement by sensing the magnetic field produced by the current.

1.3.4 The Faraday Effect

When linearly polarised light travels through a material and there is a component of a magnetic field parallel to the path of the light, the polarisation remains linear but rotates at a rate which is linearly dependent on the strength of the field and also dependent on the nature of the material. This is the Faraday Effect. The total rotation of polarisation, θ, of a monochromatic beam of light travelling for a distance, ℓ, in a material subject to a parallel magnetic field, H, is therefore:

$$\theta = V\ell H$$

where V is a constant depending on the material, the wavelength of the light and possibly also other variables such as temperature, pressure, etc. V is the "Verdet constant" of the material under the conditions quoted. Since it is easier to detect large polarisation rotations rather than small ones, for engineering applications we obviously require materials with a high Verdet constant and we also try to maximise the interaction length, ℓ.

1.3.5 Choice of sensor material

One of the first choices in implementing such a device is that of wavelength for the interrogating beam. This choice is influenced by the environmental conditions that the device will normally be subjected to, also by the availability of sensing materials with desirable qualities at the frequency concerned and also of suitable sources and detectors for the wavelength used. There have been attempts to use the Faraday Effect in this connection at microwave, infra-red and optical wavelengths. An important factor in each case was the choice of the sensor material.

Yttrium iron garnet (YIG) has a high Verdet constant at both infra-red and microwave frequencies, and both parts of the spectrum have been used to produce experimental Faraday Effect devices[6,7,8,18]. The main problems with these devices were their liability to non-linearities caused by saturation and domain structure inhomogeneities in the material. Furthermore, the susceptibility of YIG is temperature dependent, and so current monitors using YIG must have temperature compensation built into them[6].

In order to avoid the problems with YIG and similar materials, researchers have looked to materials with the weakest magnetic properties, the diamagnetics, for a solution; these do not suffer from domain structure inhomogeneities or temperature dependence of the Verdet constant. Since the diamagnetics have low susceptibility, the Faraday Effect in these materials is also very small, typically 10^{-5}rad/cm/G. However, optical glass with high transparency can be doped with diamagnetic material without increasing its absorption to unacceptable levels, and so the smaller Faraday rotation per unit length in the material can be countered by providing a much longer interaction length in the glass than is possible with other materials.

1.3.6 Review of Faraday Effect current monitors using bulk glass sensors

By far the largest amount of work on EHT current measurement by the Faraday Effect has been carried out using bulk glass as the sensor material. In general, a block of heavy lead glass is supported inside an insulating ceramic protective shield close to an EHT line. The shield also serves to protect the light path from obstruction by smoke, fog, rain, etc. and the light source and detectors with associated electronic processing circuitry are situated in a metal cabinet at earth potential and beneath the ceramic bushing. A typical design is shown below[9].

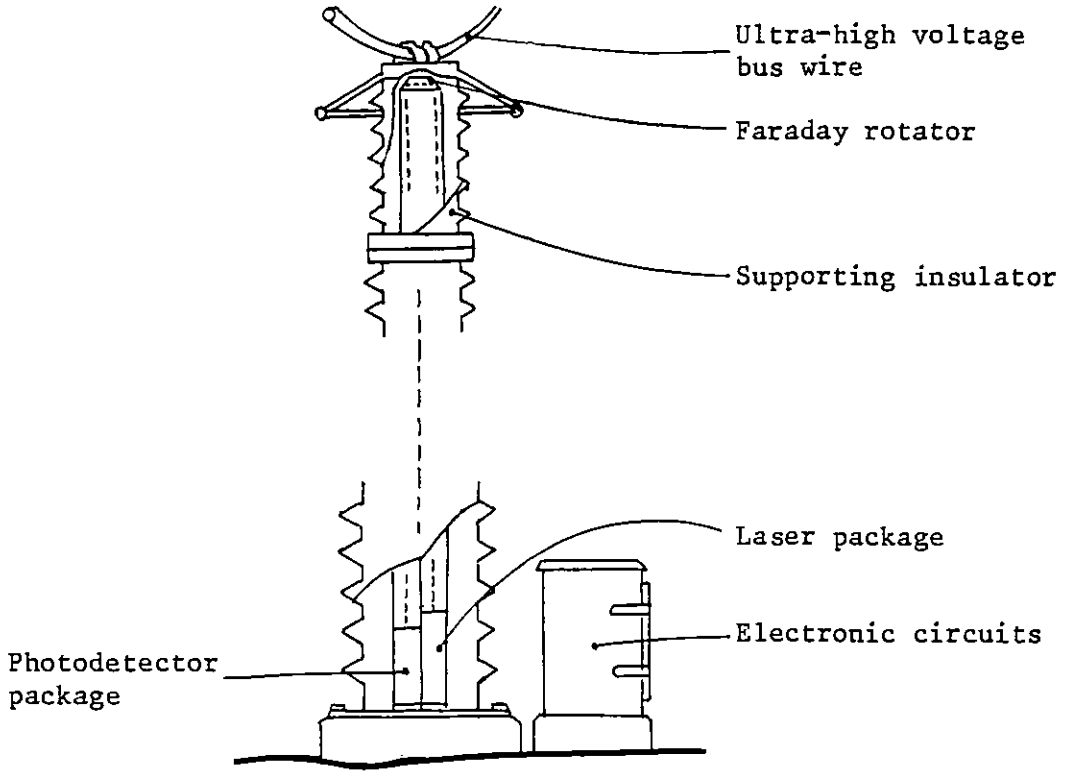

Fig. 1 Proposed laser current transformer

The detailed description of each practical scheme can be seen in references 9 to 20 and will not be discussed here. However, the general conclusions arising from the body of work done are worth attention.

Not unexpectedly, a major problem with Faraday Effect instruments is the difficulty in accommodating the large dynamic range necessary. Since the Faraday rotation in glass is very small even at moderate currents, the photodetector noise limits the smallest detectable current in most systems to ten amps or so. The high limit on range is set by non-linearity in the detector system for rotations greater than a few degrees, normally corresponding to about a thousand amps.

In order to solve the dynamic range problem, several techniques have been tried. Systems employing a second Faraday rotator governed by an auxiliary coil fed with a current to keep the polarisation relatively static have been built. They are complex and unreliable[9,11,16,18], and current work is aimed at simulating a rotator by means of the Pockels Effect in conjunction with suitable retarders. A better

solution seems to be to linearise the output for large rotations by using sophisticated electronic processing techniques and then to produce the large rotations by increasing the interaction length with the interrogating beam bouncing back and forth several times in the sensor before departing towards the ground station[14].

With such a large path length (> 1 m) and number of reflections inside the glass sensor block (20 reflections), the instrument then becomes limited by vibration causing the beam to wander off the detector and also limited by the natural birefringence of the glass itself. Although this second problem can be ameliorated somewhat by a compensation technique[15], the problem of stress induced birefringence due to mounting and temperature gradient effects is not easily soluble. The manner in which birefringence interacts with Faraday Effect will be discussed in more detail later. In order to avoid the vibration problems, sophisticated mechanical design is required and periodic adjustment would also be necessary to compensate for slow beam movements due to creep.

One final disadvantage of bulk glass sensors is that they are also prone to inaccuracy due to stray fields from neighbouring conductors. This problem has been approached by using two similar glass blocks near the wanted conductor so that rotations add for that conductor but subtract for all others[17,20]. The success of this technique depends on careful matching of the optical paths in the two blocks and slow variation of stray field across the apparatus. In substation environments, the last requirement is rarely likely to be closely met.

The foregoing assessment of bulk glass Faraday Effect devices has been only cursory and was designed to pick out the main faults of these instruments. Some are suitable as laboratory or portable instruments for current measurement under unusual conditions, in fact, but none has been adopted for long term use on any large scale power system. For a recent comparison of a wide selection of devices including more detail than given here, see reference 21.

1.3.7 Early attempts to employ optical fibres in current measurement equipment

Faraday Effect devices have also incorporated optical fibres[15,16] purely to protect light from obstructions between the ground station and sensor head, but due to the depolarising effect of the fibres used it was necessary to polarise and analyse the light at the head itself. The consequent loss of signal power and lack of easy maintenance (due to inaccessibility of the optical components) made the devices unacceptable for service. Despite this, a new proposal running along these lines has recently been made[32].

An attempt to use an optical fibre itself as a Faraday sensor in 1972 failed totally because a multimode fibre with extreme depolarising characteristics was used[25]. The same authors also attempted to use graded index fibre as a transmission and sensing medium, but abandoned the attempt due to gross polarisation disturbances caused by fibre bending. The mechanisms behind these effects will be discussed in later chapters.

Another effect which limits the performance of optical fibres as Faraday Effect sensors has been investigated recently. This is the effect of strong birefringence in fibres which partially destroys linear polarisation. Certain types of fibres, specifically graded index and single mode types, will preserve a linear input polarisation under ideal conditions (ie. straight fibre; no external stress) and for specific angles of E-field. However, for all other angles of E-field, these fibres effectively split the polarisation up into two orthogonally polarised modes which then propagate down the fibre with different phase velocities. If the difference in phase velocities is large enough to produce a phase shift per unit length much greater than the polarisation rotation - also measured in angular units per length - then the result is that the Faraday Effect loses its proportionality to field interaction length and is also severely reduced in magnitude[26].

1.3.8 Recent applications of optical fibres as Faraday sensors

As will be explained in the next chapter, the problem of fibre birefringence has been tackled by improved manufacturing techniques and recent publications[27,36] describe laboratory models of Faraday sensors using improved fibres. It has been demonstrated that birefringence had been sufficiently reduced to produce an instrument workable within a generating station environment[27] but it was also clear that the problems of vibration and fibre bending still need attention before a generally applicable field instrument of this type can be made.

1.4 Conclusions from the case study: The need for two types of polarisation-transmitting fibre

The case study produced above demonstrates several interesting conclusions.

First, the principal attraction in using optical fibres for this application is that they provide a convenient method of constraining a beam of light to travel over a very extended interaction path where an optical effect occurs. They do so wthout involving problems of alignment, instability and size of the active part of the device. These advantages are common to the laser gyroscope and Raman oscillator. In this particular instance, there is the further consequent advantage that the fibre can be wrapped closely around a particular conductor in the form of a coil, thus producing the best chance that stray fields will cancel out within the sensor.

Second, transmission through fibres protects the light from attenuation by foreign bodies (smoke, rain, dust, animals, vegetation, etc.) in the optical system. This obviously prevents premature ageing and catastrophic failures of the device which might otherwise occur.

Third, the use of polarisation transmitting fibres allows a hitherto unparallelled flexibility in the situation of source, detector and processing electronics. Since these parts may require periodic attention, freedom to place them in safe areas where work may be done

without interrupting operation of the system may be a significant advantage. (Naturally, it is the safety inherent in using a dielectric path to communicate with an EHT environment which makes this possible at all.)

Fourth, the small size and weight of a fibre device leads us to expect that it might become less costly in terms of labour and materials than its conventional counterpart. (Incidentally, the mechanical simplicity of a fibre device is also strongly marked but in a different way in the fibre gyroscope, where the absence of moving parts leads to better potential reliability as well as potential accuracy.)

Finally, it has become clear that the main drawback to the use of even top quality single mode fibre for the devices mentioned is the sensitivity of polarisation within the fibre to external mechanical influences. In particular, it seems very likely that no reliable optical fibre gyroscope can be produced unless a fibre much less sensitive to external influence is developed.

Ideally, we require a fibre which will faithfully reproduce any input polarisation state at its output. However, it will be shown later that this requirement is incompatible with the further condition that the output polarisation state should be robust to externally imposed influences on polarisation. We must forego trying to satisfy both conditions in the same fibre.

Specifically then, two types of fibre are needed. The first type should be such that all polarisation perturbing tendencies of the fibre are eliminated. This would be for use in situations where we want to transmit polarisation in any form which might itself be varying with time, such as in the sensing section of a Faraday Effect device. Care would obviously have to be taken, when using such a fibre, to eliminate all unwanted sources of polarisation distortion, both internal and external to the fibre.

The second type of fibre needed is one which should be capable of transmitting a single polarisation state only, for example linear polarisation which is not affected by any external influences. If such a fibre is used in conjunction with a properly aligned polarisation splitter at its output, the function of this fibre would be to act as a remote polarising beamsplitter acting at the input end of the fibre.

1.5 Proposal for a workable optical fibre Faraday Effect current monitor

Figure 2 shows a schematic arrangement for a Faraday Effect current monitor employing both types of fibres described above.

Linearly polarised light is fed into a fibre designed to hold this polarisation in spite of bends and vibrations. The polarisation is therefore linear at the point where it is coupled into the sensor head. The sensor itself should be made from isotropic fibre wound into a coil around the busbar in such a way as to minimise bend-induced disturbance of polarisation[30]. In this way, the polarisation remains linear at the end of the sensing section, but is rotated by the Faraday Effect with respect to the original orientation. At the input end of the downward guiding fibre, the polarisation is resolved into two linear, orthogonal components which are then guided independently down to the ground station and are measured separately by photodetectors placed at the outputs of a polarising beamsplitter orientated so as to split the two components apart.

The use of a completely sealed optical path above ground level prevents obstruction of the light beam and obviates any necessity for cleaning of optical surfaces at or near the sensor head. Measurement of two orthogonally polarised components affords a simple method of eliminating noise due to fluctuations in source intensity or system attenuation[31].

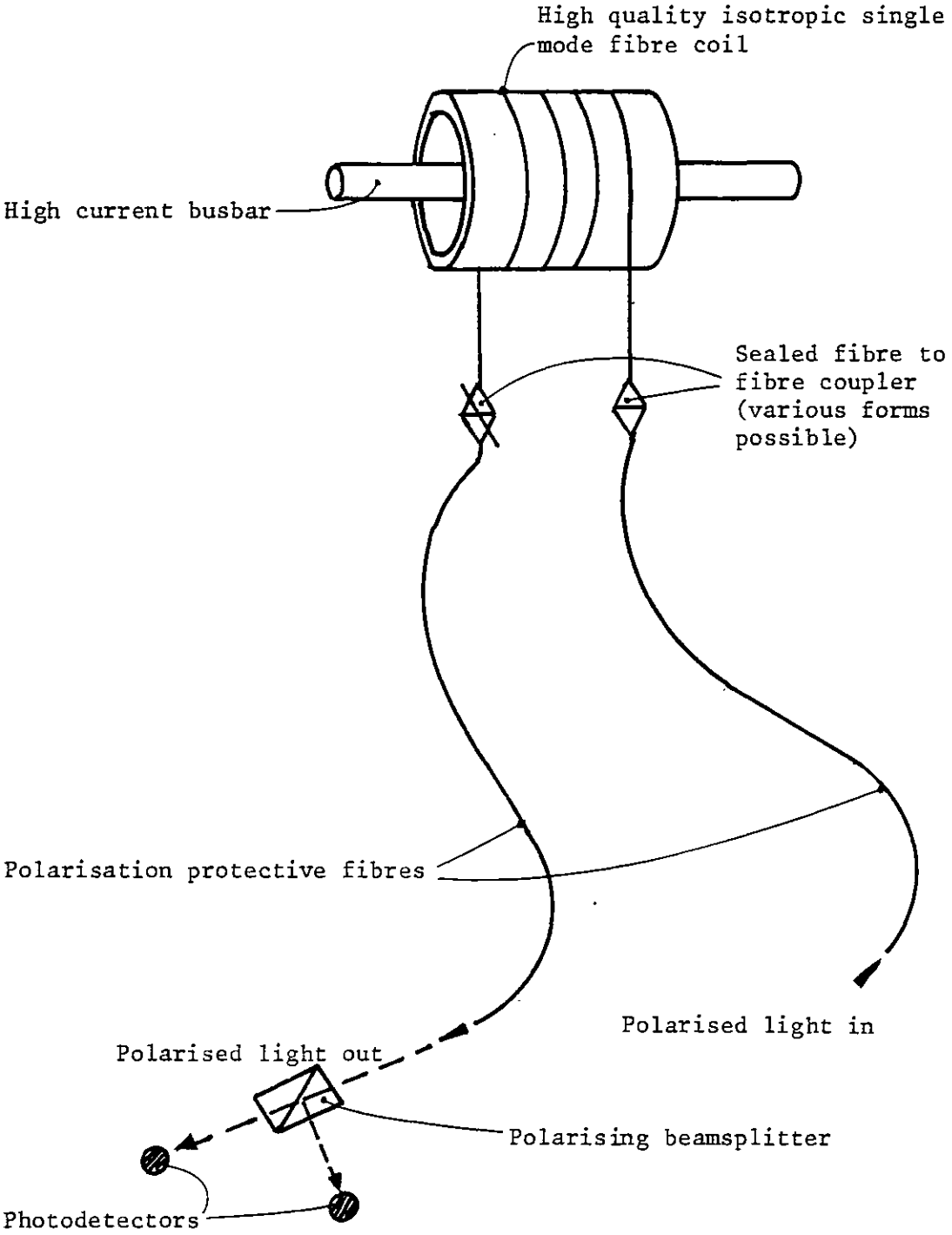

Fig. 2 Schematic arrangement of Faraday Effect current monitor incorporating polarisation holding fibres

References to Chapter I

1. HODGKINSON, T. G., HOOPER, R. C., SMITH, D. W. and WHITE, B. R., "Optical fibre system performance at 140 Mbit/s", IEE Conf. Digest 1978/30.

2. KAO, K. C., COLLIER, M. E. "Fibre-optic systems in future telecommunication networks", Telecommunications, April 1977, pp 25-32.

3. THOMPSON, D. E., ANDERSON, D. B., YAO, S. K., YOUMANS, B. R. "Sagnac fibre ring interferometer gyro with electronic phase sensing using (GaAl)As laser", Appl. Phys. Lett. 33:11 (Dec. 78), pp. 940-941.

4. VALI, V., SHORTHILL, R. W., BERG, M. F. "Fresnel-Fizeau effect in a rotating optical fibre ring interferometer" Appl. Opt. 17:3 (1st February 78), pp. 330-331.

5. BUCARO, J. A., CAROME, E. F. "Electromagnetic field components: their measurement using linear electro-optic and magneto-optic effects" Appl. Opt. 14:11 (Nov 75), pp. 2712-2719.

7. HEBNER, R. E., MALEWSKI, R. A., CASSIDY, E. C. "Optical methods of electrical measurement at high voltage levels" Proc. IEEE 65:11 (Nov 77), pp. 1524-1548.

8. SAITO, S., HAMASAKI, J., FUJII, Y., YOKOYAMA, K., OHNO, Y. "Development of the laser current transformer for extra-high voltage power transmission lines" IEEE J. Qu-E 3:11 (Nov 67), pp 589-597.

9. SAITO, S., FUJII, Y., YOKOYAMA, K., HAMASAKI, J., OHNO, Y. "The laser current transformer for EHV power transmission lines" IEEE J. Qu-E 3:11 (Nov 67), pp. 589-597

10. GOŁODOLINSKIJ, G. W.
Elektrichestvo 1956, No. 8, pp 1 - 4

11. PELENC, Y., BERNARD, G.
"Prototype industriel de transformateur de courant à effet magnéto-optique"
Revue Générale de l'Electricité 76, 7:8, pp. 1055-1064

12. HÉROIN, P., BENOIST, C., DELAMARRE, Y.,
"Mésure d'un courant par un ampèremètre a effet Faraday
Revue Générale de l'Electricité 76, 7:8, pp. 1045-1054

13. TAKESHITA, S., SASANO, T.
Japan Electronic Engineering No. 29 (April 69), pp. 16-20

14. JAECKLIN, A. A.
"Measuring current at Extra-High-Voltage"
Laser Focus May 1970, pp. 35-38

15. JAECKLIN, A. A., LIETZ, M.
"Elimination of disturbing birefringence effects on Faraday rotation"
Appl. Opt. 11:3, pp. 617-621 (March 72)

16. AUMONT, P., PELLETIER, E.
"Réducteurs de courant magnéto-optiques à effet Faraday"
Revue Générale de l'Electricité 80:7/8 (July 71), pp. 617-622

17. CARNEL, A., GREBILLE, B., KAPLAN, C., TEBOUL, J.
"Transformateur de courant magnéto-optique à effet Faraday, astatique"
Revue Générale de l'Electricité 80:11 (Nov 71), pp. 815-826

18. DEFECHEREUX, J.
"Les moyens non conventionnels de mesure de courant sur les lignes à haute tension"
Bulletin Société Royale Belge des Electriciens 88:4, pp. 301-314 (1972)

19. JARACZ, K.
"Przegląd elektroopycznych metod pomiaru napięć i prądów"
Pomiary, Automatika Kontrolla 1974 7, pp. 292-295

20. ROGERS, A. J.
"Optical technique for the measurement of current at high voltage"
Proc. IEE 120:2 (Feb 73), pp. 261-267

21. RZEWUSKI, N., TARNAWECKY, M. Z.
"Unconventional methods for current detection and measurement in EHV and UHV transmission systems"
IEEE Trans Instrumentation and Measurement 1M-24:1, pp. 43-51 (March 75)

22. B.S. 3938:1973 Specification of Current Transformers

23. "Laser measures extra-high-voltage transmission line current"
Laser Focus June 1st, 1965, pp. 11-13

24. STALEWSKI, A., BROWN, C. W.
"Optical link current transformer"
IEE Conf. Digest 125, March 1975

25. HIGHAM, A. D., NEWMAN, J. D.
"Measurement of current using Faraday rotation in glass fibre"
IEE Colloquium Digest: Conference on novel types of transducer, Nov. 27, 1972

26. HARMS, H., PAPP, A., KEMPTER, K.
"Magneto-optical properties of index gradient optical fibres"
Appl. Opt. 15:3 (March 76), pp. 799-801.

27. SMITH, A. M.
"Polarisation and magneto-optic properties of single mode optical fibre"
Appl. Opt. 17:1 (Jan 78) pp. 52-56

28. MIDWINTER, J. E.
"Optical fibre transmission"
Paper presented to Seminex 77 at Imperial College, London.

29. LIN, C., STOLEN, R. H., FRENCH, W. G., MALONE, T. G.
"A c.w. tunable near infra-red Raman oscillator"
Optics Letters 1:3 (Sept 77), pp. 96-97.

30. PAPP, A., HARMS, H.
"Polarisation optics of liquid core optical fibres"
Appl. Opt. 16:5 (May 77), pp. 1315-1319.

31. PAPP, A., HARMS, H.
"Polarisation optics of index gradient optical waveguide fibres"
Appl. Opt. 14:10 (Oct 75), pp. 2406-2411.

32. TEICH, T. H., NEALE, J. A. G.
"Current measurement by means of the Faraday Effect and Pockels Effect"
Proc. Third International Symposium on high voltage engineering, Milan, Aug 28-31, 1979.

33. STOLEN, R. H., IPPEN, E. P.
"Raman gain in glass optical waveguides"
Appl. Phys. Lett. 22:6 (15th March 1973), pp. 276-278.

34. DYOTT, R. B.
"The fibre-optic Doppler anemometer"
MOA 2:1 (Jan 78) pp. 13-18.

35. BIRCH, K.
National Physical Laboratory, Private Communication.

36. PAPP, A., HARMS, H.
"Magneto-optical current transformer: principles, components, measurements"
Appl. Opt. 19:22 (15th Nov 1980), pp. 3729-3745.

CHAPTER II

PROPAGATION OF LIGHT IN IDEAL AND NON-IDEAL FIBRES

In chapter I the various problems involved in preserving the polarisation of light in optical fibres were outlined without explanation. In this chapter we shall consider the polarisation performance of various types of optical fibre by means of a review of the relevant propagation theory. At first, we shall restrict our attention to benign environments where ideal fibres are not strongly affected by their surroundings and then we shall extend our treatment to examine a way in which imperfections may be incorporated into our model to bring it closer to reality.

2.1 The failure of geometrical optics to explain propagation of polarised light in optical fibres

We begin the chapter by considering the applicability of geometrical optics to the function of propagation characteristics in fibres. In general, an optical waveguide is formed by any structure which contains an area of a certain refractive index completely surrounded by other regions of lower index. Large structures of this sort can be understood as guiding light by total internal reflection. The structure may be almost any shape, which normally does not change along the guide. Two common types are the rectangle and the circle. These are depicted in figure 2.1, where the central and surrounding materials are shown as having refractive indices, n_1 and n_2 respectively.

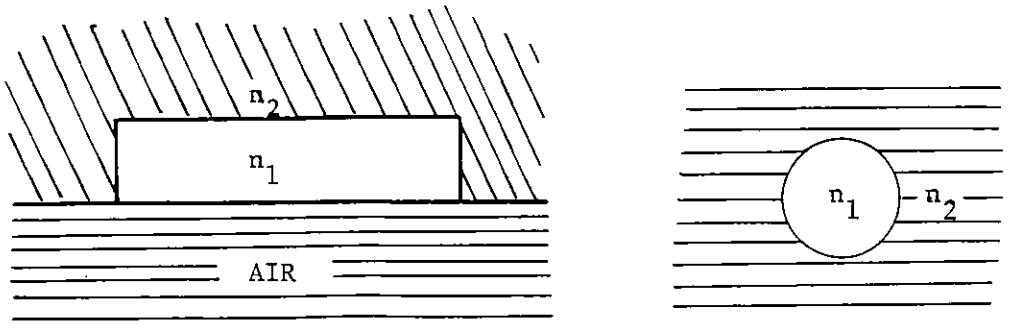

Rectangular guide Circular guide

Fig. 2.1 Two common shapes of optical waveguide

Typically, optical fibres are constructed with circular cross section. The central region is called the core and the surrounding material the cladding.

If it were possible to gain an intuitive understanding of the polarisation behaviour of light in optical fibres using the familiar principles of ray optics and plane wave behaviour, this would obviously be an attractive starting point for our study. Such an approach works acceptably for the slab waveguide[1], yielding equations for the guided modes of the structure. There has been an attempt to extend this approach to circular guides[2], and it is indeed possible to produce equations giving approximately the modes of the structure. However, the published analysis neglects the effect of polarisation, as this would have considerably complicated the treatment. In addition, the physical significance of rays is much reduced in the fibre case because of the curvature of the boundary, which causes any imaginable plane wave of finite size to converge after reflection and also because the ray approach ignores the penetration of optical energy into the cladding. These effects significantly modify the behaviour of the guide.

2.2 Electro-magnetic theory of circular optical fibres

The inadequacies of the simpler methods of analysing optical fibres recommend us to use a more general and fundamental study of their characteristics. This is supplied by electro-magnetic theory. The general treatment of electro-magnetic wave propagation in optical fibres is well documented elsewhere[1,3] and will only be given here in sufficient detail for a general appreciation of the method and the important results of the analysis.

As in figure 2.1, we assume a circular cylindrical region of refractive index, n_1, having radius, a, surrounded by another medium of lower refractive index, n_2, extending to infinity. Both media are assumed to be lossless and non-magnetic, therefore they have purely real values of dielectric constant, ε_1 and ε_2 and magnetic permeability μ_o equal to that of a vacuum. We assume a

system of cylindrical polar co-ordinates, r, ϕ and z with the z axis lined up with the axis of the guide, as this appears to be most convenient for analysis. In this situation, where we have dielectric material inhomogenous in cross-section but independent of z, applying Maxwell's equations leads to the wave equation for both the E_z and H_z components of the waveguide fields:

$$\frac{\delta^2 f}{\delta r^2} + \frac{1}{r}\frac{\delta f}{\delta r} + \frac{1}{r^2}\frac{\delta^2 f}{\delta \phi^2} + \kappa^2 f = 0 \qquad 2.1$$

Here f represents either E_z or H_z. No other field components are needed because in this situation, the transverse field components can be expressed totally in terms of the z components. The wave equation applies to the fields separately inside and outside the core and this leads to the necessity for two sets of solutions, one for the core and one for the cladding, which can be chosen by remembering the physical considerations relevant to the problem.

We search for solutions to the equations by using the method of normal modes, building up a general solution from linear superpositions of harmonic oscillations. Each such possible basic oscillation in the system is called a 'mode' of the system, and can be defined as 'an eigensolution of Maxwell's equations belonging to a particular eigenvalue, and satisfying all the boundary conditions of the problem[4,1]'.

We apply a trial solution of this form:

$$E_z = A\ F(r)\ e^{i\nu\phi}\left[e^{i\ (\omega t - \beta z)}\right] \qquad 2.2$$

Here, A is an amplitude factor and F(r) contains the radial variation of the field. ν is a constant with any integer value and governs the azimuthal variation of the field. The term in square brackets expresses the time and z dependences of the field. The angular frequency ω and the propagation constant β respectively characterise these two dependences. Normally, for convenience in writing, these dependences are not stated explicitly since they occur throughout the subsequent analysis and can be assumed. We follow this practice below. Substitution of the trial solution into the wave equation yields:

$$\frac{d^2f}{dr^2} + \frac{1}{r}\frac{df}{dr} + \left(\kappa^2 - \frac{\nu^2}{r^2}\right)f = 0 \qquad 2.3$$

This is Bessel's equation and its solutions are the well known cylinder functions. We have already noted that our situation has two separate sets of solutions, one for the core and the other for the cladding, and we now choose the appropriate cylinder functions which represent a guided mode. We require that the field should not be infinite anywhere inside the core and that it should be localised in the cladding so as to be near the co re and not travelling in the transverse direction. These considerations lead us to choose the Bessel J_ν function for the field in the core as this remains finite for zero argument. The Hankel $H_\nu^{(1)}$ function with imaginary argument is used to represent guided fields outside the core as this function falls to zero at infinity. We have within the core:

$$E_z = AJ_\nu(\kappa r)\, e^{i\nu\phi}$$

and in the cladding 2.4

$$E_z = BH_\nu^{(1)}(i\gamma r)\cdot e^{i\nu\phi}$$

A and B are amplitude factors and $\kappa^2 = k_1^2 - \beta^2$

$$\text{and } \gamma^2 = \beta^2 - k_2^2$$

(with k_1 and k_2 being the bulk propagation constants for the core and cladding respectively). The expressions for κ and γ follow from the derivation of the wave equation. Exactly similar equations for the H fields yield two more amplitude factors. We now know the shapes of the field distributions, but in order for the field to be completely specified, we need to know β. We can find β by applying the boundary conditions at the core/cladding interface. These specify that magnetic field components tangential to the boundary must each be respectively continuous across this boundary. Consequently, for any guided mode this imposes a relation between the two sets of solutions. Since these are two tangential E-field components and two H-field components, we now have four equations relating these solutions. For non-trivial solutions, the determinant of this system of four homogeneous equations must be zero. This yields the eigenvalue equation:

$$\left(\frac{\varepsilon_1}{\varepsilon_2}\frac{a\gamma^2}{\kappa}\frac{J_\nu'(\kappa a)}{J_\nu(\kappa a)} + i\gamma a\frac{H_\nu^{(1)'}(i\gamma a)}{H_\nu^{(1)}(i\gamma a)}\right)$$

$$\times\left(\frac{a\gamma^2}{\kappa}\frac{J_\nu'(\kappa a)}{J_\nu(\kappa a)} + i\gamma a\frac{H_\nu^{(1)'}(i\gamma a)}{H_\nu^{(1)}(i\gamma a)}\right)$$

$$= \left[\nu\left(\frac{\varepsilon_1}{\varepsilon_2} - 1\right)\frac{\beta k_2}{\kappa^2}\right]^2 \qquad 2.5$$

This is a transcendental equation in β which can only be solved by numerical methods. We can considerably simplify the solution by remembering that usually for optical fibres $\varepsilon_1 \simeq \varepsilon_2$. This allows us to treat $\varepsilon_1/\varepsilon_2$ as being unity but otherwise retaining ε_1 and ε_2 as distinguishable values.

With this approximation, we find two simpler eigenvalue equations

$$\frac{J_{\nu\pm1}(\kappa a)}{\kappa a J_\nu(\kappa a)} = \frac{H_{\nu\pm1}^{(1)}(i\gamma a)}{i\gamma a\, H_\nu^{(1)}(i\gamma a)} \qquad 2.6$$

These equations describe two sets of modes which are labelled $HE_{\nu\mu}$ (minus sign) and $EH_{\nu\mu}$ (plus sign). The index ν indicates the number of cycles of azimuthal variation in the fields. This is already explicit in the trial solution 2.5. The second suffix μ counts the number of radial nodes in the pattern, ignoring any at the fibre axis. Both types of modes generally have six field components, except for those where $\nu = 0$. However, there is a physical difference between the types; the peaks in the energy distribution for the EH modes lie further from the centre of the guide than for HE modes of the same ν and μ. In the special case where $\nu = 0$, we can classify the modes by their field configurations because we find that this case embraces two types of modes, one with no z-component for the E-field and the other with a z-directed H-field. These modes are classified as TE and TM respectively to denote that the electric and magnetic fields are respectively purely transverse.

We can further simplify the equations by making use of the recurrence relations for Bessel Functions and show that both equations reduce to exactly the same form when ν is replaced with $(\nu' + 1)$ in the HE case and with $(\nu' - 1)$ in the EH case. Thus, to the degree of

approximation inherent in assuming $\varepsilon_1 \simeq \varepsilon_2$, we find that $HE_{\nu\mu}$ modes propagate with the same phase velocity as $EH_{(\nu-1),\mu}$ modes. The approximation we have made is equivalent to ignoring the z components of the modal fields. In practice these are smaller than the transverse components by a factor of order $(\varepsilon_1 - \varepsilon_2)/\varepsilon$, typically about 0.01.

Before we can consider the implications of this analysis for polarisation behaviour, we note that for each mode there is a frequency below which that mode will not propagate. The mode is said to be 'cut off' in this eventuality. The cut-off frequency of each mode occurs when $\beta = n_2 k_o$, that is when $\gamma = 0$. In order to study more easily the cut-off conditions, the eigenvalue equation 2.5 is re-expressed:

$$\left[\frac{\varepsilon_1}{\varepsilon_2}\frac{J_{\nu-1}(\kappa a)}{\kappa a J_\nu(a)} - \frac{H^{(1)}_{\nu-1}(i\gamma a)}{i\gamma a H^{(1)}_\nu(i\gamma a)}\right]\left[\frac{J_{\nu+1}(\kappa a)}{\kappa a J_\nu(\kappa a)} - \frac{H^{(1)}_{\nu+1}(i\gamma a)}{i\gamma a H^{(1)}_\nu(i\gamma a)}\right]$$

$$+\left[\frac{\varepsilon_1}{\varepsilon_2}\frac{J_{\nu+1}(\kappa a)}{\kappa a J_\nu(\kappa a)} - \frac{H^{(1)}_{\nu+1}(i\gamma a)}{i\gamma a H^{(1)}_\nu(i\gamma a)}\right]\left[\frac{J_{\nu-1}(\kappa a)}{\kappa a J_\nu(\kappa a)} - \frac{H^{(1)}_{\nu-1}(i\gamma a)}{i\gamma a H^{(1)}_\nu(i\gamma a)}\right]$$

$$= 0 \qquad 2.7$$

We then make use of the approximate forms for the Bessel and Hankel functions with small arguments to simplify this equation and thereby give us the following simple expressions:

For $\nu = 0$	$J_o(\kappa a) = 0$	for TE, TM modes
$\nu = 1$	$(\kappa a) = 0$	for HE_{11} mode
$\nu > 1$	$J_\nu(\kappa a) = 0$	for EH modes and $HE_{1\mu}$ modes
$\nu > 2$		for $HE_{\nu\mu}$ modes

2.8

We see that the HE_{11} mode has no cut-off and that the first modes with a cut-off are those at the first zero of $J_o(\kappa a)$. These are the TE_{01} and TM_{01} modes.

We see from the above that it is the value of κa which governs the cut-off wavelength for all modes of the fibre. Unfortunately, this contains the value of β and would involve much calculation if used in this form when designing fibres to have only a single mode. We noted earlier that $\gamma = 0$ at cut-off and we can make use of this to arrive at a simpler way of calculating cut-off conditions for fibres. If we add $(\gamma a)^2$ to $(\kappa a)^2$ we can eliminate the actual β from our calculations and work simply in terms of the core diameter and index difference of the fibre. Thus:

$$(\kappa a)^2 + (\gamma a)^2 = (k_1^2 - k_2^2)\, a^2$$

$$= (n_1^2 - n_2^2) k_o^2 a^2 \qquad 2.9$$

The square root of this sum is an easily calculated quantity which is conventionally given the symbol V and is called the 'normalised frequency' of the fibre. Thus:

$$V = \frac{2\pi a}{\lambda_o} \sqrt{n_1^2 - n_2^2} \qquad 2.10$$

2.3 Representation of propagation behaviour; the ω-β diagram

The algebraic treatment of propagation in optical fibres given above can be interpreted diagrammatically with the help of the ω/β diagram. This is a very useful aid for visualising many effects in optical fibres. The ω/β diagram is a plot of the propagation constants for the modes of a waveguide against the frequency of the launched wave. A typical diagram of this sort is shown in figure 2.2.

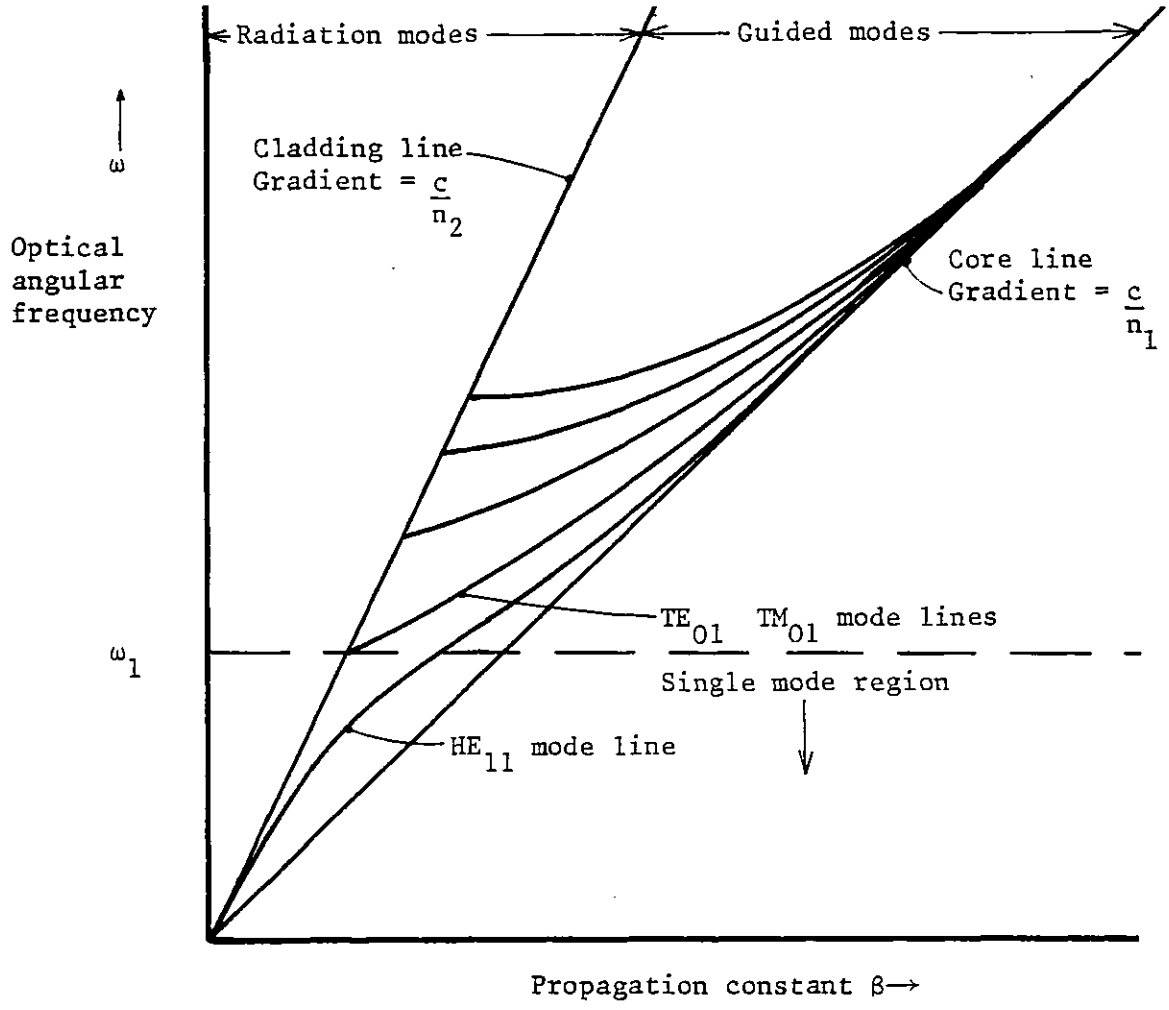

Fig. 2.2 The ω/β diagram for representation of optical fibre propagation characteristics

Referring to equations 2.2, we note that when $\beta z = 2\pi$, the distance, z, is equivalent to the wavelength of the radiation in the guide, λ_g, since the exponential factor duplicates itself at intervals of $2\pi i$. Thus we see that:

$$\beta = \frac{2\pi}{\lambda_g} \qquad 2.11$$

And so ω divided by β is simply the product of the optical frequency, f, and λ_g, which gives the phase velocity of light in the guide. For non-dispersive isotropic materials, the phase velocity of light is independent of frequency and so these materials can be represented on the ω-β diagram by a straight line through the

origin. Figure 2.2 shows the core and cladding materials of a fibre in this way, the phase velocity of light in each medium being given by the free space velocity of light divided by the appropriate refractive index.

The phase velocities of guided modes of the fibre must always lie between the limits imposed by the core and cladding lines. At cut-off, when a transverse modal field extends very far into the cladding, the modal propagation constant is equal to that of the cladding for the frequency concerned. As the frequency is raised, the mode becomes better bound and the field is confined more nearly to the core and so the modal propagation constant approaches that of the core material. Many standard texts[5] show that the velocity of propagation for energy in a weakly dispersive medium is given by the slope of the ω-β curve at the operating frequency. This velocity is the "group velocity" of the wave. The diagram is therefore well suited to the visualisation of fibre dispersion characteristics.

For any particular operating frequency, the mode structure of the fibre is displayed along the appropriate horizontal line in the diagram. The figure clearly displays that the fibre has only one guided, propagating mode for frequencies up to ω_1. When operated below this frequency, the fibre is known as a 'single mode' fibre. Radiation modes of the fibre can be regarded as existing throughout the space to the left of the cladding line in the diagram.

Problems involving mode coupling, anisotropy and harmonic generation can also be visualised with the ω-β diagram. In particular, the problems of mode coupling and anisotropy will be examined in the following sections.

2.4 Polarised light in multimode fibres

In section 2.2 we noted that to a very good approximation the propagation constant of $HE_{\nu\mu}$ modes and $EH_{\nu-2,\mu}$ modes are closely equal. We may make use of this fact to produce new approximate and simplified modes of optical fibres. The field configurations of these modes govern our expectations of the polarisation behaviour of these fibres.

Equations 2.4 gave the z-component of guided modes in the core and cladding of a fibre. We can re-express these equations in terms of the more familiar circular functions by adding a new trial solution of the wave equation in cylindrical co-ordinates (2.1), replacing ν with $-\nu$ and forming linear combinations with the original solutions by addition and subtraction of the equations. Thus we find

$$E_z = F_\nu \begin{Bmatrix} \cos \nu\phi \\ i \sin \nu\phi \end{Bmatrix}$$

$$H_z = \pm G_\nu \begin{Bmatrix} -\sin \nu\phi \\ i \cos \nu\phi \end{Bmatrix} \qquad 2.12$$

Here, the F and G are new amplitude factors and the two possible signs and sets of circular functions must be used independently. The differing signs denote HE and EH modes as before, while the different groups of circular functions describe orthogonal polarisations. The transverse field components can be derived from the z-components by applying Maxwell's equations to give:

$$E_x = \pm F_{\nu\pm1} \begin{Bmatrix} i \cos (\nu\pm1)\phi \\ -\sin (\nu\pm1)\phi \end{Bmatrix}$$

$$E_y = F_{\nu\pm1} \begin{Bmatrix} i \sin (\nu\pm1)\phi \\ \cos (\nu\pm1)\phi \end{Bmatrix}$$

$$H_x = -G_{\nu\pm1} \begin{Bmatrix} i \sin (\nu\pm1)\phi \\ \cos (\nu\pm1)\phi \end{Bmatrix} \qquad 2.13$$

$$H_y = \pm G_{\nu\pm1} \begin{Bmatrix} i \cos (\nu\pm1)\phi \\ -\sin (\nu\pm1)\phi \end{Bmatrix}$$

If we now add or subtract the field components for $HE_{\nu'+1,\mu}$ modes to those for $EH_{\nu'-1,\mu}$ modes, we achieve cancellation of the E_x and H_y components, leaving only the four field components E_z and H_z, E_y and H_x to describe the approximate, simplified modes. In particular, the transverse fields become:

$$E_y = 2F_{\nu'} \cos \nu'\phi$$

$$H_x = -2G_{\nu'} \cos \nu'\phi \qquad 2.14$$

This is true for addition of the HE and EH modes. Subtraction of the components leads to fields which are orthogonally polarised to these. We see then, that this description of the modal fields, which was perfected by Gloge[6], leads to the conclusion that the resulting field of all the modes in a multimode fibre will be linearly polarised. In the limit of weak guidance, when $n_1 = n_2$, this would be exactly true, and Gloge coined the name, 'linearly polarised' (LP) modes for the simplified modes of optical fibres.

In reality, however, since the core and cladding indices are never equal, the propagation constants of the true fibre modes are likewise unequal and the linear superpositions forming the LP modes decompose progressively along the fibre, leading to elliptical polarisation at moderate distances from the fibre end. Further phase shift of the true modes leads to periodic variation in the polarisation along the fibre, from linear to elliptical to linear, etc. So we see that even under ideal conditions multimode fibres cannot be expected to preserve the polarisation of the light they carry.

In non-ideal conditions, the picture is further complicated by the effects of mode coupling within the fibre, imperfect launching conditions and selective modal attenuation. In addition, finite spectral width of the light source will produce depolarisation by a loss of coherence due to inter-mode delays[7] and, finally, any attempt to use these fibres in interferometric applications would also be severely hampered by the variations in phase and polarisation across the far-field patterns. This is a manifestation of the modal noise effect[8] which will always occur in situations where only a part of an end pattern is used for measurements.

2.5 Polarised light in single mode fibres

Returning to the general description of the true modal fields (2.13) we now examine the behaviour of an ideal fibre operating in the 'single mode' region. We have already seen that the HE_{11} mode for which $\nu = 1$, has no cut-off. When only this mode propagates, the transverse field in a fibre is described completely by the field expressions appropriate to this mode. When we insert $\nu = 1$ into these expressions, taking the upper and lower circular functions separately as we must in all cases to account for orthogonal

polarisations, we see that one E and one H component vanishes for each polarisation. Thus the field of the HE_{11} mode is linearly polarised and can exist in either of two orthogonal states. Taking one polarisation only, we find that the complete set of fields for one polarisation of the HE_{11} mode are given by:

Inside the core ($r < a$)	Outside the core ($r > a$)
$\underset{\sim}{E}_z = \frac{iA\kappa}{\beta} J_1(\kappa r) \sin\phi$	$= -\frac{A\gamma}{\beta} \frac{J_o(\kappa a)}{H_o^{(1)}(i\gamma a)} H_1^{(1)}(i\gamma r) \sin\phi$
$\underset{\sim}{E}_y = A J_o(\kappa r)$	$= A \frac{J_o(\kappa a)}{H_o^{(1)}(i\gamma a)} H_o^{(1)}(i\gamma r)$
$\underset{\sim}{E}_x = 0$	$= 0$
$\underset{\sim}{H}_z = \left(\frac{\varepsilon_o}{\mu_o}\right)^{\frac{1}{2}} \frac{iA\kappa}{k_o} J_1(\kappa r) \cos\phi$	$= \left(\frac{\varepsilon_o}{\mu_o}\right)^{\frac{1}{2}} \frac{A\gamma}{k_o} \frac{J_o(\kappa a)}{H_o^{(1)}(i\gamma a)} \times H_1^{(1)}(i\gamma r) \cos\phi$
$\underset{\sim}{H}_y = 0$	$= 0$
$\underset{\sim}{H}_x = -n A \frac{\beta}{\lvert\beta\rvert} \left(\frac{\varepsilon_o}{\mu_o}\right)^{\frac{1}{2}} J_o(\kappa r)$	$= -nA \frac{\beta}{\lvert\beta\rvert} \left(\frac{\varepsilon_o}{\mu_o}\right)^{\frac{1}{2}} \frac{J_o(\kappa a)}{H_o^{(1)}(i\gamma a)} \times H_o^{(1)}(i\gamma r)$

(A is an amplitude factor) 2.15

The orthogonally polarised mode is obtained by replacing $\sin\phi$ with $-\cos\phi$ and $\cos\phi$ with $\sin\phi$ in the expressions where they appear. This orthogonal polarisation is degenerate with the first when the fibre is perfectly cylindrically symmetrical. In reality, however, it is more helpful to regard these two polarisations as being two separate, fundamental modes. This is because real 'single' mode

fibres turn out to be significantly anistropic (for reasons which will be examined in chapter three) exhibiting birefringence and optical activity. In fact, the term 'single mode' fibre should be regarded as a misnomer for most fibres of this type.

2.6 The coupled mode theory for analysing real fibre behaviour

To see how polarisation changes occur we must extend our theory to approach reality more closely by taking into account the imperfections which all real fibres possess.

We have seen that the solutions for the circular step index optical fibre are available in fairly simple forms. Unfortunately, real fibres tend to have non-circular cores with something other than a step index change between the core and cladding. There is also very often an index dip in the centre of the core. Solutions for these real fibres are much more difficult to produce in simple form. For this reason, we try to express the solutions for the real guide in terms of those appropriate to a similar appropriately chosen hypothetical guide. Because the real guide differs from the hypothetical one the modes we use are obviously not individually solutions of Maxwell's equations for the system and the effect of the difference between the real and hypothetical guides will be to cause coupling between the modes we choose to represent the actual field. Coupled mode theory can be used to analyse this process. For many practical cases the real waveguide may differ only very slightly from the hypothetical guide and any changes in shape will be very slow over a wavelength. This allows us to consider the coupling as being weak. In addition, many practical cases also involve only two modes, allowing perturbation solutions to be applied.

The coupled mode formalism is well documented elsewhere and only a brief outline of the mathematical argument will be given here as a preparation for later work. We begin by noting that the longitudinal (z) components of the total field in a fibre can be derived from the transverse components using Maxwell's equations. We can separate the total field, $\underset{\sim}{E}$, in a fibre into its transverse part $\underset{\sim}{E}_t$ and its longitudinal part, $\underset{\sim}{E}_z$. Thus:

$$\underset{\sim}{E} = \underset{\sim}{E}_t + \underset{\sim}{E}_z \qquad 2.16$$

Because $\underset{\sim}{E}_z$ is totally dependent on $\underset{\sim}{E}_t$, we can simplify the problem by eliminating all $\underset{\sim}{E}_z$ components from the field equations and replacing them in terms of $\underset{\sim}{E}_t$ and solving for the transverse fields only. We can now represent $\underset{\sim}{E}_t$ in terms of a superposition of the guided fields $\underset{\sim\nu t}{\mathcal{E}}$ and radiation fields, $\underset{\sim\rho t}{\mathcal{E}}$ of the normal modes of our hypothetical guide. (Here ν and ρ represent mode labels) These fields are taken to be functions of the transverse co-ordinates only, the z-dependences being separately expressed, as described below.

$$E_t = \sum_{\nu=1}^{N} a_\nu \underset{\sim\nu t}{\mathcal{E}} + \int_0^\infty a_\rho \underset{\sim\rho t}{\mathcal{E}} \, d\rho \qquad 2.17$$

A similar equation applies for the magnetic fields. The a are amplitude coefficients which express the z dependence of the mode fields:

$$a_\nu = c_\nu^{(\pm)} \exp(\mp j \beta_\nu z) \qquad 2.18$$

Here C_ν is the constant mode amplitude coefficient appropriate to the hypothetical guide. The ± signs serve to differentiate forward and backward travelling modes. Substituting these field expansions into Maxwell's equations gives a system of coupled differential equations relating the amplitude coefficients. By applying the orthogonality condition for the modes of the hypothetical guide and simplifying, we arrive at the following system of coupled equations covering all the modes of the system.

$$\frac{dc_\mu^{(+)}}{dz} = \sum_\nu \left\{ K_{\mu\nu}^{(+,+)} c_\nu^{(+)} \exp\left[i (\beta_\mu - \beta_\nu) z \right] + K_{\mu\nu}^{(+,-)} c_\nu^{(-)} \exp\left[i (\beta_\mu + \beta_\nu) z \right] \right\}$$

$$\frac{dc_\mu^{(-)}}{dz} = \sum_\nu \left\{ K_{\mu\nu}^{(-,+)} c_\nu^{(+)} \exp\left[-i (\beta_\mu + \beta_\nu) z \right] + K_{\mu\nu}^{(-,-)} c_\nu^{(-)} \exp -\left[i (\beta_\mu + \beta_\nu) z \right] \right\} \qquad 2.19$$

Here the $K_{\mu\nu}$ represent the coupling coefficients between modes μ and ν travelling both forward and backward, as designated by the + and - signs. These coupling coefficients are defined by the relation:

$$K_{\mu\nu}^{(p,q)} = \frac{\omega \varepsilon_o}{4i P} \int_{-\infty}^{\infty} \int_{-\infty}^{\infty} (n^2 - n_o^2) \left[\frac{|\beta_\mu|}{\beta_\mu^{(p)}} \underset{\sim}{\mathcal{E}}_{\mu t}^{(p)*} \cdot \underset{\sim}{\mathcal{E}}_{\nu t}^{(q)} + \left(\frac{n_o^2}{n^2}\right)\left(\frac{|\beta_\mu|}{\beta_\mu^{(p)*}}\right) \underset{\sim}{\mathcal{E}}_{\mu z}^{(p)*} \cdot \underset{\sim}{\mathcal{E}}_{\nu z} \right] dxdy \qquad 2.20$$

P is a normalisation factor derived from the orthogonality condition[9]. The p and q represent + and - signs as appropriate to describe modes travelling in their particular directions. This expression tells us that modes couple only if there is an overall non-zero sum of the scalar product of the fields for the two modes concerned in that region of an infinite cross section where the actual guide index, n, differs from that of the hypothetical guide, n_o.

2.7 Perturbation solutions of the coupled mode theory for the single mode case

The normal modes of the real fibre must have a simply periodic z dependence, such that the total transverse fields can be represented as:

$$\underset{\sim}{E}_t = c_t \exp(-i \beta_t z) \underset{\sim}{\mathcal{E}}_{\nu t} \qquad 2.21$$

If we consider this total field as formed from a sum of only the guided modes of the fibre and compare this expression with 2.17 and 2.18, we can absorb the remaining slow z-dependence in the real fibre of the ideal mode amplitude factors C_ν as follows:

$$C_\nu^+ = C_{\nu o}^+ \exp[-i(\beta_t - \beta_\nu) z]$$

$$C_\nu^- = C_{\nu o}^- \exp[-i(\beta_t + \beta_\nu) z] \qquad 2.22$$

Now $C_{\nu o}^{\pm}$ are independent of z.

We have already remarked that for weak coupling, where there are only slight differences between the real and hypothetical guide, and where these differences change only slowly along the guide, it is often adequate to consider coupling between only two modes, and so perturbation solutions can be applied. Substituting the expressions 2.22 into the coupled mode equations 2.19 leads in this case to four simultaneous equations for the amplitudes of the hypothetical modes:

$$
\begin{aligned}
&K_{\mu\mu}^{(+,+)} + i\,(\beta_t-\beta_\mu)\;\; c_{\mu o}^{+} + K_{\mu\nu}^{(+,+)}\, c_{\nu o} + K_{\mu\mu}^{(+,-)}\, c_{\mu o}^{-} \\
&\qquad\qquad + K_{\mu\nu}^{(+,-)}\, c_{\nu o}^{-} \;\; = \;\; 0 \\
&K_{\mu\mu}^{(-,+)}\, c_{\mu o}^{+} + K_{\mu\nu}^{(-,+)}\, c_{\nu o}^{+} + K_{\mu\mu}^{(-,-)} + i(\beta_t+\beta_\mu)\; c_{\mu o}^{-} \\
&\qquad\qquad + K_{\mu\nu}^{(-,-)}\, c_{\nu o}^{-} \;\; = \;\; 0 \\
&K_{\mu\nu}^{(+,+)}\, c_{\mu o}^{+} + K_{\nu\nu}^{(+,+)} + i(\beta_t-\beta_\nu)\; c_{\nu o}^{+} + K_{\nu\mu}^{(+,-)}\, c_{\mu o}^{-} \\
&\qquad\qquad + K_{\nu\nu}^{(+,-)}\, c_{\nu o}^{-} \;\; . \;\; = \;\; 0 \\
&K_{\nu\mu}^{(-,+)}\, c_{\mu o}^{+} + K_{\nu\nu}^{(-,+)}\, c_{\nu o}^{+} + K_{\nu\mu}^{(-,-)}\, c_{\mu o}^{-} \;\; + \\
&\qquad\qquad K_{\nu\nu}^{(-,-)} + i(\beta_t+\beta_\nu)\; c_{\nu o} = 0
\end{aligned}
\qquad 2.23
$$

For non-trivial solutions, the determinant of the coefficients of these equations must be zero. This leads to a fourth order equation in β_t. This can be simplified if we can reason that $K_{\mu\mu}$ and $K_{\nu\nu}$, which represent modes coupling to themselves, will be large for small perturbations, while $K_{\mu\nu} = K_{\nu\mu}$ will be small. We then have:

$$
\begin{aligned}
\beta_{t\mu} &= \pm\,(\beta_\mu^2 + 2\,i\,\beta_\mu\, K_{\mu\mu})^{\frac{1}{2}} \\
\beta_{t\nu} &= \pm\,(\beta_\nu^2 + 2\,i\,\beta_\nu\, K_{\nu\nu})^{\frac{1}{2}}
\end{aligned}
\qquad 2.24
$$

In the case of the single mode fibre, there is only one guided mode, so, $K_{\mu\nu} = K_{\nu\mu} = K_{\nu\nu} = 0$ and we are left with only one equation for β_t, with $\mu = 1$. Thus:

$$\beta_{t1} = \pm (\beta_1^2 + 2 i \beta_1 K_{11})^{\frac{1}{2}} \qquad 2.25$$

We shall use this expression later to consider the effect of deformations on the propagation of polarised light in single mode fibres.

References to Chapter II

1. MARCUSE, D.
"Theory of dielectric optical waveguides"
London; Academic Press; 1974, p.3 et seq.

2. LOVE, J. D., SNYDER, A. W.
"Optical fibre eigenvalue equation: plane wave derivation"
Appl. Opt. 15:9 (Sept 76), pp. 2121-5

3. MARCUSE, D
"Light transmission optics"
London; Van Nostrand Reinhold; 1972, pp. 289-305

4. Ibid, p. 11

5. For instance, see BROWN, J., GLAZIER, E. V. D.
"Telecommunications"
London; Chapman and Hall; 1974 (2nd ed), pp. 80-83

6. GLOGE, D.
"Weakly guiding fibres"
Appl. Opt. 10:10 (Oct 71), pp. 2252-2258

7. RASHLEIGH, S. C., ULRICH, R.
"Polarisation mode dispersion in single mode fibres"
Optics Letters 3:2, (August 78), pp. 60-2

8. EPWORTH, R. E.
"The phenomenon of modal noise in digital and analogue optical fibre systems"
Istituto Internazionale delle Communicazioni, Genova, Sept. 78.

9. MARCUSE, D.
"Theory of dielectric optical waveguides"
London; Academic Press; 1974, p. 95 et seq.

CHAPTER III

POLARISATION PERFORMANCE OF EXISTING OPTICAL FIBRES

This chapter describes experiments to test the polarisation performance of double crucible drawn single mode fibre and compares the results with work done elsewhere on other types of fibre. At the time this work was done there was only one published study[1] on the polarisation characteristics of 'single mode' fibre. Since then, several other similar investigations have been published, allowing the work reported in this chapter to be put in a broad perspective.

The chapter continues by examining the mechanisms of polarisation change in fibres in the light of the theory developed in chapter two. Once again, since this work was done, further publications have appeared elsewhere and these will be briefly discussed for completeness.

3.1 Measurement of the polarisation performance of double crucible drawn single mode fibre

3.1.1 Reason for measurements

The only study of polarisation in single mode fibres which appeared in the literature before the work described in this chapter was done concerned single mode fibres made by the controlled vapour deposition (CVD) process[1]. Since the fibre available at Imperial College was of significantly different design and was made by the double crucible process, we were interested to know how this type of fibre compared with CVD fibre. Firstly, it seemed that the core could be expected to be more precisely circular in the double crucible fibre because this fibre is made by a one stage process, being drawn directly from the circular orifice of a crucible containing molten glass. The CVD fibre, on the other hand, must withstand many stages of production without being significantly distorted.

The double crucible drawn fibre used in these experiments had a 3 μm diameter core and 15 μm diameter cladding. The base glass was borosilicate and the core-to-cladding refractive index difference was 8×10^{-3}.

3.1.2 Basis of measurements

The two effects which transform polarisation in a non-absorbing, non-scattering body are linear and circular birefringence. (Circular birefringence is also known as optical activity.) Linear birefringence is the name given to that effect whereby a material will impart different phase velocities to two orthogonally, linearly polarised waves propagating in the same direction in the material. In general, there will be a particular orientation of these mutually perpendicular polarisations for which the difference in phase velocities is a maximum. When light linearly polarised along either of these axes is directed into the material in the given direction, it will remain linearly polarised and undergo no transformation. Under these conditions, such axes are called privileged axes.

An optical component exhibiting linear birefringence is called a linear retarder. The retarder can be completely characterised by the degree of retardation - i.e. phase shift - it produces between perpendicularly polarised waves and by specification of the orientation of the privileged axes. In order to find these two pieces of information for a particular piece of optical fibre or any other type of retarder, the following measurements must be made.

Linearly polarised light entering a linear retarder will become elliptically polarised during its passage through the retarder and on leaving will have a general ellipse as its polarisation form. A polarisation analyser may be rotated in front of this emergent beam so as to secure a minimum transmitted intensity. The E-field transmission axis of the analyser will now correspond to the minor axis of the ellipse, and the wave polarised in this direction will be $\pi/2$ radians out of phase with the wave polarised on the major axis. The ellipse can therefore be reconverted into plane polarised light by

interposing a quarter-wave plate between the fibre output and the analyser. The orientation of the quarter-wave plate may be set correctly simply by reference to the orientation of the transmission axis of the analysing polariser. Finally, the polariser may be rotated once more to find the correct orientation for complete extinction of the light.

Figure 3.1 shows that the ratio of the field amplitudes on the ellipse axes is given directly by the tangent of the angle, θ, between the minor axis position for the initial minimum transmission and the position for a final extinction angle of the polariser. The ratio of the corresponding intensities is then given by the square of the amplitude ratio.

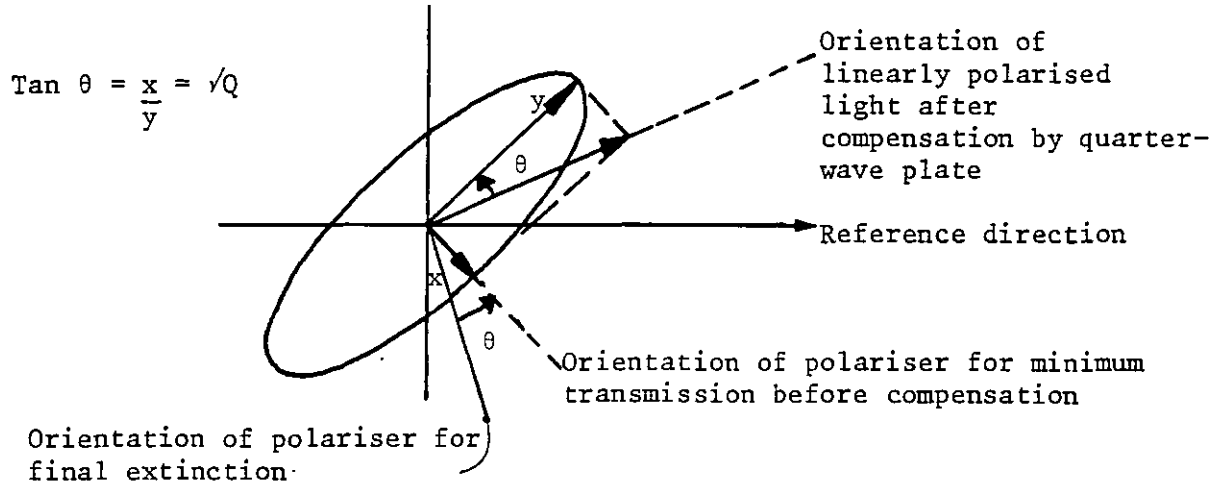

Fig. 3.1 Output polarisation ellipse and linear polarisation attainable by means of a quarter wave plate

The 'degree of polarisation', P, of a beam of light is commonly defined by the following equation:

$$P = \frac{I_{max} - I_{min}}{I_{max} + I_{min}} \qquad 3.1$$

where I_{max} and I_{min} are the intensities corresponding to those of the major and minor axes respectively of the polarisation ellipse. Papp and Harms[12] show that for light which is linearly polarised and launched into a fibre at 45° to the privileged axes, the degree of polarisation of light emerging from the fibre is given by the cosine of the phase shift, δ, between the modes travelling on the privileged axes:

$$P = \cos \delta \qquad 3.2$$

Therefore, to find the phase shift produced by the test fibre in the experiments described here, it was only necessary to substitute the intensity ratio, Q, observed in the output ellipse under the correct launching conditions into equations 3.1 and 3.2:

$$\delta = \cos^{-1} \frac{(1 - Q)}{(1 + Q)} \qquad 3.3$$

The intensity ratio itself was found for a 180° range (initially) of input linear polarisations in order that graphical display of the results should identify the privileged axes of the fibre and provide a more accurate estimate of the intensity ratio at midway-between-privileged-axis launching. This was necessary because of the variability in the results obtainable using the available equipment.

3.1.3 Measurement made and reduction of data

A single piece of monomode fibre was laid on a flat level surface and linearly polarised light was launched into it with the polarisation direction ranging in 10° steps from 0° to 180° with respect to the vertical axis. For each input polarisation the output ellipse was measured and the intensity ratio of the fields on the ellipse axes was plotted against the input polarisation angle. A sample of the graphs plotted is shown in figure 3.2.

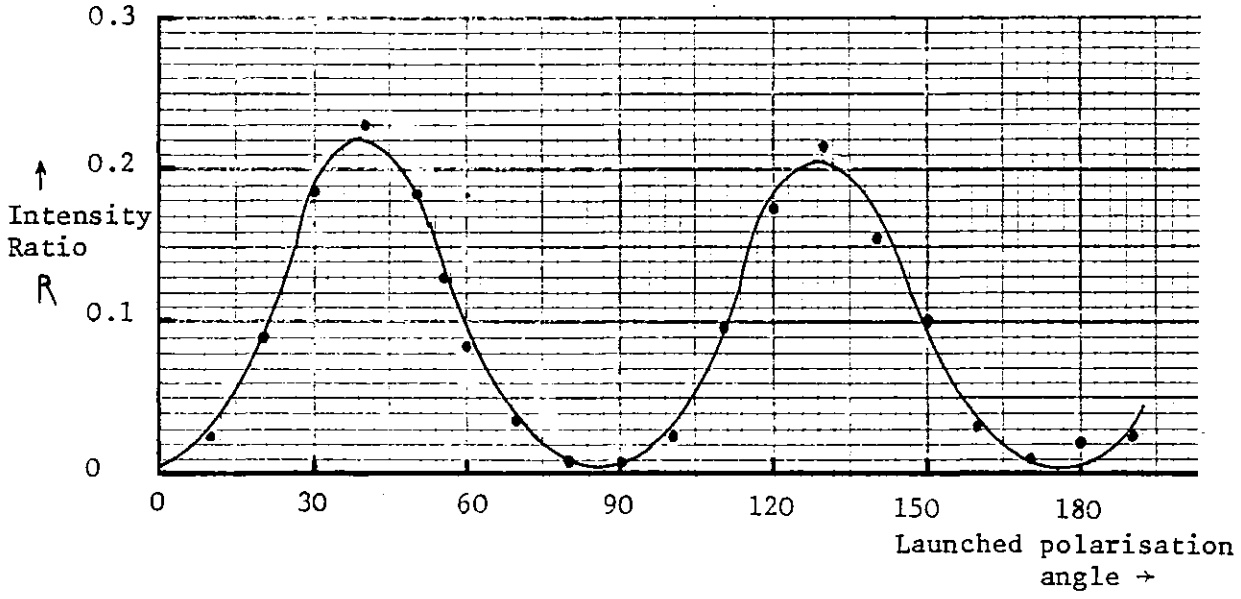

Fig. 3.2 Intensity ratio versus azimuth of launched polarisation for single mode fibre

The peak intensity ratio for the fibre concerned yielded the phase retardation produced by that fibre, as shown in equation 3.3 above. This value of phase retardation was then plotted as a point on a graph of phase retardation against fibre length.

The difference between the orientation of the major axis of the output ellipse and the input linear polarisation orientation was also plotted against this input orientation. Attention to this angle served as a double check on errors in measurements, which were in some cases very difficult to gauge accurately. The theoretical relationship between the input polarisation direction and that of the output ellipse major axis has been investigated by Born and Wolf[13] and is given as:

$$\text{Tan } 2\psi = (\text{Tan } 2\phi) \cos\delta \qquad 3.4$$

This is illustrated in figure 3.3, where X and Y are the privileged axes of the fibre and OP represents the amplitude of the linearly polarised launched-wave's electric vector. The vector may be resolved into two components along the privileged axes. These components remain

bound to the privileged axes and fixed in amplitude, but their relative phase changes until at the output end of the fibre the polarisation ellipse is as shown.

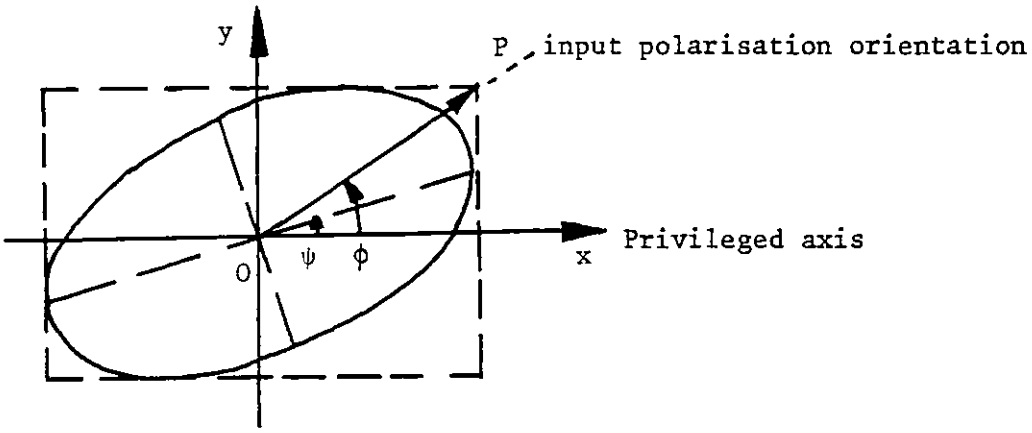

Fig. 3.3 The relation between input polarisation, privileged axes and output ellipse of a retarder

With the phase shift calculated as above, it was possible to calculate the expected orientations of the ellipse major axes for all measurements for comparison with measured values, as shown in figure 3.4. The extra polarisation shift was then the optical activity of the fibre.

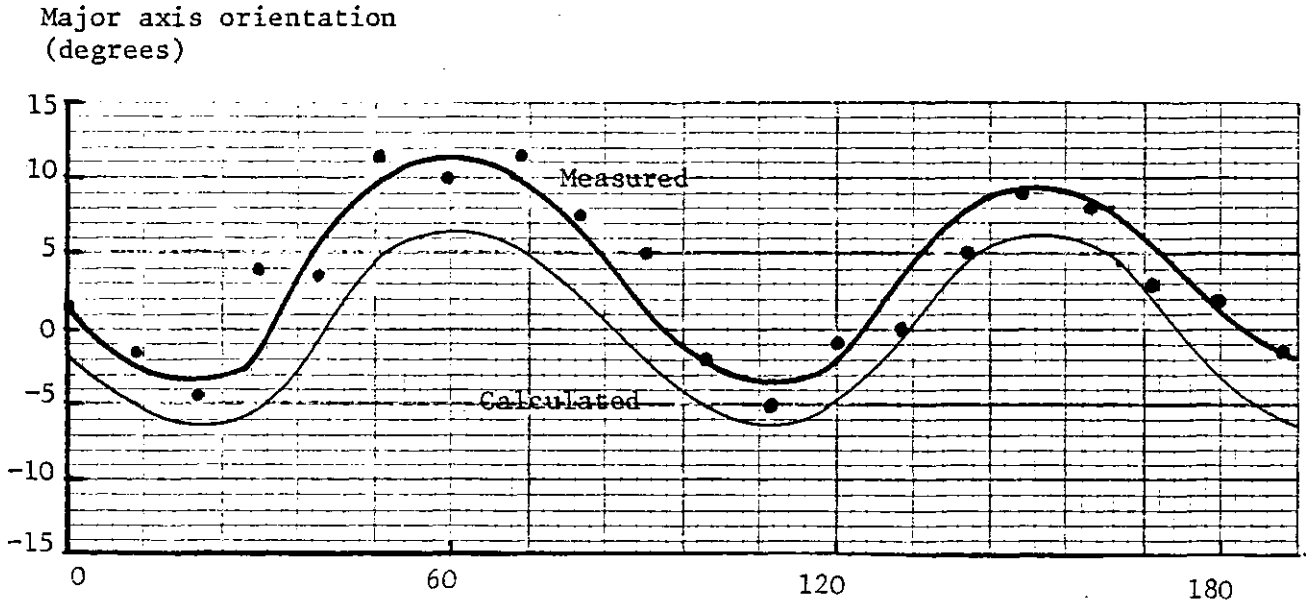

Fig. 3.4 Major axis orientation v. azimuth of launched polarisation

When measurements had been completed on a single piece of fibre, the fibre was then cut shorter and the entire test run was repeated. This procedure was continued until the fibre was so short that further measurements were impractical.

3.1.4 Experimental arrangement

An optical fibre was laid on the specially prepared flat, level surface of a wooden beam so that the fibre was perfectly straight and unstressed. Laser light was launched into this fibre by means of a x45 microscope objective, the light having been passed through a prism polariser. It was necessary to position the fibre to a fraction of a micron for good launching. With normal triaxial micrometer driven micromanipulators, this accuracy is very difficult to attain; merely touching the adjustment knob lightly is liable to deflect the structure by this amount.

Accordingly, a better launching arrangement was sought and a novel solution was adopted. It is possible to use stereophonic pickup cartridges of the moving magnet type as micropositioning units by feeding them with electric currents. The forces associated with the resulting stylus movements are miniscule, but are sufficiently large to move optical fibres of the size used here.

The launcher arrangement is shown in figure 3.5. The fibre enters the launcher at the rear through a hole and is supported on a card support which bridges the distance between the main fibre support and the launcher platform. The launcher platform supports the fibre for 4 cm and this section is normally covered in high index liquid beneath a microscope cover glass so as to strip out unwanted cladding modes. The launcher platform is level with the stylus platform, which is a small piece of 'minimagnet' material and together with another similar piece of material forms a magnetic clamp which holds the fibre end firmly without greatly stressing it. For the major part of the tests, the fibre was glued down to the launcher platform with collodion so that the launching face would be static over as many test runs as possible. The cartridge launcher assembly is screwed to a standard

triaxial micromanipulator which provides a coarse adjustment. The supply to the cartridge is made by a cable carrying the left and right signal voltages and neutral supply, and these are connected to independently variable constant voltage sources so as to give movement independently in two directions at the stylus. The entire assembly is mounted on a double stem optical bench carrier to reduce the possibility of relative movement between the lens and launcher.

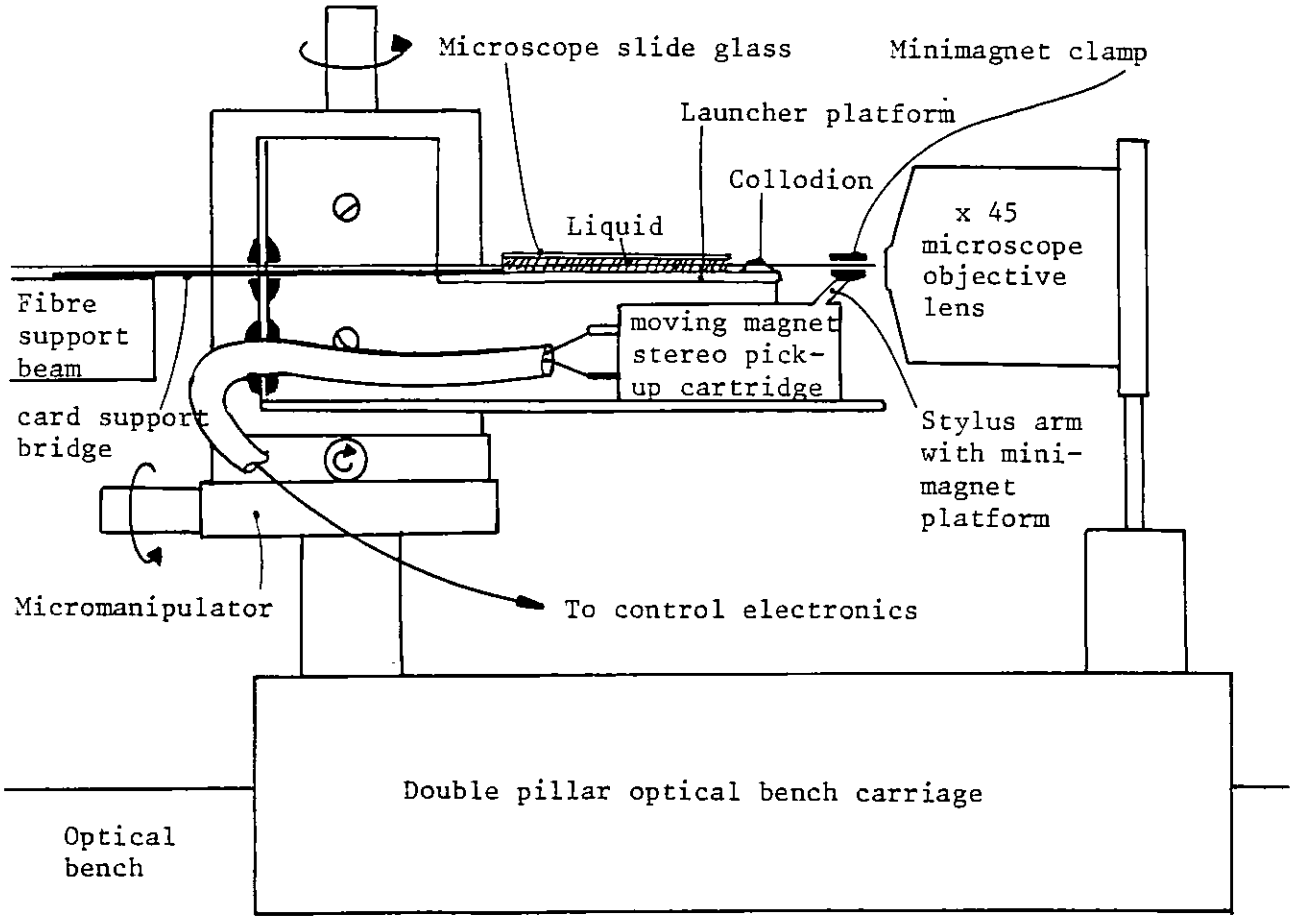

Fig. 3.5 Monomode fibre launcher

The cartridge chosen for this application was a moving magnet cartridge (type Shure M44). The circuit used for controlling the cartridge was a straightforward dual output dc voltage source. Each output was taken directly from a 741 operational amplifier voltage

follower driven from a potential divider comprising fixed resistors and two potentiometers of very different value to allow independent coarse and fine control of stylus position on each axis. The circuit diagram is shown below:

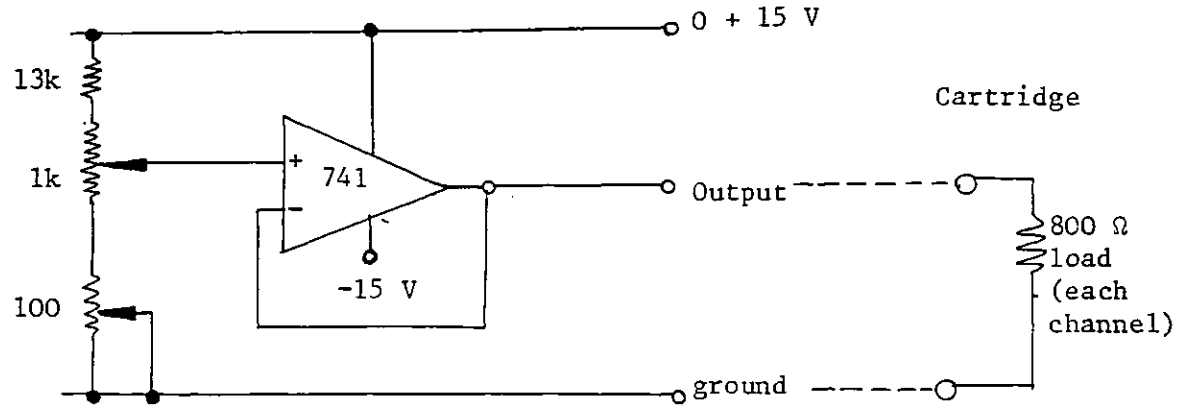

Fig 3.6 Cartridge controller

The sensitivity of the cartridge to applied voltage was measured at dc with a microscope and measuring eyepiece. The movement on each axis was approximately linear with voltage until about 1.5 V, the displacement being non-linear above this value. The useful range of movement was about ± 5 µm on each axis with the circuit shown above. No more than 1 volt was supplied to each channel so as to keep power dissipation in the cartridge safely low. The displacement/ voltage characteristics of the cartridge are shown below:

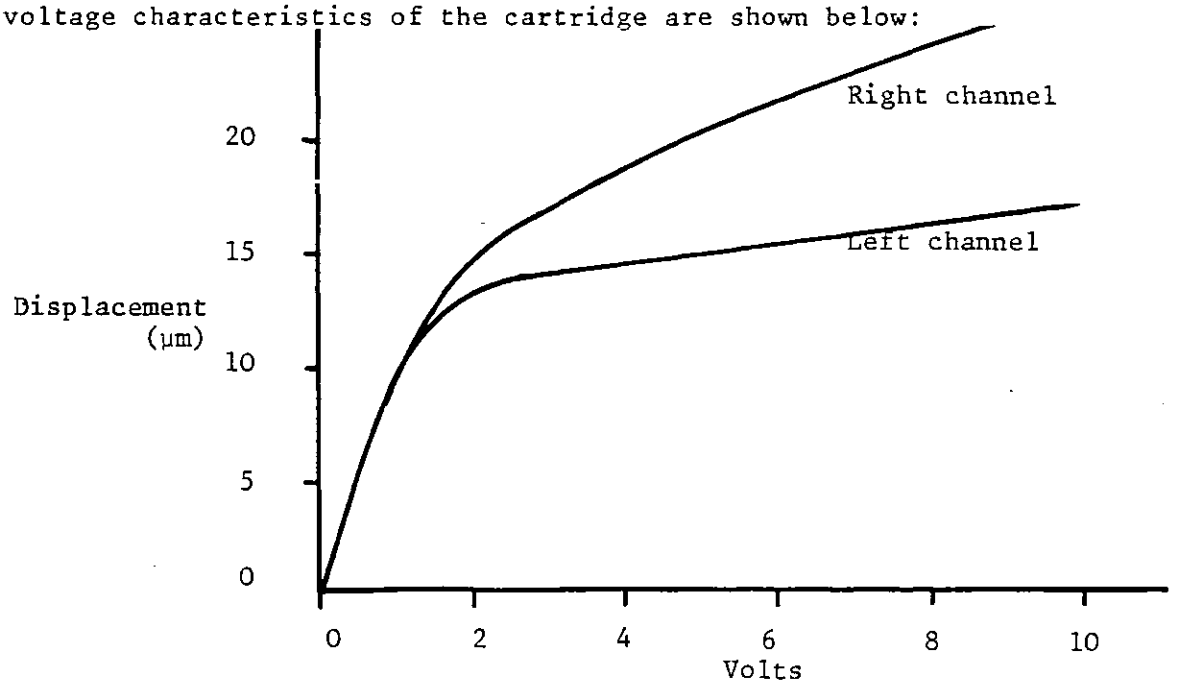

Fig. 3.7 Stylus displacement v. applied voltage for Shure M44

The launcher proved invaluable for providing stable, repeatable launching conditions over long periods. The accuracy is more than satisfactory and there is the additional benefit that the stylus mounting provides isolation from vibration at other parts of the bench. The final attraction of this device is its extreme cheapness.

The analysis of the fibre's light output was accomplished (after further cladding mode stripping at the output end) by collecting the light output with a collimating lens focussing through a quarter wave plate and polarisation analyser onto a screen.

Figure 3.8 shows the complete optical arrangement.

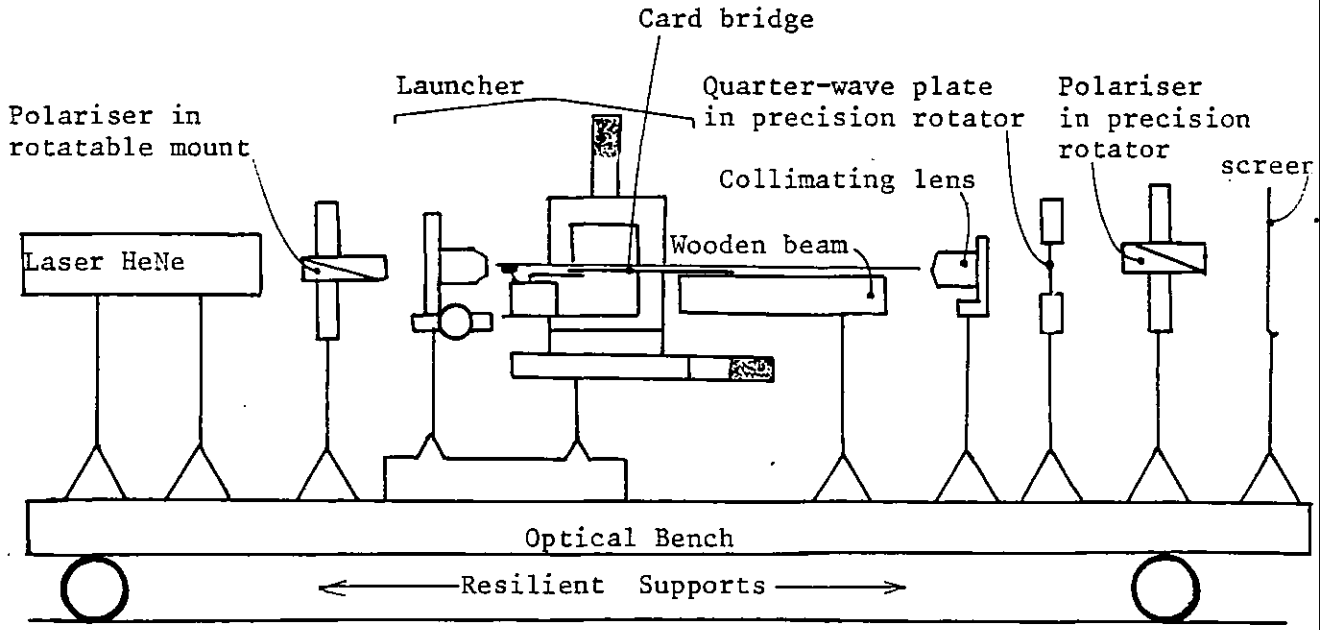

Fig. 3.8 Optical layout for fibre polarisation experiments

3.1.5 Limitations of experiment

The extreme limits of fibre length which can be investigated by the arrangement are set at the high end by fibre strength and at the low end by the intrusion of cladding modes. Long fibres of the sizes used here need extreme care if they are to be handled without breakage.

Several opportunities for measurement were lost by premature breakage of the fibre in this experiment. For short fibres, it is impossible to take repeatable, stable readings from fibres below about 10 cm in length due to the interference between ineradicable cladding modes and core light. It is not possible to remove cladding modes even with normally efficient mode stripping liquids over such short lengths and this is why the results reported here stop at this length.

The accuracy of the readings themselves is limited firstly by the polarisation quality of the optical components used. Initially, several sets of measurements were lost because the predominant birefringent element in the optical system was the collimating lens. The second accuracy limit is due to the precision of alignment between the transmission axes of the two polarisers and the privileged axes of the quarter-wave plate. Misalignment results in lack of symmetry over a 180° set of measurements.

For phase shifts in the region of 45°, the eye itself is unable to distinguish precise transmission minima, and so there is more variability in results in this area.

A further limitation of the experiment was the amount of time required to make measurements; each length of fibre took a day to characterise.

3.1.6 Results

The overall phase retardation, R, privileged axis orientation, ϕ, and optical activity, Ω, of the fibre when cut for measurement are displayed as figures 3.9, 3.10 and 3.11 respectively.

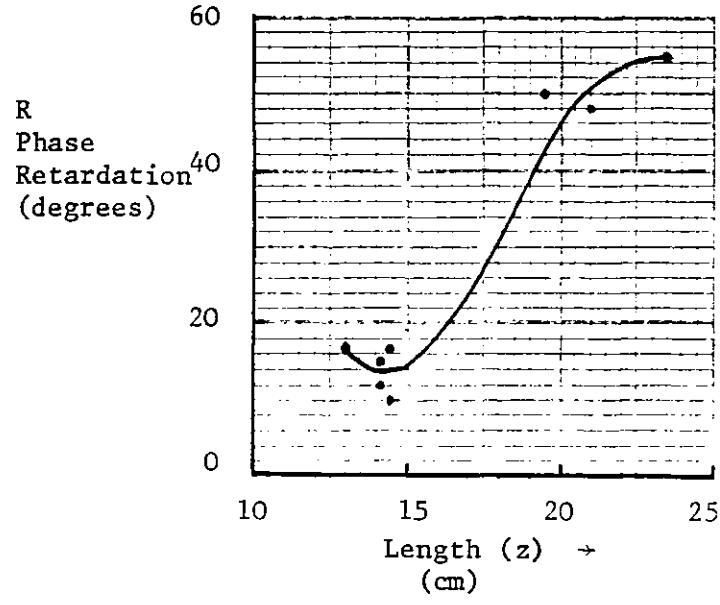

Fig. 3.9 Phase retardation v. fibre length.

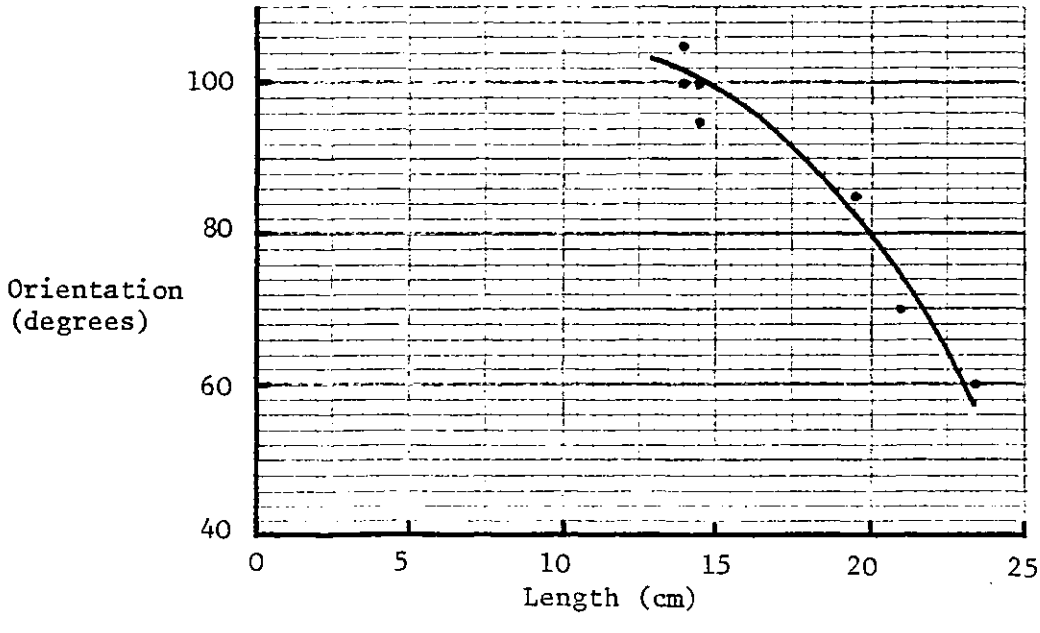

Fig. 3.10 Position of privileged axis v. fibre length

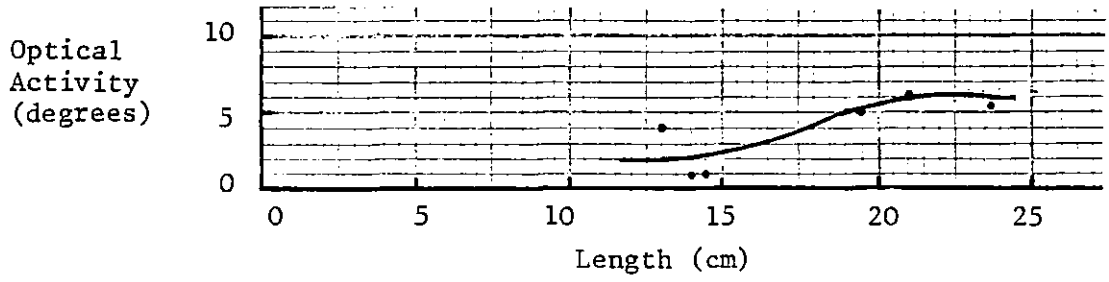

Fig. 3.11 Optical activity v. fibre length

3.2 Analysis of results for measured fibres

3.2.1. Analysis by the Jones calculus

The results in the preceding section were analysed using the Jones calculus in a manner described by Kapron and Keck[1] in order to find the local variation of the birefringent properties of the tested fibre.

The Jones calculus represents a beam of polarised light by means of a two-element column vector representing the orthogonal, transverse components of the electric field directed along a pair of chosen axes which we conventionally label x and y. Normally, these components are written with the time dependent $e^{i\omega t}$ omitted for brevity. Phase relations are preserved, however, by expressing the two vector elements in complex form. Thus the general full Jones vector is written[14]:

$$\begin{bmatrix} E_x\, e^{id} \\ E_y\, e^{iB} \end{bmatrix} \qquad 3.5$$

Transformation between different polarisations is accomplished mathematically by modelling retarders with, in general, four element matrices describing their properties. The effect of linear and circular retarders acting on a beam of light with initial polarisation $\begin{bmatrix} E_x \\ E_y \end{bmatrix}$ is then written as:

$$\begin{bmatrix} \bar{E}_x \\ \bar{E}_y \end{bmatrix} = \begin{pmatrix} A & -B^* \\ B & -A^* \end{pmatrix} \begin{bmatrix} E_x \\ E_y \end{bmatrix} \qquad 3.6$$

where:

$A = \cos R/2 \cos \Omega + i \sin R/2 \cos (2\phi + \Omega)$

$B = \cos R/2 \sin \Omega + i \sin R/2 \sin (2\phi + \Omega)$

Here we assume a linear retardance, R, with fast axis orientation, ϕ, followed by a circular retarder producing angular rotation, Ω. These macroscopic equations hold for an arbitrary length of optical path and if this is shrunk to an infinitesimal section of length, Δz, say, these values of retardance become local for that section. We now introduce the local retardance per unit length $r(z)$, rotation per unit length $\omega(z)$ and fast axis angle $\theta(z)$. Obviously for our section, $R = r(z)\Delta z$, $\Omega = \omega(z)\Delta z$ and $\phi = \theta(z)$. These expressions may be substituted into 3.6 to gain the Jones matrix of each section and then we can find an expression for the matrix of the whole fibre of length L by integrating the contributions from all the infinitesimal sections of the retarder. This matrix is of the form 3.6 with the relations[1]:

$$A = \cos \lambda + i\, C\, \frac{\sin\lambda}{\lambda}$$

and $$B = (i\, S + \gamma)\, \frac{\sin\lambda}{\lambda} \qquad 3.7$$

where $$\lambda(L) = (C^2 + S^2 + \gamma^2)^{\frac{1}{2}}$$

$$\gamma(L) = \int_0^L \omega\,(z)\, d\, z$$

$$\begin{bmatrix} C(L) \\ S(L) \end{bmatrix} = \frac{1}{2} \int_0^L r\,(z) \begin{bmatrix} \cos 2\theta(z) \\ \sin 2\theta(z) \end{bmatrix} dz \qquad 3.8$$

Since the macroscopic matrix for the whole fibre must be equal to the integrated matrix for the infinitesimal sections, we find:

$$C = \frac{\lambda}{\sin\lambda} \sin R(L)\cos(\phi(L)+\Omega(L))$$

$$S = C \tan\left(\phi(L)+\Omega(L)\right)$$

$$\gamma = \lambda q \text{ with } q = \frac{\cos R(L) \tan \Omega(L)}{\sqrt{\sin^2 R(L)+\tan^2\Omega(L)}} \qquad 3.9$$

$$\text{and } \lambda = \tan^{-1}\left\{\frac{\tan \Omega(L)}{q}\right\}$$

Finally, we can find the local values of specific retardance etc. by substitution between 3.8 and 3.9:

$$r(z) = 2\left[\left(\frac{dC}{dz}\right)^2 + \left(\frac{dS}{dz}\right)^2\right]^{\frac{1}{2}}$$

$$\theta(z) = \frac{1}{2} \tan^{-1}\left[\frac{dS}{dz} \Big/ \frac{dC}{dz}\right] \qquad 3.10$$

$$\omega(z) = \frac{d\gamma}{dz}$$

3.2.2 Local characteristics of the measured fibre

The relations of the preceding section were used in the following way. A range of eleven equispaced data points were chosen between 13 cm and 23 cm along the tested fibre. R, Ω and ϕ were tabulated for each point, and from these C, S, and γ were calculated as defined in equations 3.9. Graphs of each of these were then drawn and the slope of each at every data point was found by carefully drawing tangents to these curves in the appropriate places. (The tabulated values and graphs are recorded in Appendix I.) This method was used rather than numerical differentiation as it was difficult to estimate the size of the errors involved in using the associated finite difference techniques. Having thus obtained dC/dz, dS/dz and $d\gamma/dz$, the values of local specific retardance r(z), local fast axis orientation $\theta(z)$ and local optical activity $\omega(z)$ were calculated at each data point using the formulae 3.10 and they are plotted as figures 3.12, 3.13 and 3.14 respectively.

These results disclose that the local birefringence is subject to a large variation even over short distances in this type of fibre. However, there does appear to be a particular defect between 15 and 16 centimetres in the measured fibre, and this is contributing significantly to the overall retardation in the sample. At the same time, the fast axis is spinning at a roughly constant rate of 13 radians per metre, giving a full rotation every half metre. This length coincides roughly with the circumference of the drum onto which the fibre was drawn during production and it is conjectured that there may be a direct connection between the winding drum size and the rotation rate of anisotropic axes in these fibres. The optical activity of the fibre is small and also is not prone to dramatic variation.

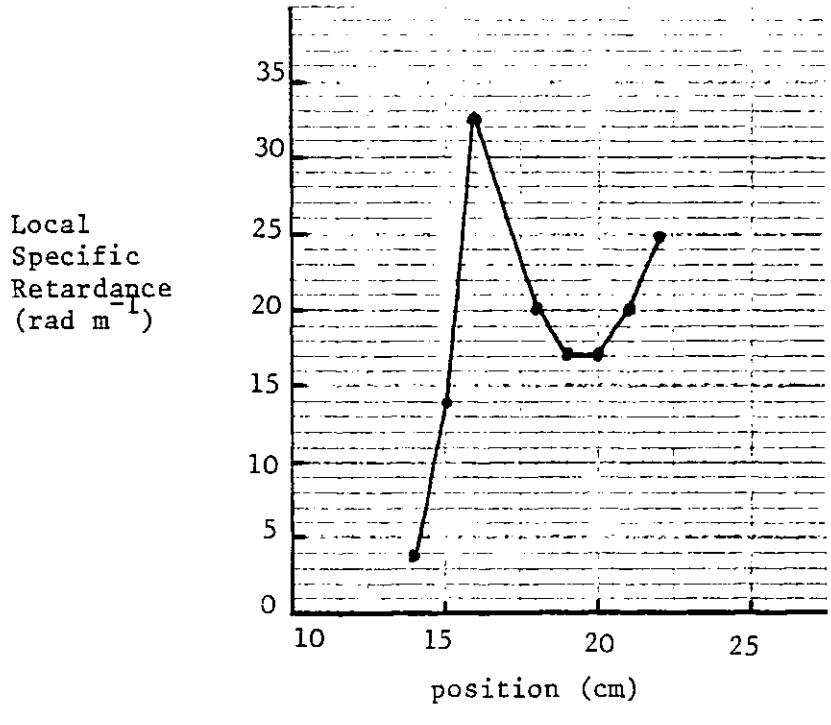

Fig. 3.12 Local specific retardance v. position along fibre

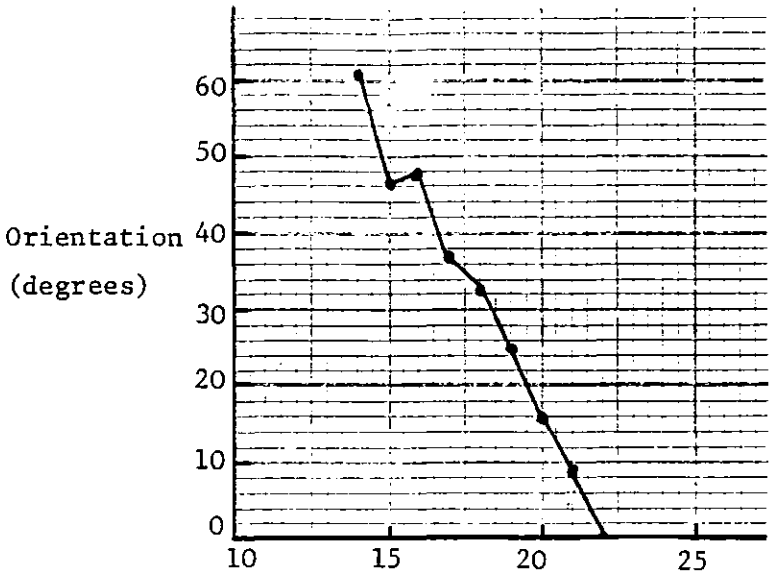

Fig. 3.13 Orientation of fast axis within fibre

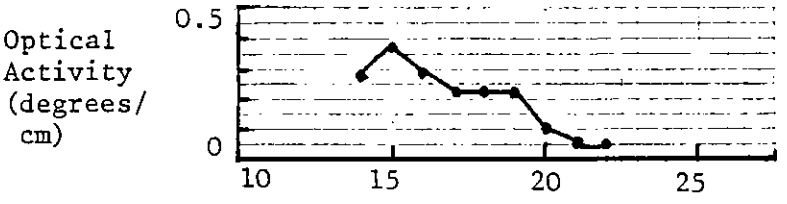

Fig. 3.14 Local optical activity of fibre

3.2.3 Comparison with results for other fibres

Since this work was done, there has been a considerable upsurge of interest in this subject. Many laboratories have now reported polarisation measurements on single mode fibre[1,6,15-17].

Birefringence and privileged axis rotation have been observed by all workers on single mode, solid core fibres. Often the measured birefringence lies between one and several tens of radians per metre. From the foregoing, it is clear that double crucible drawn fibre has been shown to perform to a standard which is not unusual for typical fibres produced by CVD. The origins of this birefringence are examined in section 3.3 and these include process-dependent variables.

Recently, there have been efforts made to eliminate the process induced birefringence of fibres and this work has been very successful. This performance was initially gained by paying attention to preserving core circularity during deposition and collapse and by matching the core and cladding expansion coefficients and viscosities, thus considerably reducing the thermal stresses in these fibres. However, further work[18] showed that, by rotating the preform during pulling, it is possible to eliminate almost perfectly the cumulative effect of any residual anisotropy in the preform, leading to fibre with birefringence below measurable limits.

Although the sources of linear birefringence and privileged axis rotation have obviously been very fully explored, the origin of optical activity in unstressed fibres was not at the time explained by any published work, and it occurred to the author to question whether a possibility existed whereby polarisation might be weakly bound to the privileged axes. This led to the proposal for an optical fibre where the birefringence is deliberately enhanced, rather than reduced, in order to hold a stable, linear polarisation.

3.3 Mechanisms of polarisation change in optical fibres

There are four classes of effects which can influence the polarisation of light travelling in single mode fibres. These are stresses, electro-magnetic fields, core geometry problems and mechanical deformation of the fibre. We will briefly examine the first two effects and then go on to consider the remaining two in a little more detail.

3.3.1 Stress

Stresses in optical fibres can arise both as an unavoidable consequence of the fibre manufacturing process and as a result of external loads placed on the fibre. In the first case, thermal stress normally exists in optical fibres because the core and the cladding have different expansion coefficients and transition (setting) temperatures. Normally the cladding of an optical fibre is made of silica which sets at a high temperature (circa 1615° C) while the core, which is normally doped with germania, is still molten. When the core solidifies (circa 1400° C) thermal stress begins to build up between the core and cladding as the fibre cools to room temperature. Under perfect conditions the stress pattern would be isotropic in the core, but under real conditions, non-uniform quenching will often distort this and lead to an anisotropic stress pattern. This will then lead to stress birefringence via the elasto-optic effect.

We can estimate the plausibility of this theory by calculating the expected thermal stress level in a typical silica based single mode fibre designed for communication applications. Such fibres normally possess a deposited optical cladding having a refractive index very close to, but slightly lower than, that of silica to avoid secondary guidance effects. Normally fibre cores are made from germano-silicate glass. To arrive at the total thermal stress in such a fibre, we need to know the relations between refractive index, doping concentration and expansion coefficient. This information has been published for the germania-silica system[2]. Using this, we find that for a typical fibre having an index difference of 10^{-2} (0.7%) the doping level in the core will be approximately 7 mole% germania. The resulting

difference in thermal expansion coefficients between the core and cladding is about 10^{-6}/° C. The thermal strain between the core and cladding starts to build up when the core solidifies at about 1400° C and so at room temperature the difference in the unstrained sizes of the core and cladding will therefore be about 7×10^{-4} x core size. Using a value of Young's Modulus for silica[3] of 7.33×10^{3} kgmm^{-2} we arrive at a value for the thermal stress in the fibre of 5 kg mm^{-2} (assuming that the core and cladding are equally strained). In practice this is likely to be a conservative estimate of the strain since many of the important thermal and mechanical parameters are temperature dependent and because stress in fact starts to build up before the core solidifies. However, accepting this estimate in order to get an order of magnitude estimate of the index change caused by this strain, we now use the pressure coefficient of refractive index for silica to calculate the full index modification due to the thermal strain, which is assumed to be hydrostatic in the core. The value of this coefficient[4] is 9.1×10^{-5} mm^{2}kg^{-1}, yielding a value of 4.6×10^{-4} for the thermally induced modification of the core refractive index. The maximum intrinsic local phase retardations reported elsewhere are of the order of 100 radians per metre, equivalent to a refractive index difference of around 10^{-5} for two orthogonal polarisations. This is equivalent to about two percent of the total stress modification, and it is not hard to imagine that slight thermal asymmetries during quenching might easily result in this degree of anistropic stress.

The second source of stress in fibres, external loading, can be estimated also. Typically, the outer diameter of an uncoated silica communications fibre is 125 microns. Imagine a fibre subjected to an evenly distributed transverse load of x kg per mm of fibre. If we take the crude assumption of an isotropic, linear stress field in the fibre, the transverse stress at the core will be given by (x/0.125)kg mm^{-2}. The relative photoelastic constant of silica is given[4] as 3.5×10^{-5} mm^{2}kg^{-1}. To get a birefringence of 10^{-5} in refractive index, we find that the required value of x is only 36 g mm^{-1} loading on the fibre. This is not high, and might easily be produced by clamping of the fibre in an optical system. Thus care should be taken to arrange clamping forces properly if natural fibre birefringence is not to be severely modified in experimental systems.

3.3.2 Electro-magnetic fields

The modification of polarisation in fibres by magnetic fields has already been thoroughly examined in chapter one, and no more need be said here.

Electric fields can also modify polarisation in silica fibres by means of the electro-optic Kerr effect. Transverse electric fields in the fibre cause birefringence in the material. For silica this effect is very small (the Kerr constant for silica is 9×10^{-15} cm V^{-2}) and polarisation changes due to this effect are unlikely to be often seen. However, this effect has been used to detect the polarisation state in single mode fibres[6] and the linear electro-optic effect might be put to use for measurement of electric fields if a suitable fibre material can be found.[7]

3.3.3 Core shape

We saw in section 2.7 that the propagation constant of the mode in a perturbed single mode guide is described by the equation 2.25, re-stated here for convenience:

$$\beta_{t1} = \pm (\beta_1^2 + 2 i \beta_1 K_{11})^{\frac{1}{2}}$$

We saw also in section 2.6 that the coupling coeffient $K_{\mu\nu}^{(p,q)}$ consists of two parts, corresponding to the separate effects of the longitudinal and transverse fields of the individual modes. If we label these two parts separately, we may express the coupling coefficient as:

$$K_{\mu\nu}^{(p,q)} = p \overline{K}_{\mu\nu} + q \overline{k}_{\mu\nu} \qquad 3.11$$

with

$$\overline{K}_{\mu\nu} = \frac{\omega\varepsilon_o |\beta_\mu|}{4iP\beta_\mu^{(p)}} \iint_{-\infty}^{+\infty} (n^2 - n_o^2) \underset{\sim}{\mathcal{E}}_{\mu t}^{*} \cdot \underset{\sim}{\mathcal{E}}_{\nu t} \, dx \, dy$$

and

$$\overline{k}_{\mu\nu} = \frac{\omega\varepsilon_o |\beta_\mu|}{4iP\beta_\mu^{(p)*}} \iint_{-\infty}^{+\infty} \frac{n_o^2}{n^2} (n^2 - n_o^2) \underset{\sim}{\mathcal{E}}_{\mu z}^{*} \cdot \underset{\sim}{\mathcal{E}}_{\nu z} \, dx \, dy$$

If we substitute this separated expression for $K_{\mu\nu}$ into 2.24, we get

$$\beta_{t1} = \pm \beta_1 \left[1 + \frac{i(\bar{K}_{11} + \bar{k}_{11})}{\beta_1} \right] \qquad 3.12$$

Thus β_1, the propagation constant in the ideal guide, is modified by an additive value which we will express as $\Delta\beta$ $(= i\,(\bar{K}_{11} + \bar{k}_{11}))$ due to the perturbation. We will call that part of $\Delta\beta$ which differs for the two polarisations $\Delta\beta_p$.

The first obvious conclusion which we can draw from this analysis is that the coupling coefficient, $\bar{K}_{11}$, cannot contribute to $\Delta\beta_p$ since we know that the fundamental mode transverse fields are linearly polarised. Clearly, the two possible orthogonal polarisations must everywhere have a vanishing scalar product.

We are led to the conclusion that any differences in the propagation constants for orthogonal polarisations must arise through coupling of the longitudinal fields. We now return to our expression for $\bar{k}_{\mu\nu}$ and insert the appropriate expressions for the parameters. First, we convert the expression for use in polar co-ordinates, as this simplifies calculations:

$$\Delta\beta_p = j\,k_{11} = \frac{\omega\varepsilon_o}{4iP}\int_o^{\infty}\int_o^{2\pi}\left(\frac{n_o}{n}\right)^2 (n^2-n_o^2)\,\underset{\sim}{\mathcal{E}}_{1z_{//}} \cdot \underset{\sim}{\mathcal{E}}_{1z_{\perp r}}\; r\,d\,r\,d\,\phi \qquad 3.13$$

We also take the core deformation as being expressible in terms of a sum of azimuthal harmonics such that the core boundary is determined by:

$$r\,(x, y) = a + \sum_m p_m \cos\,(m\phi + \psi_m) \qquad 3.14$$

Since the perturbation index is always equal to the difference between the core and cladding indices, n_1 and n_2, we can take all references to index difference outside the integrals and simply employ $(n_1^2 - n_2^2)$ as a multiplying factor in all perturbed regions. Also, in the spirit of the weakly guiding approximation, we take $n_1/n_2 = 1$.

For the field expressions, we use the fundamental mode longitudinal fields described equation 2.15. Allowing for the orthogonality of transverse polarisation, we have within the core:

$$E_{z_{//}} = \frac{Ai\kappa J_1}{\beta_1} (\kappa r) \sin \phi$$

$$E_{z_{\perp r}} = \frac{-Ai\kappa J_1}{\beta_1} (\kappa r) \cos \phi \qquad 3.15$$

We have chosen the A's here as equal so that both polarised modes are carrying the same power, but this is for convenience only.

Finally, for small perturbations, we will take the E_z as being constant throughout the perturbed region and equal to the value at r = a. This fairly crude approximation gives:

$$\Delta\beta_p = j\,\bar{k}_{11} = \frac{\omega\epsilon_o}{4iP} (n_1^2 - n_2^2) \frac{A^2 \kappa^2 J_1^2(\kappa a)}{\beta_1^2}$$

$$\times \int_o^{\infty} \int_o^{2\pi} p_m \cos(m\phi + \psi_m) \sin\phi \cos\phi \times r\, dr\, d\phi \qquad 3.16$$

Taking advantage of normalisation relations between A and P[8] and treating only one harmonic of the perturbation, we find:

$$\Delta\beta_p = j\,\bar{k}_{11} = \frac{\kappa^2\gamma^2 p_m}{2\pi\, a\, n\, k\, \beta^2} \int_o^{2\pi} \sin\phi \cos\phi \cos(m\phi + \psi_m)\, d\phi \qquad 3.17$$

We find that, if Ψ_m is zero, the integral vanishes for all m, but if $\Psi_m = \pi/2$, the integral will have a finite value, $\pi/2$, when m is 2. This shows that only elliptical deformation of the core boundary will introduce a difference between the propagation constants of the orthogonally polarised modes.

In addition, we can deduce one more important result from the above equation. For a fixed value of V, $\sqrt{(k_1^2 - k_2^2)}$ is inversely proportional to a. Therefore $(\kappa a)^2$ and $(\gamma a)^2$ will be almost constant. Also, $\beta/k \simeq n$, which is also virtually constant. We manipulate 3.17 then to find:

$$\frac{}{\Delta\beta} = \frac{\Delta\beta_p}{\beta} = \frac{(\kappa a)^2\ (\gamma a)^2\ p_m}{4a^5\ k^4\ n^4} \qquad 3.18$$

This expresses the difference in propagation constants of the polarised modes normalised in relation to β. Also, if we normalise the amplitude of the perturbation to a, by $p_m = pa$, then for a given value of p:

$$\frac{\Delta\beta_p}{\beta} = \left(\frac{(\kappa a)^2\ (\gamma a)^2\ p}{4n^4}\right)\left(\frac{1}{ka}\right)^4$$

$$\propto \left(\frac{1}{ka}\right)^4 \qquad 3.19$$

And remembering $V = ka\sqrt{n_1^2 - n_2^2} \simeq ka\sqrt{2n\Delta n}$ we finally find

$$\frac{\Delta\beta_p}{\beta} \propto (\Delta n)^2 \quad \text{for fixed V and p} \qquad 3.20$$

The importance of this result will emerge in the next chapter.

The analysis we have examined in this section is not completely accurate because of the various approximations we have made en route, but nevertheless the basic relationships pointed out here do hold true in practice. For a precise numerical prediction of $\Delta\beta$ for a given ellipticity, however, more rigorous analyses are necessary, and very many attempts to produce reliable versions abound in the literature. Most of these are unreliable. However, the results of Tjaden[9], who employed a double power series expansion of the propagation constant with respect to the index difference and perturbation amplitude, appears to give acceptable accuracy. Tjaden's analysis is limited to small ellipticity, but gives good agreement with calculations based on the exact analysis for arbitrary ellipticity which will be examined in the next chapter.

3.3.4 Mechanical deformation of fibres

The case of deformation resolves into two separate instances: bending and twisting. At the time when the experimental work described in this chapter was being done, there were no explanations of these effects in the literature.

In an attempt to explain this bending effect, the author applied the perturbation theory exposed earlier to examine the effect of the perturbation of the core boundary during bending, which contains a small asymmetrical component. This produced a result which was many orders of magnitude too small to explain observed results and was linear with the fibre curvature. Observed birefringence is proportional to the square of the curvature[10]. A further attempt was made to explain this effect using the earlier work but allowing for the deformation of the mode field at the bend[11]. This also gave a result which was several orders of magnitude too small, but which had the correct square-law relation to the curvature.

More recently, Ulrich has shown that both the bending and twisting effects can be explained by stress in the fibre material[19,20].

References to Chapter III

1. KAPRON, F. P., BORELLI, N. F., KECK, D. B.
"Birefringence in dielectric optical waveguides"
IEEE Jnl Quantum Electronics 8:2 (Feb 72), pp. 222-5

2. HUANG, Y. Y., SARKAR, A., SCHULTZ, P. C.
"Relationship between composition, density and refractive index for germania-silica glasses"
Jnl. Non-Crystalline Solids 27 (1978), pp. 29-37

3. MALLINDER, F. P., PROCTOR, B. A.
"Elastic constants of fused silica as a function of large tensile strain"
Phys. Chem. Glasses 5:4 (August 64), pp. 91-103

4. PRIMAK, W., POST, D.
"Photoelastic constants of vitreous silica and its elastic coefficient of refractive index"
J. Appl. Phys. 30:5 (May 59), pp. 779-788

5. SCHERER, G. W.
"Stress induced index profile distortion in optical fibres"
Applied Optics 19:12 (15 June 80), pp. 2000-2006

6. SIMON, A., ULRICH, R.
"Evolution of polarisation along a single mode fibre"
Appl. Phys. Lett. 31:8 (15 Oct 77), pp. 517-520

7. ROGERS, A. J.
"Optical transducers for power system electrical measurements"
Lecture delivered at IEE London, 3 December 80, unpublished.

8. MARCUSE, D.
"Theory of dielectric optical waveguides", pp. 69-70
London; Academic Press; 1974

9. TJADEN, D. L. A.
"Birefringence in single mode optical fibres due to core ellipticity"
Philips J. Res. Vol. 33, pp. 254-263 (1978)

10. SMITH, A. M.
"Birefringence induced by bends and twists in single mode optical fibre"
Applied Optics 19:15 (1 Aug. 80), pp. 2606-2611.

11. GAMBLING, W. A., MATSUMURA, H., RAGDALE, C. M.
"Field deformation in a curved single mode fibre"
Electronics Letters 14:5 (2 March 78), pp. 130-132

12. PAPP, A., HARMS, H.
"Polarisation optics of index gradient optical waveguide fibres"
Applied Optics 14:10 (Oct 75), pp. 2406-2411

13. BORN & WOLF
Principles of Optics
Pergamon, Oxford, 1975

14. See, for example, SHURCLIFF, W. A.
"Polarised light, production and use"
Oxford University Press; London; 1962

15. GAMBLING, W. A., PAYNE, D. N., MATSUMURA, H.
"Birefringence and optical activity in single mode fibre"
Optical Society of America Topical Meeting on Optical Waveguides II, Williamsburg, Va. 1977

16. RAMASWAMY, V., STANDLEY, R. D., SZE, D., FRENCH, W. G.
"Polarisation effects in short length, single mode fibres"
BSTJ 57:3 (March 78), pp.635-651

17. SMITH, A. M.
"Polarisation and magneto-optical properties of single mode optical fibre"
Applied Optics, Vol 17 (1978), pp. 52-56

18. BARLOW, A. J., RAMSKOV-HANSEN, J. J., PAYNE, D. N.
"Anistropy in spun single mode fibres"
Electronics Letters 18:5 (4 March 82), pp. 200-2

19. ULRICH, R. and SIMON
"Polarisation optics of twisted single mode fibres"
Applied Optics 18:13 (1 July 79), pp. 2241-2251

20. ULRICH, R., RASHLEIGH, S. C., EICKHOFF, W.
"Bending induced birefringence in single mode fibres"
Optics Letters Vol 5:6 (15 June 80), pp. 273-5

CHAPTER IV

ELLIPTICALLY CORED FIBRE FOR POLARISATION MAINTENANCE

This chapter begins by arguing that fibres with very elliptical cores and large refractive index differences should maintain linear polarisation of transmitted light. The exact theory for predicting propagation constants and cut-off wavelengths in such fibres is then examined and qualitative tests on experimental samples of such fibre are reported.

4.1 Proposal of elliptically cored fibres for maintaining linear polarisation

The weakness of the approach of producing perfectly axially symmetrical single mode fibre for polarisation maintenance has already been exposed in chapter one. Even if the effects of core ellipticity and asymmetrical thermal stress are totally eradicated, polarisation modulation by deformations of and stresses placed upon the fibre would destroy its polarisation maintaining characteristics. In use, such modulation could be particularly unfortunate if it was caused by vibrations. A fibre is required where coupling between the orthogonally polarised waveguide modes is suppressed.

Coupling beween modes of propagation is caused by suitable perturbations of the system for which such modes are a solution. Significant coupling will occur over short distances if the perturbations are strong, or, in the case of weak perturbations, if they possess a spatial frequency component which matches exactly the distance required for the two modes to change their relative phase by one full cycle. Under this condition, propagating fields induced by the perturbation will interfere constructively to produce a growing component of coupled energy. One way of suppressing significant coupling then is to produce a system where the propagating modes are travelling with phase velocities sufficiently different as to require a very high spatial frequency from the perturbation. In practice, spatial frequencies of perturbations are found to be weighted strongly towards the low frequencies. The amplitude of perturbations is

commonly found to be almost insignificant for a spatial period (or pitch) less than one millimetre for normal communications fibres. In the case of two orthogonally polarised modes, then, we require to introduce strong optical anisotropy - birefringence - into the fibre sufficient to cause the two polarised fundamental modes to slip in relative phase by one cycle or more in a millimetre. This might be done by producing a fibre with a circular bore in which a biaxial anisotropic crystal has been grown. The main disadvantage of this approach is that in practical terms, the growth of such a crystal inside a fibre for more than a centimetre or so would present very great problems! If such crystal growth were easy, this would offer the possibility of a truly single polarisation fibre where one polarised mode is not merely prevented from coupling to its orthogonal partner, but is absolutely cut off. This would be implemented by arranging that the refractive indices of the crystal straddle that of the cladding glass.

Another method of deliberately introducing anisotropy into a fibre is by producing a very high transverse stress in the core region. At the time that the work described in this thesis was done, there was some relatively unsuccessful work on this approach being pursued elsewhere[2] and since then considerable progress has been made[3], but elliptically cored fibres produced to the designs covered by this thesis have shown better polarisation-holding properties to date[4].

Another possible technique for making anisotropic fibre is by modifying the distribution of refractive index in the fibre's cross section. Various complicated suggestions have appeared recently[5,6,7], but the most obvious way of doing this - the method advocated in this thesis - is to make a fibre with an elliptical core. This type of fibre requires the fewest changes in production methods compared to the various methods suggested elsewhere. At the time the work described in this thesis was done, the proposal for an elliptically cored fibre was the only suggestion for a polarisation maintaining fibre which had been published. A rectangular guide would be the obvious choice in systems with 'hard' electro-magnetic boundaries, but the shape would be difficult to make in fibre form.

4.2 Prediction of the characteristics of the elliptical guide

There exists a foundation of work already done on elliptically cored fibres. It was pointed out in the last chapter that for small ellipticities many approximations have already been published, that of Tjaden (chapter 3 ref 9) appearing to be the most reliable. None of these approximations can be expected to provide accurate solutions for large ellipticities. Analytical solution of the elliptical guide for any ellipticity has been completed independently by Lyubimov et al in Russia[8] and Yeh in the USA[9]. Propagation constants from the exact analysis are only found with difficulty, since it is necessary to apply lengthy numerical techniques to evaluate the solutions from truncated infinite determinants involving Mathieu functions. However, since the difference between the propagation constants for the two orthogonally polarised fundamental modes is of crucial importance to the polarisation-maintaining characteristics of the guide, the effort involved in extracting the propagation constants accurately was judged to be worth while. Accordingly, Yeh's analysis will be summarised next and a universal set of curves for the difference between the propagation constants for the two polarised fundamental modes will be presented. Next the cut-off conditions for this type of guide will be examined and the depolarisation mechanism will be briefly discussed.

4.2.1 Electro-magnetic theory for the propagation constants of an elliptical dielectric waveguide

(i) Specifying the problem

We tackle the problem of analysing the elliptical dielectric waveguide in a similar fashion to that adopted for the circular waveguide. With the same assumptions of an infinitely long, straight guide with the cladding material extending transversely to infinity we assume the core material to have dielectric constant ε_1 and the cladding ε_2. Both media have the magnetic permeability of a vacuum, μ, and of course we assume $\varepsilon_1 > \varepsilon_2$. We chose elliptical cylinder co-ordinates, ξ, η, z, since they suit the geometry of the problem. The use of these co-ordinates is displayed in figure 4.0. The system consists of a set of confocal elliptical cylinders with their common central axis forming the z direction.

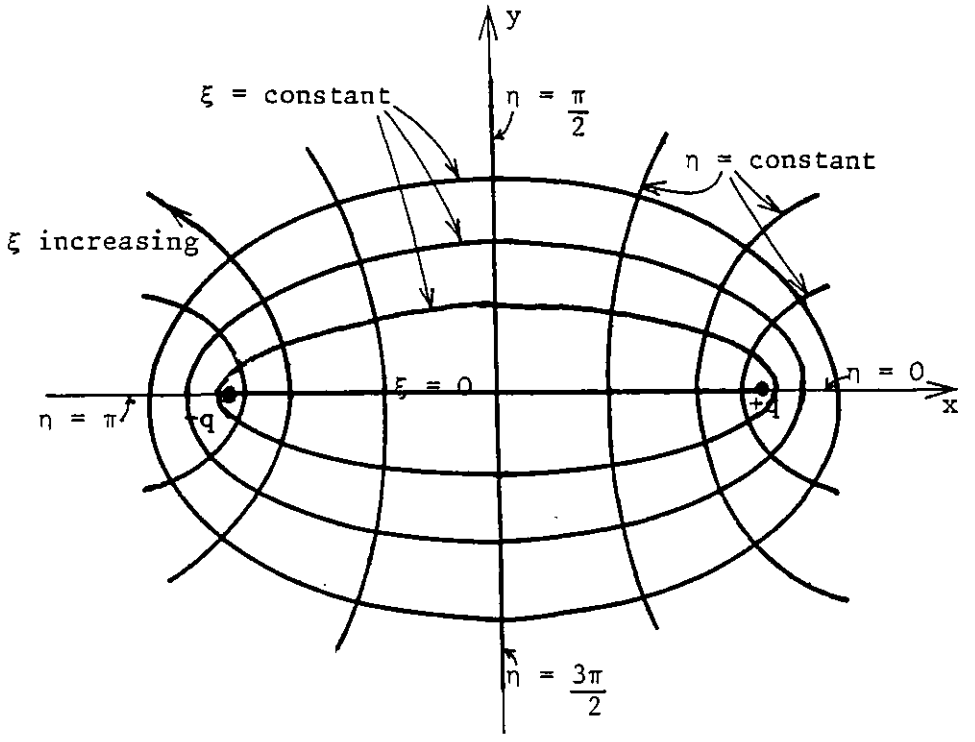

Fig. 4.0 Use of elliptical cylinder co-ordinates

Rectangular Cartesian co-ordinates are expressed in terms of these elliptical co-ordinates in the following manner:

$$\begin{aligned} x &= q \cosh \xi \cos \eta \\ y &= q \sinh \xi \sin \eta \\ z &= z \end{aligned} \qquad 4.1$$

where $0 \leq \xi < \infty$ and $0 \leq \eta \leq 2\pi$ and q = semifocal length of ellipse.

The value of ξ determines the ellipticity of the cylinder while q determines the scale of the system. One of the elliptic cylinders, $\xi = \xi_o$, is chosen to coincide with the boundary of the core.

In the circular case, our assumption of inhomogeneity in cross section but no z-dependence led to the characteristic that all the field components could be derived from the z-components of the propagating fields. The same is true in this case. For a propagating mode the z-fields must be periodic in z, and so our problem is to solve the wave equation for this system. In general, the wave equation for a field component in a dielectric medium is:

$$\nabla^2 f + \omega^2 \mu_o \epsilon f = 0 \qquad 4.2$$

In our case f = either E_z or H_z.

When expressed in elliptic cylinder co-ordinates, the wave equation becomes:

$$\frac{\delta^2 f}{\delta \xi^2} + \frac{\delta^2 f}{\delta \eta^2} + q^2 (k^2 - \beta^2) (\sinh^2 \xi + \sin^2 \eta) f = 0 \qquad 4.3$$

Here k has been written for $\omega^2 \mu_o \epsilon$ and β is the axial propagation constant of the mode.

(ii) Solution of the wave equation

We can express the variation of f in the cross section by the product of functions of ξ only and of η only:

$$f(\xi, \eta) = F(\xi)\, G(\eta) \qquad 4.4$$

This leads to the equations:

$$\frac{\delta^2 G}{\delta \eta^2} + (C - 2\gamma^2 \cos 2\eta)\, G = 0 \qquad 4.5$$

$$\frac{\delta^2 F}{\delta \xi^2} - (C - 2\gamma^2 \cosh 2\xi)\, F = 0 \qquad 4.6$$

Equation 4.5 is Mathieu's equation and 4.6 is the modified Mathieu equation[10]. Here, C is the separation constant and $\gamma^2 = 1/4(k^2 - \beta^2)q^2$. In our case f must be periodic in η with period π or 2π. For a lossless medium, γ^2 will be real. C is the characteristic number[1] of one particular Mathieu function which is a periodic solution of the equation and C is itself a function of γ^2. The Mathieu function may be even or odd in η.

When γ^2 is positive and real, the periodic solutions of Mathieu's equation 4.5 are:

$$G_1(\eta) = \begin{cases} ce_n(\eta, \gamma^2) & \text{even} \\ se_n(\eta, \gamma^2) & \text{odd} \end{cases} \qquad 4.7$$

ce is the cosine-elliptic function and se the sine-elliptic function[10]. (The subscript n specifies the order of the function).

Solutions of the modified Mathieu equation 4.6 when γ^2 is positive real are:

$$F_1(\xi) = \begin{cases} A\ Ce_n(\xi, \gamma^2) + B\ Fey_n(\xi, \gamma^2) & \text{even} \\ A_1\ Se_n(\xi, \gamma^2) + B_1\ Gey_n(\xi, \gamma^2) & \text{odd} \end{cases} \qquad 4.8$$

Ce and Se are quasi-periodic functions of ξ playing an analogous role in elliptical geometry to the J Bessel functions of circular geometry and the Fey and Gey are analogous to the Y Bessel functions. For negative real values of γ^2 the solutions of the Mathieu equation 4.5 are:

$$G_2(\eta) = \begin{matrix} ce^*_n(\eta, |\gamma^2|) & \text{even} \\ se^*_n(\eta, |\gamma^2|) & \text{odd} \end{matrix} \qquad 4.9$$

Similarly, the solutions for the modified Mathieu equation 4.6 in this case are:

$$F_2(\xi) = \begin{cases} D\ Ce^*_n(\xi, |\gamma^2|) + L\ Fek_n(\xi, |\gamma^2|) & \text{(even)} \\ D_1 Se^*_n(\xi, |\gamma^2|) + L_1 Gek_n(\xi, |\gamma^2|) & \text{(odd)} \end{cases} \qquad 4.10$$

A, A_1, B, B_1, C, C_1, D and D_1 are all arbitrary constants.

In analogous fashion to the solution for circular guides, we construct our solution by choosing functions which are physically reasonable. We do not use the Fey and Gey functions since they would imply an infinite field at $\xi = 0$. Ce* and Se* are also discarded since they become infinite at $\xi = \infty$ and so cannot represent a guided mode.

We can thus write the solution for the fields in the core, where γ^2 is positive and $0 \leqslant \xi \leqslant \xi_o$. These are of the form:

$$f_1 = \sum_{n=0}^{\infty} A_n \, Ce_n(\xi, \gamma_1^2) \, ce_n(\eta, \gamma_1^2) e^{j\beta z} \quad \text{(even)}$$

$$+ \sum_{n=1}^{\infty} A_n' \, Se_n(\xi, \gamma_1^2) \, se_n(\eta, \gamma_1^2) \, e^{j\beta z} \quad \text{(odd)} \qquad 4.11$$

Outside the core, where γ^2 is negative and $\xi \geqslant \xi_o$ the solutions have the form

$$f_2 = \sum_{n=0}^{\infty} L_n \, Fek_n(\xi, |\gamma_2^2|) \, ce^*_n(\eta, |\gamma_2^2|) \, e^{j\beta z} \quad \text{(even)}$$

$$+ \sum_{n=1}^{\infty} L_n' \, Gek_n(\xi, |\gamma_2^2|) \, se^*_n(\eta, |\gamma_2^2|) \, e^{j\beta z} \quad \text{(odd)} \qquad 4.12$$

In these equations, the A and L are arbitrary constants, while Fek and Gek represent radial Mathieu functions which play a similar role in elliptical geometry to the Hankel functions of cylindrical geometry. These equations apply for both the E and H fields present in the guide.

(iii) Applying boundary conditions

We now wish to produce the eigenvalue equation for the system by applying the boundary conditions. We retain flexibility in the choice of refractive index difference between the core and cladding materials. This procedure will lead to characteristic equations for the waveguide modes.

The boundary conditions relate to the components of E and H on both sides of and directed tangentially to the core boundary i.e. along the z and the η directions. These must be continuous across the core boundary. Thus we require:

$$E_{z1} = E_{z2} \qquad H_{z1} = H_{z2}$$

$$E_{\eta 1} = E_{\eta 2} \qquad H_{\eta 1} = H_{\eta 2} \qquad 4.13$$

A propagating mode consists of an electric wave and a magnetic wave propagating together, one of these having even symmetry about $\eta = 0$ and the other odd symmetry.

We arbitrarily choose to call modes with longitudinal magnetic component of even symmetry as even modes, and those with odd magnetic symmetry, odd modes. Thus mode designations will be $_{e}XX_{\mu\nu}$ for the even modes and $_{o}XX_{\mu\nu}$ for the latter. Here XX stands for any particular mode type designation, μ specifies the order of the Mathieu functions concerned and ν the νth root of the characteristic equation. For the fundamental modes, we choose the mode type designation as HE in analogy to the circular case. Our solutions will of course degenerate into the HE_{11} mode of the circular guide as the ellipticity falls to zero.

(iv) Analysis for $_{e}He$ modes

From this point onwards, we shall make use of the fact that the particular Mathieu functions are unambiguously connected with either the core or the cladding. This allows us to write them in abbreviated form omitting the explicit dependence on γ which will now be implicit.

We can now write the general expressions for the axial fields of the $_{e}HE_{\mu\nu}$ modes as:

$$H_{z1} = \sum_{\mu=0}^{\infty} A_{\mu}\, Ce_{\mu}(\xi)\, ce_{\mu}(\eta)$$

$$E_{z1} = \sum_{\mu=1}^{\infty} B_{\mu}\, Se_{\mu}(\xi)\, se_{\mu}(\eta) \qquad (0 \leq \xi \leq \xi_{o})$$

in the core and:

$$H_{z2} = \sum_{r=0}^{\infty} L_{r}\, Fek_{r}(\xi)\, ce^{*}_{r}(\eta)$$

$$E_{z2} = \sum_{r=1}^{\infty} P_{r}\, Gek_{r}(\xi)\, se^{*}_{r}(\eta) \qquad (\xi_{o} < \xi < \infty) \qquad 4.14$$

in the cladding.

Here we have introduced new co-efficients A_{μ}, B_{μ}, L_{r} and P_{r} These are specific to this case and should not be confused with the earlier notation.

Applying the boundary conditions $E_{z1} = E_{z2}$ from 4.14 we obtain:

$$\sum_{\mu=1}^{\infty} B_\mu \; Se_\mu (\xi_o) \; se_\mu (\eta) = \sum_{r=1}^{\infty} P_r \; Gek_r (\xi_o) \; se^*_r (\eta) \qquad 4.15$$

We now multiply both sides of this equation by $se_\nu(\eta)$ and integrate with respect to η from 0 to 2π. Then:

$$N_{\mu\nu} \; B_\mu \; Se_\mu (\xi_o) = \sum_{r=1}^{\infty}{}' P_r \; Gek_r (\xi_o) \; \gamma_{r\nu} \qquad 4.16$$

where $\nu = 0, 1, 2 \ldots .$
and the prime on the summation sign indicates that only odd or even values of r should be chosen according to whether ν is odd or even.

Here $N_{\mu\nu} = \int_0^{2\pi} se_\mu^{\,2} (\eta) \, d\eta \quad$ for $\mu = \nu$

$= 0 \qquad\qquad\qquad\qquad\quad \mu \neq \nu$

(This is due to the orthogonality of Mathieu functions.)

and $\gamma_{r\nu} = \int_0^{2\pi} se^*_r (\eta) \; se_\nu (\eta) \, d\eta$

For every μ there is an infinite set of linear equations which can be combined to give an equation with only two arbitrary constants B_μ and P_μ:

$$N_{\mu\mu} \; B_\mu \; Se_\mu (\xi_o) = \frac{P_\mu \; Gek_\mu (\xi_o)}{H_\mu (\gamma_{r\nu})} \qquad 4.17$$

where $H_\mu (\gamma_{r,\nu})$ is a function of $\gamma_{r\nu}$.

As an illustration, for $\mu = 1$ in equation 4.16:

$$N_{11}\ B_1\ Se_1\ (\xi_o) =$$

$$P_1\ Gek_1\ (\xi_o)\ \gamma_{11} + P_3\ Gek_3\ (\xi_o)\ \gamma_{31} + P_5\ Gek_5\ (\xi_o)\ \gamma_{51} + \ldots\ldots$$

$$0 = P_1\ Gek_1\ (\xi_o)\ \gamma_{13} + P_3\ Gek_3\ (\xi_o)\ \gamma_{33} + P_5\ Gek_5\ (\xi_o)\ \gamma_{53} + \ldots\ldots$$

$$0 = P_1\ Gek_1\ (\xi_o)\ \gamma_{15} + P_3\ Gek_3\ (\xi_o)\ \gamma_{35} + P_5\ Gek_5\ (\xi_o)\ \gamma_{55} + \ldots\ldots$$

etc. 4.18

Combining this set of equations, we obtain:

$$N_{11}\ B_1\ Se_1\ (\xi_o) = \frac{P_1\ Gek_1\ (\xi_o)}{H_1\ (\gamma_{r\nu})} \qquad 4.19$$

where $H_1\ (\gamma_{r\nu}) =$

$$\frac{\begin{vmatrix} \gamma_{33} & \gamma_{53} & \cdots\cdots \\ \gamma_{35} & \gamma_{55} & \cdots\cdots \\ \cdot & \cdot & \cdots\cdots \\ \cdot & \cdot & \cdots\cdots \end{vmatrix}}{\begin{vmatrix} \gamma_{11} & \gamma_{31} & \gamma_{51} & \ldots \\ \gamma_{13} & \gamma_{33} & \gamma_{53} & \ldots \\ \gamma_{15} & \gamma_{35} & \gamma_{55} & \ldots \\ & & & \end{vmatrix}}$$

It can be shown[11] that $P_1 > P_3 > P_5 > \ldots\ldots > P_\infty$

Having paused to examine in detail the results of matching the E_z boundary condition, we will now summarize the results of matching all four boundary conditions listed in 4.13. First we define some simplifying notation and expansions which can be readily shown from the theory of Mathieu functions:

$$ce^*_r\ (\eta) = \sum_{\nu=0}^{\infty}{}'\ \alpha_{r\nu}\ ce_\nu\ (\eta)$$

$$se^*_r\ (\eta) = \sum_{\nu=1}^{\infty}{}'\ \beta_{r\nu}\ se_\nu\ (\eta)$$

$$\frac{d}{d\eta}\left(ce_\mu(\eta)\right) = \sum_{\nu=1}^{\infty}{}' \chi_{\mu\nu}\, se_\nu(\eta)$$

$$\frac{d}{d\eta}\left(se_\mu(\eta)\right) = \sum_{\nu=0}^{\infty}{}' \rho_{\mu\nu}\, ce_\nu(\eta) \qquad 4.20$$

where

$$\alpha_{r\nu} = \int_0^{2\pi} ce_r^*(\eta)\, ce_\nu(\eta)\, d\eta \Big/ \int_0^{2\pi} ce_\nu^2(\eta)\, d\eta$$

$$\beta_{r\nu} = \frac{\gamma_{r\nu}}{N_{\mu\nu}}$$

$$\chi_{\mu\nu} = \int_0^{2\pi} ce_\mu'(\eta)\, se_\nu(\eta)\, d\eta \Big/ \int_0^{2\pi} se_\nu^2(\eta)\, d\eta$$

$$\rho_{\mu\nu} = \int_0^{2\pi} se_\mu'(\eta)\, ce_\nu(\eta)\, d\eta \Big/ \int_0^{2\pi} ce_\nu^2(\eta)\, d\eta$$

Conditions for matching the fields at the boundary can then be expressed by equation 4.16 and also:

$$A_\mu\, Ce_\mu(\xi_o) = \sum_{r=0}^{\infty}{}' L_r\, Fek_r(\xi_o)\, \alpha_{r\nu}$$

$$\frac{\omega\varepsilon_1}{\beta} B_\nu\, Se_\nu'(\xi_o) + \left(1 + \frac{\gamma_1^2}{\gamma_2^2}\right) \sum_{r=1}^{\infty}{}' A_r\, Ce_r(\xi_o)\, \chi_{r\nu} = \left(-\frac{\gamma_1^2}{\gamma_2^2}\right) \frac{\omega\varepsilon_o}{\beta} \sum_{r=1}^{\infty}{}' P_r\, Gek_r'(\xi_o)\, \beta_{r\nu}$$

$$\frac{\omega\mu_o}{\beta} A_\nu\, Ce_\nu'(\xi_o) - \left(1 + \frac{\gamma_1^2}{\gamma_2^2}\right) \sum_{r=0}^{\infty}{}' B_r\, Se_r(\xi_o)\, \rho_{r\nu} = \left(-\frac{\gamma_1^2}{\gamma_2^2}\right) \frac{\omega\mu_o}{\beta} \sum_{r=0}^{\infty}{}' L_r\, Fek_\nu'(\xi_o)\, \alpha_{r\nu} \qquad 4.21$$

where the dashed functions indicate those differentiated with respect to the argument and β is the propagation constant of the mode under consideration.

Combining equations 4.16 and 4.21 and defining:

$$g_{\mu\nu} = \left(1 + \frac{\gamma_1^2}{\gamma_2^2}\right) Fek_\mu(\xi_o) \sum_{r=1}^{\infty}{}' \chi_{r\nu}\, \alpha_{\mu r}$$

$$s_{\mu\nu} = -\left(1 + \frac{\gamma_1^2}{\gamma_2^2}\right) Gek_\mu(\xi_o) \sum_{r=1}^{\infty}{}' \rho_{r\nu}\, \beta_{\mu r}$$

$$h_{\mu\nu} = \frac{\omega\varepsilon_1}{\beta} \frac{Se'_\nu(\xi_o)}{Se_\nu(\xi_o)} + \frac{\gamma_1^2}{\gamma_2^2} \frac{\omega\varepsilon_2}{\beta} Gek'_\mu(\xi_o)\, \beta_{\mu\nu}$$

$$t_{\mu\nu} = \frac{\omega\mu}{\beta} \frac{Ce'_\nu(\xi_o)}{Ce_\nu(\xi_o)} Fek_\mu(\xi_o)\, \alpha_{\mu\nu} + \frac{\gamma_1^2}{\gamma_2^2} \frac{\omega\mu_o}{\beta} Fek'_\mu(\xi_o)\, \alpha_{\mu\nu}$$

we obtain:

$$\sum_{\mu=0}^{\infty}{}' \left[L_\mu\, g_{\mu\nu} + P_\mu\, h_{\mu\nu}\right] = 0$$

$$\sum_{\mu=0}^{\infty}{}' \left[L_\mu\, t_{\mu\nu} + P_\mu\, s_{\mu\nu}\right] = 0 \quad (\nu = 0, 2, 4 \ldots \text{ or } 1, 3, 5)$$

4.22

Equations 4.22 are two sets of infinite homogeneous linear algebraic equations in L_μ and P_μ. For non-trivial solutions of this set of equations, the determinant formed by the coefficients must vanish:

$$\begin{vmatrix} g_{11} & h_{11} & g_{31} & h_{31} & g_{51} & h_{51} & \cdots \\ t_{11} & s_{11} & t_{31} & s_{31} & t_{51} & s_{51} & \cdots \\ g_{13} & h_{13} & g_{33} & h_{33} & g_{53} & h_{53} & \cdots \\ t_{13} & s_{13} & t_{33} & s_{33} & t_{53} & s_{53} & \cdots \\ g_{15} & h_{15} & g_{35} & h_{35} & g_{55} & h_{55} & \cdots \\ t_{15} & s_{15} & t_{35} & s_{35} & t_{55} & s_{55} & \cdots \\ \cdot & \cdot & \cdot & \cdot & \cdot & & \\ \cdot & \cdot & \cdot & \cdot & \cdot & & \end{vmatrix} = 0 \qquad 4.23$$

This applies for the ${}_eHE_{\mu\nu}$ modes. When the ellipticity approaches zero, all terms outside the dashed lines in 4.23 tend to zero and these equations yield the characteristic equations for the circular case. For the present case, however, it is difficult to evaluate the roots of this determinant due to its extreme complexity. Using the method of successive approximations[11] Yeh has shown[9] that the first root of the $\mu = 1$ set of modes - applying to ${}_eHE_{11}$ - is governed principally by:

$$\begin{vmatrix} g_{11} & h_{11} \\ t_{11} & s_{11} \end{vmatrix} = 0 \qquad 4.24$$

provided that the core ellipse is not too flat (i.e. $\xi > 0.5$). For other modes ${}_{e}HE_{\mu\nu}$, successive approximations should start from the 2 x 2 determinant formed by the elements with the subscripts $\mu\nu$.

(v) Computation of the propagation constants

The object of finding the propagation constants of the orthogonally polarised fundamental modes was to find the magnitude of the difference between them over useful ranges of ellipticity and operating frequency for a given core size and index difference. In order to do this we perform a similar analysis for the ${}_{o}HE_{\mu\nu}$ modes to that described above. The odd modes have fields of similar form to the even modes, but with the symmetric and anti-symmetric Mathieu functions exchanging places in the field descriptions corresponding to 4.14 (the even case). The analysis finally produces a determinant:

$$\begin{vmatrix} g_{11}^* & h_{11}^* & g_{31}^* & h_{31}^* & \cdots \\ t_{11}^* & s_{11}^* & t_{31}^* & s_{31}^* & \cdots \\ g_{13}^* & h_{13}^* & g_{33}^* & h_{33}^* & \cdots \\ t_{13}^* & s_{13}^* & t_{33}^* & s_{33}^* & \cdots \\ \cdot & \cdot & \cdot & \cdot & \\ \cdot & \cdot & \cdot & \cdot & \end{vmatrix} = 0 \qquad 4.25$$

where $g_{\mu\nu}^*$ etc. are the same as the $g_{\mu\nu}$ etc with

$\mathrm{Fek}_{\mu}(\xi_o)$ interchanged with $\mathrm{Gek}_{\mu}(\xi_o)$
$\mathrm{Fek}_{\mu}(\xi_o)$ " " $\mathrm{Gek}_{\mu}(\xi_o)$
$\alpha_{\mu r}$ " " $\beta_{\mu r}$
$\chi_{r\nu}$ " " $\rho_{r\mu}$

This determinant simplifies in the same way as 4.23. In order to retain comparability with the circular guide, we now define the normalised frequency of an elliptically-cored fibre as:

$$V = \frac{2\pi b}{\lambda_o} \sqrt{n_1^2 - n_2^2} \qquad 4.26$$

where b is the semi-minor axis of the core ellipse. We also define U and W as for the circular guide using b in place of the radius of the circular fibre. Finally we define the normalised propagation constant:

$$\bar{\beta} = \beta / k_o \qquad 4.27$$

(where $k_o = 2\pi/\lambda_o$)

Then we find the fully expanded form of 4.24 as:

$$\left[\frac{n_1^2}{U^2} \frac{Se_\mu'(\xi_o)}{Se_\mu(\xi_o)} + \frac{n_2^2}{W^2} \frac{Gek_\mu'(\xi_o)}{Gek_\mu(\xi_o)} \right] \left[\frac{1}{U^2} \frac{Ce_\mu'(\xi_o)}{Ce_\mu(\xi_o)} + \frac{1}{W^2} \frac{Fek_\mu'(\xi_o)}{Fek_\mu(\xi_o)} \right] = \mu^2 \bar{\beta}^2 \left[\frac{1}{W^2} + \frac{1}{U^2} \right]^2 \qquad 4.28$$

for the even modes and

$$\left[\frac{1}{U^2} \frac{Se_\mu'(\xi_o)}{Se_\mu(\xi_o)} + \frac{1}{W^2} \frac{Gek_\mu'(\xi_o)}{Gek_\mu(\xi_o)} \right] \left[\frac{n_1^2}{U^2} \frac{Ce_\mu'(\xi_o)}{Ce_\mu(\xi_o)} + \frac{n_2^2}{W^2} \frac{Fek_\mu'(\xi_o)}{Fek_\mu(\xi_o)} \right] = \mu^2 \bar{\beta}^2 \left[\frac{1}{W^2} + \frac{1}{U^2} \right]^2 \qquad 4.29$$

for the odd modes.

The propagation constants for the odd and even modes were calculated from the above equations and the difference was plotted as a function of V for various ellipticities. It was found during this work that for a given ellipticity and V-value, the difference between the normalised propagation constants, $\Delta\bar{\beta}$, was directly proportional to Δn^2, just as predicted by the perturbation analysis described in section 3.3.3. Deviation from this

relationship was less than 2% for $10^{-3} < \Delta n < 7 \times 10^{-2}$. The algorithms and details of the computations are presented together with the final computer program in Appendix II. The results of the computations are plotted in figure 4.1 with the vertical axis normalised to produce a universal set of curves for all index differences. These curves were originally published in reference 12. Note that:

$$\overline{\Delta\beta} = \frac{\Delta\beta}{k_o} \qquad 4.30$$

The calculations show that the even wave, ie. that polarised along the minor axis of the core ellipse, travels faster than the odd wave, indicating that a greater proportion of the power is confined to the core for the odd wave. The position of the peak in $\overline{\Delta\beta}$ shifts towards smaller V values as ellipticity increases and the curves move smoothly towards the slab guide case also. Sixty percent of this maximum possible $\Delta\beta$ is already gained when the a/b ratio is 2.5:1 (a is the semi-major axis of the core ellipse). Thereafter ellipticities must be greatly increased to secure appreciable gains in $\Delta\beta$.

4.2.2 Higher mode cut-off in elliptical dielectric waveguides

So far, we have tacitly assumed that the elliptically cored fibre can be operated in the single mode region. Yeh showed[9] that the odd and even HE_{11} modes are both 'fundamental' modes, ie. they have no cut-off, but did not consider the cut-off conditions for higher order modes. A first attempt to analyse the cut-off conditions for higher order modes was made by Cozens and Dyott[13], but no experimental confirmation has been published and several authors have disputed the validity of these calculations (e.g. ref 17). Essentially the method of reference 13 was to assume that the elliptical guide behaves in a similar fashion to the circular guide and solve for the cut-off of modes in the elliptical guide with $\mu = 0$. This led to the characteristic equations for ${}_eTE_o$ modes and ${}_oTM_o$ modes respectively:

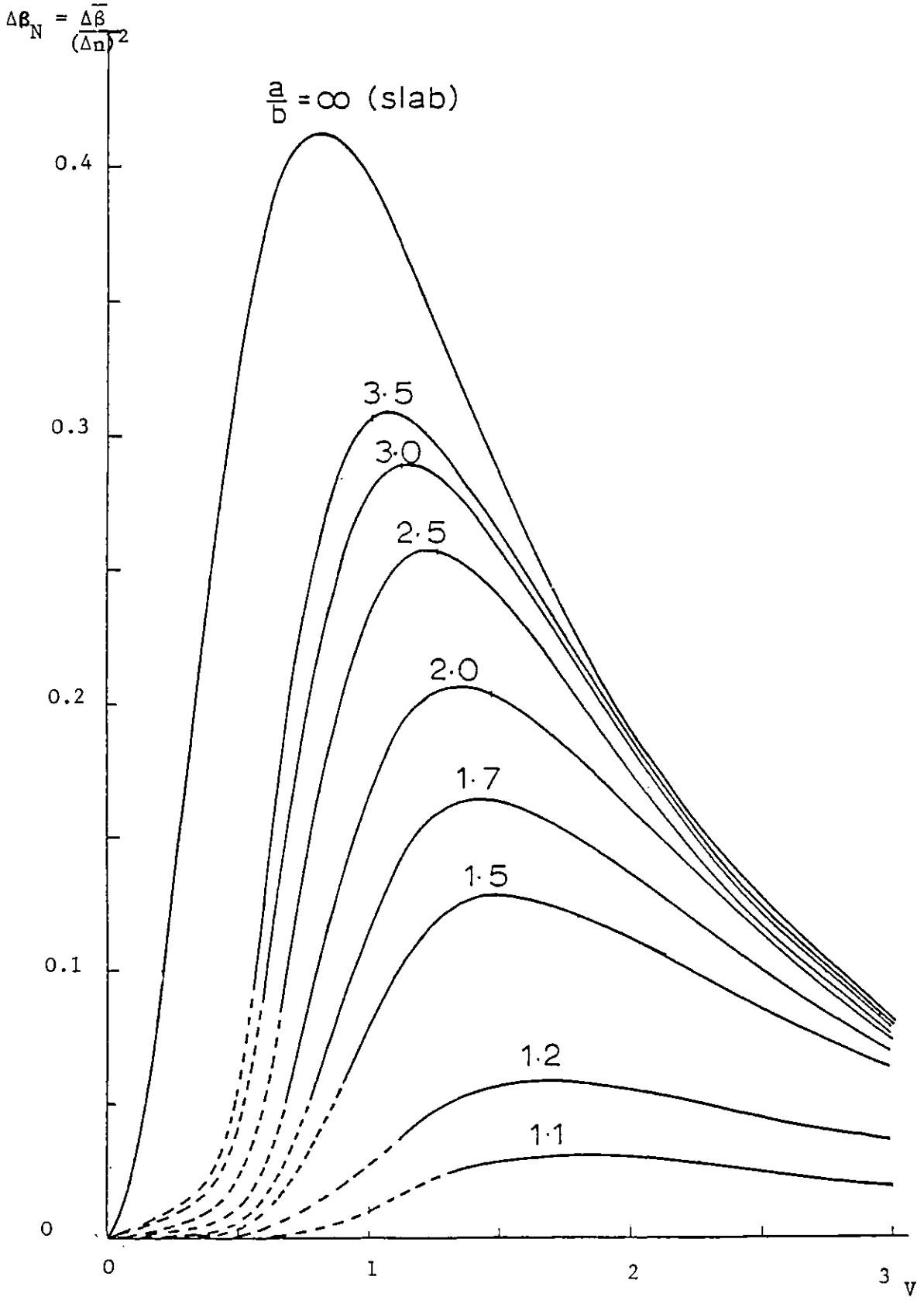

Fig. 4.1 Normalised difference in propagation constant against V for various ellipticities

$$\left(\frac{W^2}{U} \frac{Ce'_o}{Ce_o} + \frac{W\, Fek'_o}{Fek_o} \right) = 0$$

$$\left[\left(\frac{\varepsilon_1}{\varepsilon_2} \right) \frac{W^2}{U} \frac{Ce'_o}{Ce_o} + \frac{W\, Fek'_o}{Fek_o} \right] = 0 \qquad 4.31$$

This produces the requirement that $Ce_o \to 0$ at cut-off for both modes. This would lead to the cut-off behaviour shown in figure 4.2, with the cut-off moving to lower frequency as the ellipticity is increased. The cut-off frequency is not polarisation dependent for the small differences in refractive index between core and cladding which can be expected in the optical case. Experimental evidence[14] tends to support this argument between $0.4 \lesssim b/a < 1$, but for $0 < b/a < 0.4$, higher modes appear at lower V than predicted by this theory. It is conjectured[14] that this is due to the $_eHE_{21}$ mode strongly coupling to the fundamental $_eHE_{11}$ mode at high ellipticities.

The present author observed relevant behaviour in this respect while working on the verification of the $\Delta\beta$ calculations using solid core fibre. A fibre with a/b = 2.54 (measured in preform) working at a nominal V value of 1.78 was found to be multimode despite having a predicted V for higher mode cut-off of 1.82. This fibre is discussed more fully in the next section, where it is made clear that fibre non-uniformity might account for this discrepancy. However, a very clear two lobe radiation pattern was observed with this fibre. This is shown in the photograph (fig. 4.3) below.

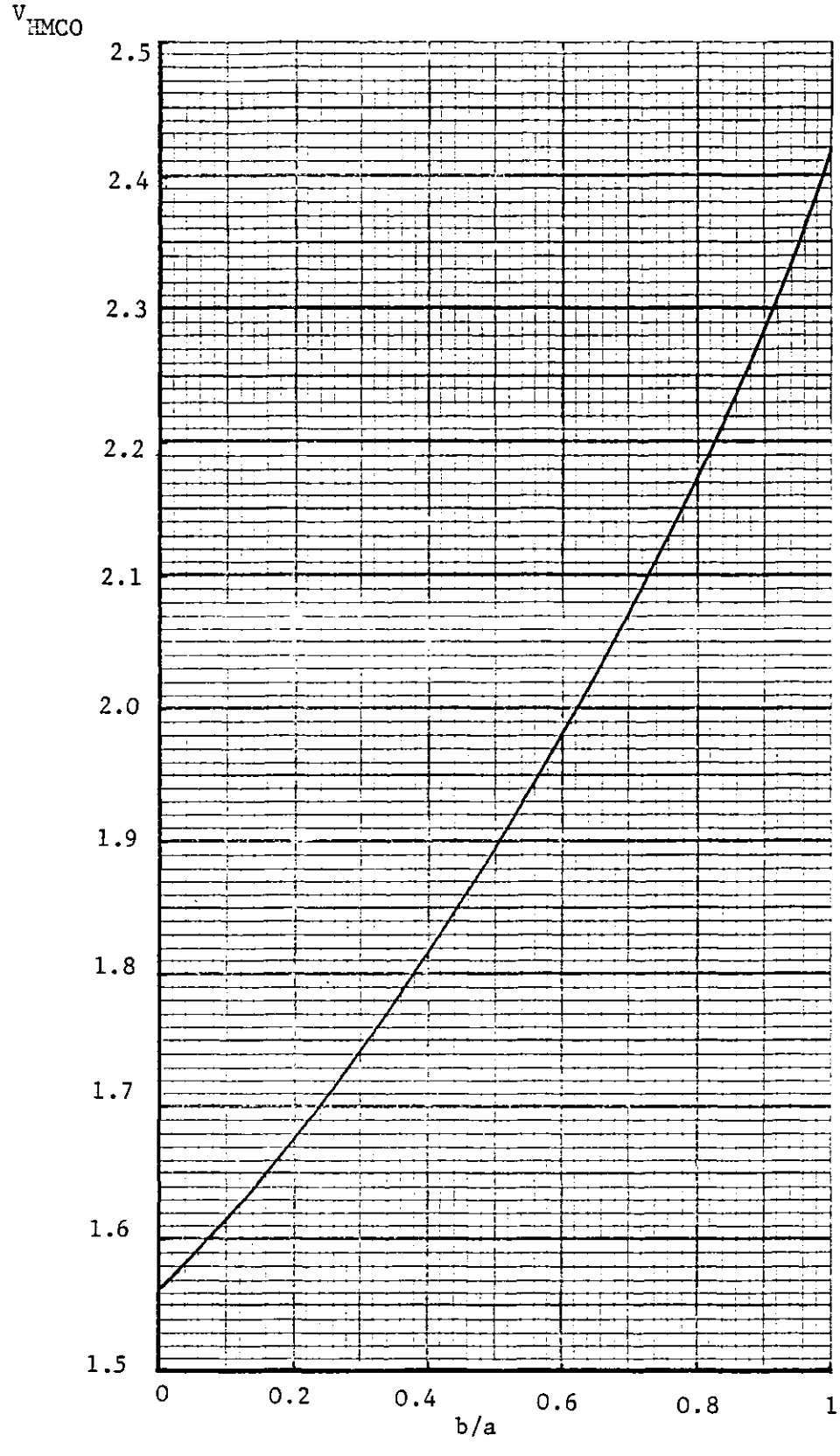

Fig. 4.2 Predicted cut-off behaviour for elliptically cored guide

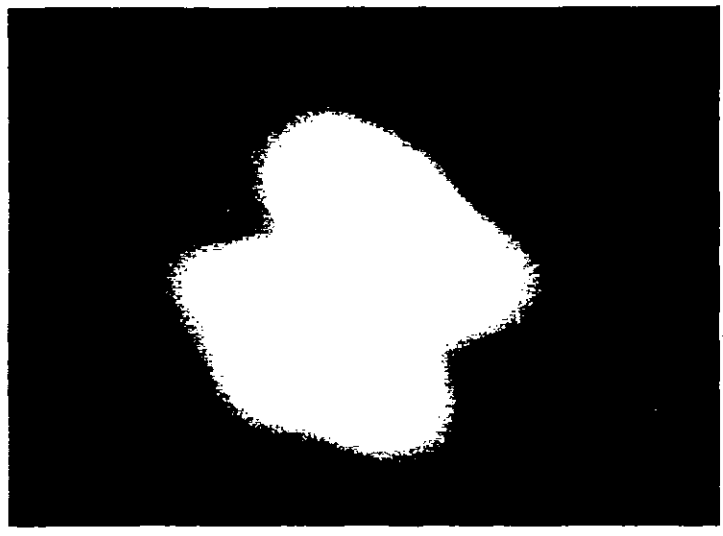

Fig. 4.3 Radiation pattern of first higher order mode of elliptically cored fibre

4.3 Qualitative tests on solid core fibre

4.3.1 Required $\Delta\beta$ values

In section 4.1, it was argued that a birefringence sufficient to suppress polarisation coupling should be adequate if it produces a relative delay of one cycle or more for every millimetre of travel along the fibre.

In order to simplify the design of elliptically-cored fibres with respect to this requirement, the information on peak $\Delta\beta_N$ from figure 4.1 has been transformed into a normalised minimum pitch (or beat length) and re-plotted as a function of ellipticity. (See figure 4.4) Interestingly, this shows that the minimum beat length for a given index difference and operating wavelength is inversely proportional to the core ellipticity. This is an empirical result only, but is obviously very useful.

Examination of figure 4.4 shows that this beat length requirement fixes the refractive index difference at very high levels compared to conventional telecommunications fibre. It was realised that fibres with the maximum possible index difference should be made.

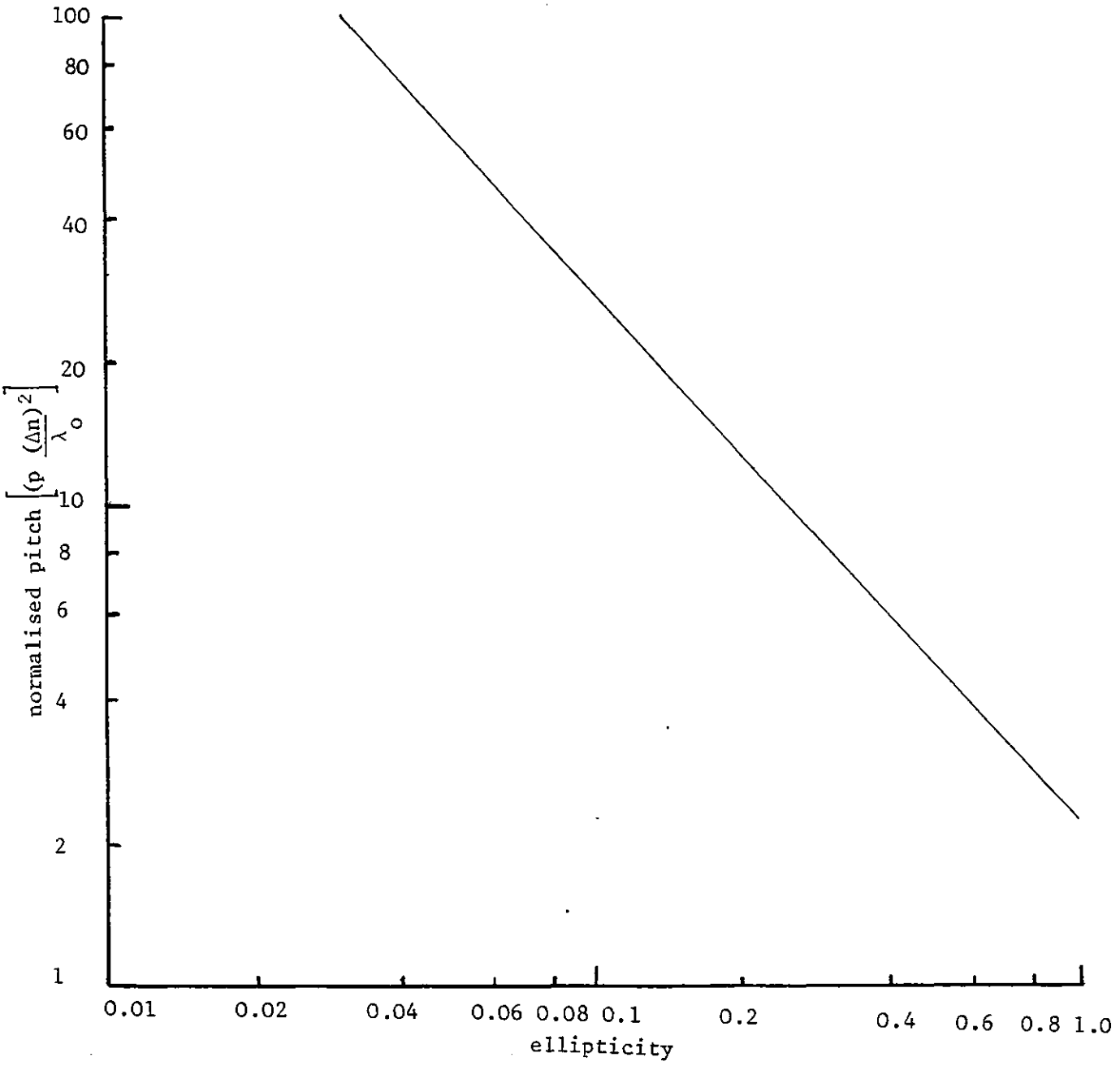

Fig. 4.4 Graph of minimum normalised pitch v. ellipticity for elliptical core fibre

Using presently available materials, the largest index difference possible is about 0.07, assuming a pure germania core and silica cladding. During the course of the work described in this thesis, a few samples of such fibre were made available for evaluation by R. Dyott. These were made within the Department as part of a research effort on the production of commercially usable elliptical fibres.

4.3.2 Measurement of $\Delta\beta$

It was decided to investigate the possibility of using some of these fibre samples for checking the $\Delta\beta$ calculations. The length required for one cycle of relative phase delay to occur between the two polarised modes has already been referred to as the "beat length", symbol p, and is visible under the right conditions due to the directional nature of Rayleigh scattering from a fibre core. Each Rayleigh scattering centre acts as a miniature dipole, radiating maximum light at right angles to the polarisation of the incident wave and minimum light in a direction parallel to the polarisation direction of the incident light. In the case where circularly polarised light is launched into a fibre having a fixed birefringence, the light will split up so that equal power travels in the two polarised modes, and as the relative phase of these two modes slips, so the state of polarisation evolves along the fibre length. This evolution is shown in figure 4.5. The extreme states of polarisation are linear and at ± 45° to the birefringent axes of the fibre. When the fibre is viewed transversely in one of these directions, it is possible to see a periodic variation in the scattered light having a pitch, p, equal to the beat length. This yields $\Delta\beta_N$ immediately:

$$\Delta\beta_N = \frac{\Delta\overline{\beta}}{(\Delta n)^2} = \frac{\lambda_o}{p(\Delta n)^2} \qquad 4.32$$

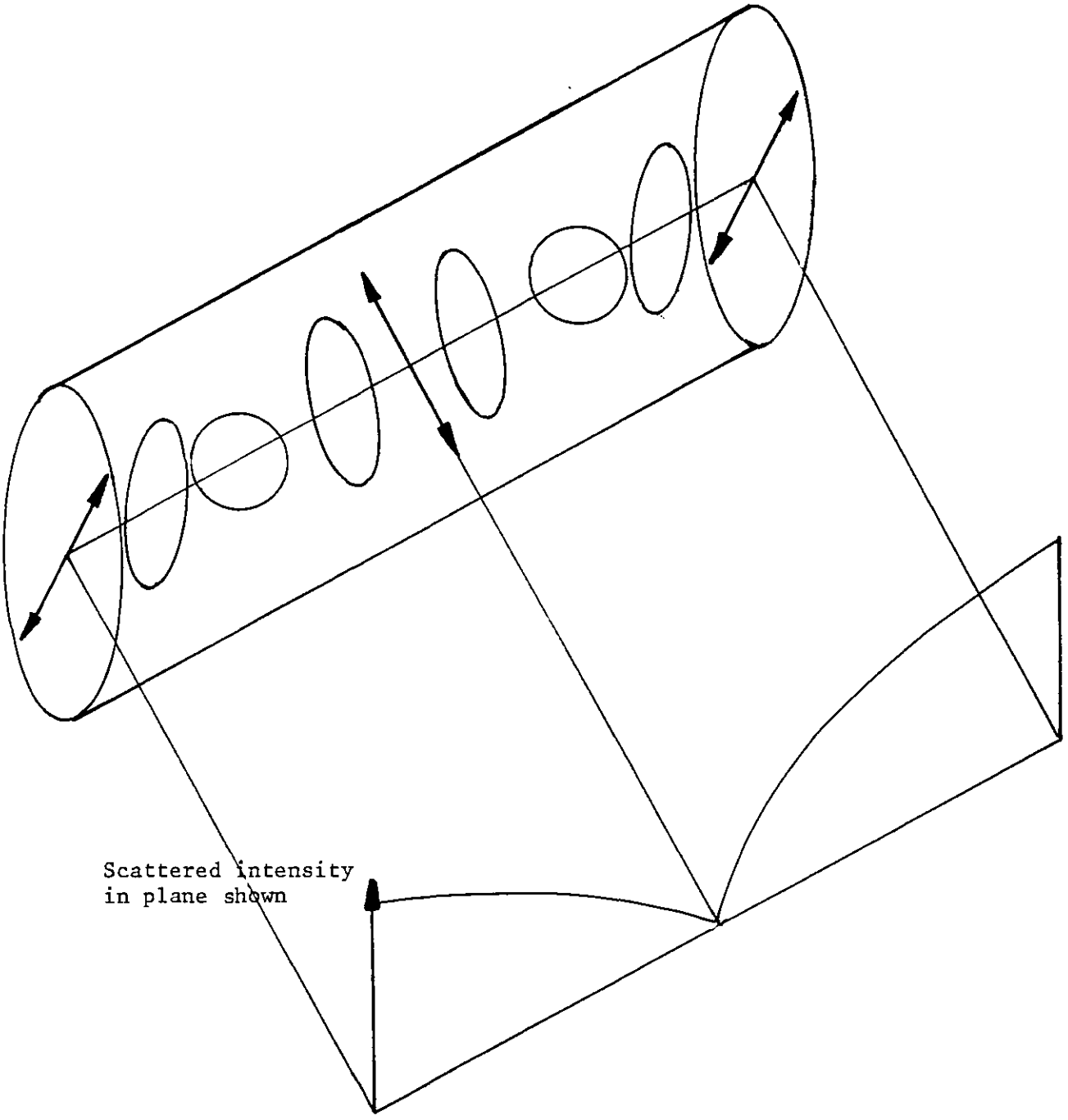

Fig. 4.5 Variation of scattered light intensity with change of polarisation

Experiments were carried out using the equipment described in section 3.1.4, but with the quarter-wave plate now interposed between the laser polariser and launcher so as to produce circular polarisation (see fig. 3.8). The wooden beam was painted matt black for this experiment and the fibre was viewed transversely by means of a macrophotography system so as to be able to see a magnified view of the fibre and record the results on film.

The camera position was fully adjustable to allow for changes in the orientations of the privileged axes of the fibre. It was found that a good beat pattern was only obtained when the fibre was immersed in index matching liquid which eliminated multiple scattering from fibre surface defects. Without this liquid, it was impossible to see any beat pattern. As it was necessary to move the camera for different fibres, a picture of a metal rule in the fibre position was made each time a beat pattern was recorded so that the real scale would be known. A photograph of the equipment is shown in figure 4.6.

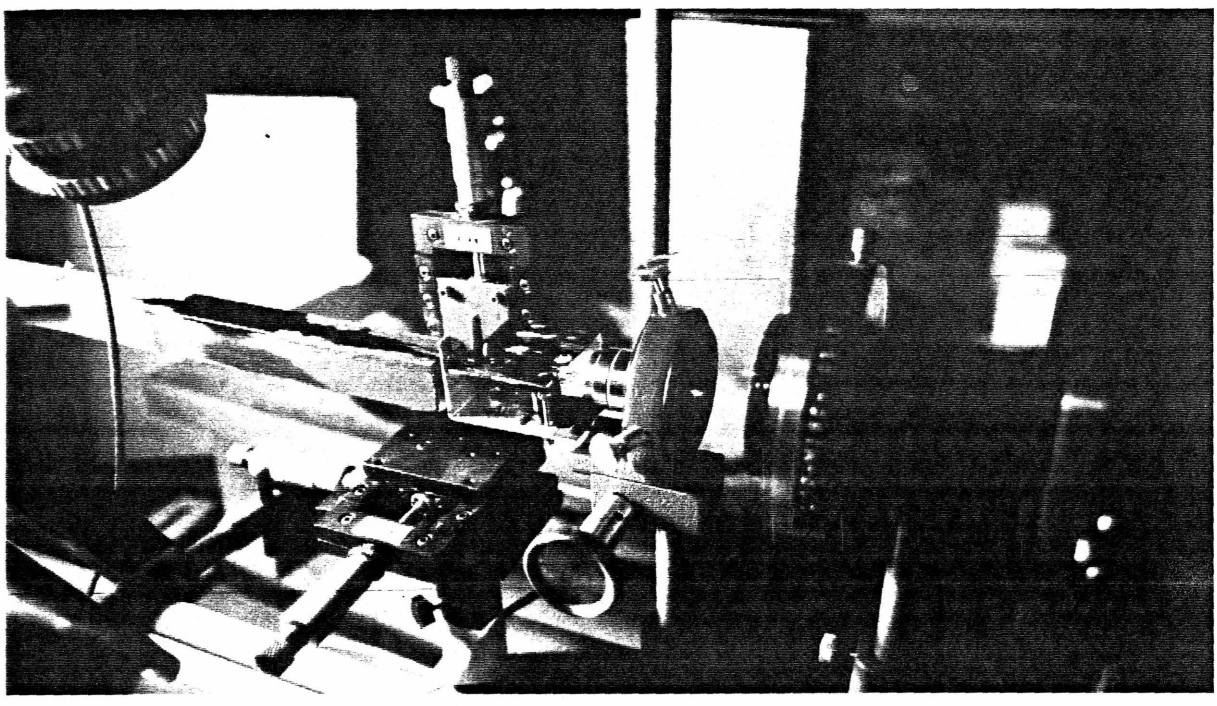

Fig. 4.6 Apparatus for producing and recording beat patterns

Tests were made on several fibres pulled from the same preform. The preform data was:

Preform reference:	790514
Measured numerical aperture:	$\sqrt{(n_1^2 - n_2^2)} = 0.424$
	$\Delta n = 0.061$
Ellipticity:	$a/b = 2.54$
Outer diameter/core major axis =	5.15

Four samples of fibre were measured. The results are summarised below:

Fibre Outer Diameter (μm)	Beat length (mm)	Fibre Reference
15	1.53	790514/2
14.4	0.96	790514/3
17.5	1.20	790514/5
17.5	0.77	790514/8

Table 4.1 Results of beat length scattering experiment

The beat pattern photograph corresponding to the last result in the table is shown here as figure 4.7. This was originally published as part of reference 12.

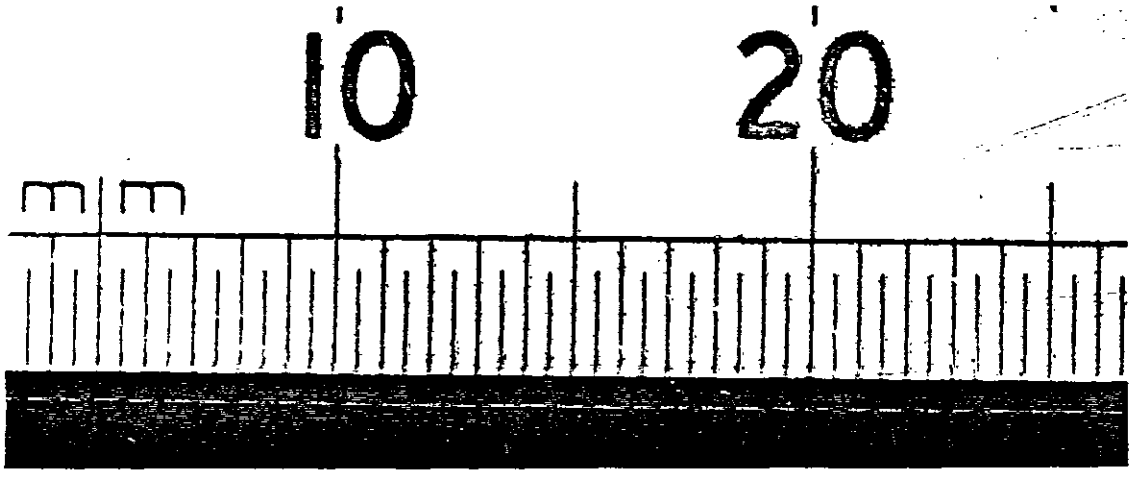

Fig. 4.7 Beat pattern for fibre 790514/8

The theoretically predicted beat length calculated from the preform and fibre data was about 0.85 mm. From these tests it was possible to infer that the $\Delta\beta$ calculations were producing the correct order of magnitude, but the variability made it impossible to gain any more precise information from these results. This can be attributed mainly to the variability in the quality of the fibre which had an obviously non-uniform core. In addition, special care had to be taken to avoid exciting higher order modes with these fibres. When higher order modes were present, beat lengths increased.

Recently workers in Japan have produced experimental samples of elliptically cored fibre using doped silica structures. The results of measurements of $\Delta\beta$ have been reported, but were expressed in a different way to that used here[16]. These results have been normalised according to our own method and are included here as figure 4.8 for comparison with the predictions of figure 4.1. It is interesting that the experimental curves appear to have the same shape and peak magnitude as the theoretical curves. However, all the curves are shifted to a higher V-value than that predicted. This might be explained by postulating that the dip in the refractive index profile

of the test fibres lowers the V value from that of a perfect step index profile with the same peak index. Stress effects may also play a significant part in modifying these results.

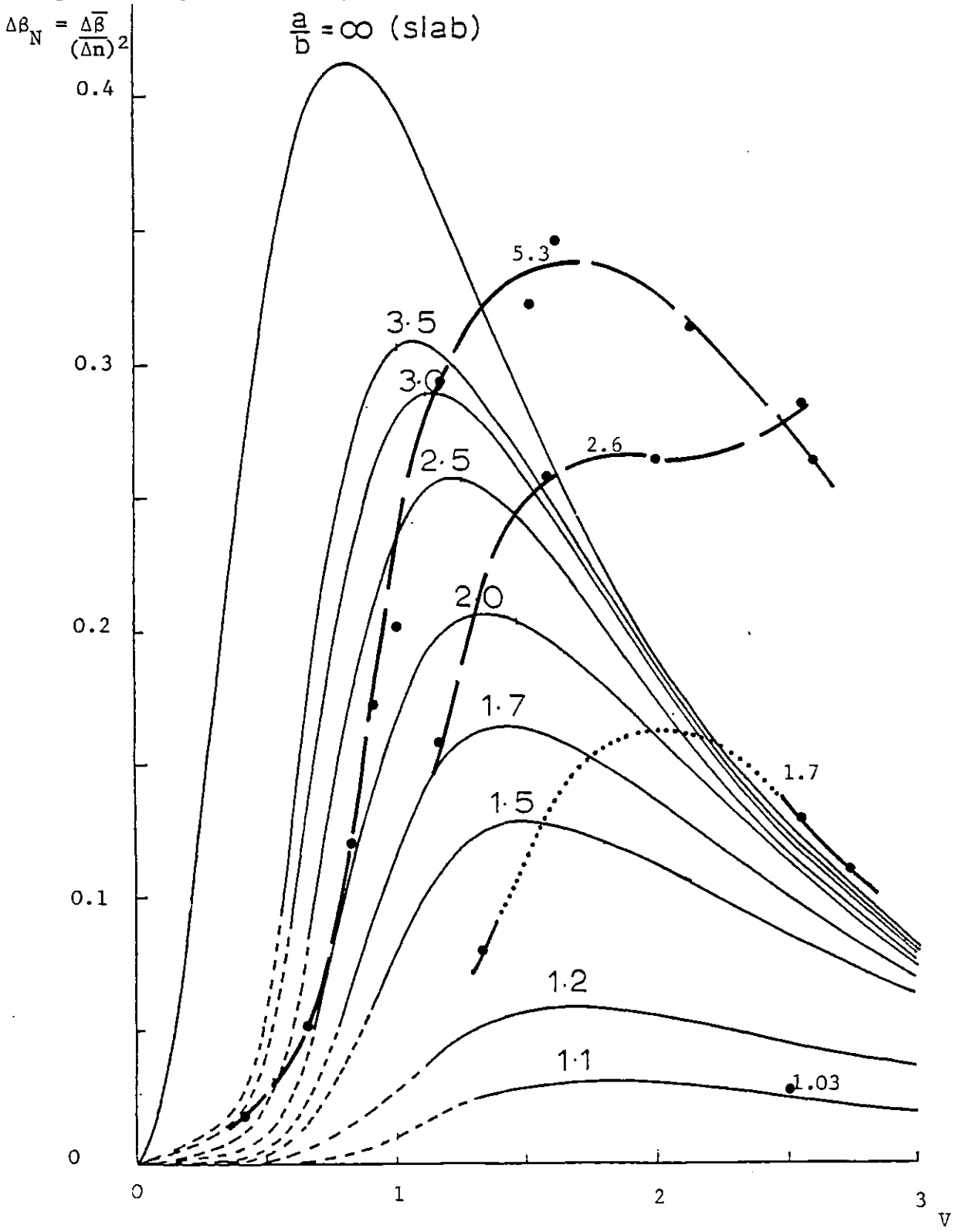

Fig. 4.8 Comparison of theoretical and experimental $\Delta\beta$ values

4.3.3 Polarisation and mode stability

Some attempts were made to examine the polarisation preserving characteristics of these fibres by bending, squashing and twisting them mechanically. When operated single mode, the fibre samples performed very well; lengths of fibre up to a metre showed no visible degradation of linear polarisation, even for bends of 2 mm diameter. It was found that even when coupling to higher modes was observed, this occurred preferentially to modes with the same polarisation. When any degradation of polarisation occurred, this was due to the higher mode coupling to its own orthogonal polarisation. Similar behaviour has since been observed by Stolen[15] in low moded, stressed fibres.

4.3.4 Radiation pattern

Finally, the radiation patterns from the ends of these fibres were photographed. A typical result is shown in figure 4.9 below. The shapes of the end patterns were not obviously sensitive to polarisation, indicating that the differences of power containment in the core between the polarised modes are indeed extremely small.

Fig. 4.9 Radiation pattern from an elliptically cored fibre

References to Chapter IV

1. AL-SHUKRI, S.
"The growth of opto-electric organic crystals in monomode optical fibres"
PhD. Thesis; Imperial College; London 1981

2. KAMINOW, I.
"Strain birefringence in single polarisation germano-silicate optical fibres"
Electronics Letters: 15:21 pp. 677-9 (11 Oct 79)

3. KATSUYAMA, T., MATSUMURA, H., SUGANUMA, T.
"Low loss single polarisation fibres"
Electronics Letters: 17:13 pp. 473-4 (25 June 81)

4. RASHLEIGH, S.
"Characterisation of polarisation holding in birefringent single mode fibres"
International Conference on Fibre Optic Rotation Sensors; Cambridge USA; (Nov 81)
Published by Research Laboratory of Electronics, MIT, Cambridge.

5. OKOSHI, T., OYAMADA, K.
"Single polarisation single mode optical fibrs with refractive index pits on both sides of core"
Electronics Letters: 16: 18 pp. 712-3 (28 Aug 80)

6. KITAYAMA, K., SEIKAI, S., UCHIDA, N., AKIYAMA, M.
"Polarisation maintaining single mode fibre with azimuthally inhomogeneous index profile"
Electronics Letters: 17:12 pp. 419-420 (11 June 80)

7. HOSAKA, T., OKAMOTO, K., MIYA, T., SASAKI, Y., EDAHIRO, T.
"Low loss single polarisation fibres with asymmetrical strain birefringence"
Electronics Letters: 17:15 pp. 530-1 (23 July 81)

8. LYUBIMOV, L. A., VESELOV, G. I., BEI, N. A.
"Dielectric waveguide with elliptical cross section"
Radio Engineering & Electronic Physics: Vol. 6 (1961)
pp 1668-1677

9. YEH, C. Y.
"Elliptical dielectric waveguides"
J. Appl. Phys. 33:11 (Nov 62) pp. 3235-43

10. MCLACHLAN, N. W.
"Theory and application of Mathieu Functions"
Oxford; Clarendon Press; 1947

11. KANTOROVICH, L., KRYLOV, V.
"Approximate methods of higher analysis"
Interscience; New York, 1958

12. DYOTT, R. B., COZENS, J. R., MORRIS, D. G.
"Preservation of polarisation in optical fibre waveguides with elliptical cores"
Electronics Letters 15:13 pp. 380-2 (21 June 79)

13. COZENS, J. R., DYOTT, R. B.
"Higher mode cut-off in elliptical dielectric waveguides"
Electronics Letters 15:18 pp. 558-9 (30 August 79)

14. DYOTT, R. B.
"Elliptically cored polarisation preserving fibre"
International Conference on Fibre Optic Rotation Sensors and Related Technologies, Research Laboratory of Electronics, MIT, Cambridge, USA; (9-11 November 81)

15. STOLEN, R. H., WAGNER, R. E., PLEIBEL, W.
"Linear polarisation in birefringent multimode fibres"
IOOC 81, San Francisco, 1981

16. MATSUMURA, H., KATSUYAMA, T., SUGANUMA, T.
"Fundamental study of single polarisation fibres"
6th European Conference on Optical Communication, York, 1980

17. RENGARAJAN, S. R., LEWIS, J. E.
"First higher mode cut-off in two layer elliptical fibre waveguides"
Electronics Letters 16:7, (27 March 80), pp. 263-4

CHAPTER V

PRODUCTION OF GLASS TUBES WITH ELLIPTICAL MICRON-SCALE BORES

5.1 Liquid cored fibres for verifying $\Delta\beta$ calculations

In chapter four, some limited tests on beat lengths in solid core elliptical fibres were described and the results were compared with a theoretical calculation of the normalised difference in propagation constants for these fibres. Although these tests appeared to show partial agreement with theory, it was felt that the remaining discrepancy and opportunities for error in the calculations justified a more determined attempt to expose any inaccuracy in the calculations or the normalisation technique. Since the discrepancy between theory and practice in the results of chapter four appeared to be attributable to the non-ideal nature of doped silica fibres, it was decided to avoid the practical problems and possible spurious effects associated with such fibres and to produce stress free, truly step index, liquid core elliptical guides.

Initially this entailed production of short lengths of hollow fibre with an elliptical bore suitable for filling with liquid which would act as the core material. It was expected that the production of a bore of single mode dimensions would be achievable fairly quickly. There were also other obvious advantages to this technique. The ellipse dimensions were expected to be easily measurable directly since the boundary would be a well defined solid surface. The liquid core would eliminate refractive index perturbations due to stress since there would be no thermal stress involved and the cladding could itself be annealed prior to filling. Furthermore, the core index would be easily measurable by using a liquid sample in a standard refractometer. Thus conditions would be nearly ideal for comparing theory and practice.

This chapter describes the results of a sustained effort to master the technique necessary for the production and examination of hollow fibres for subsequent optical tests, which will be described in the following chapter. In practice, the realization of the technique

was replete with problems. These were largely connected with the rheology of the glass and required much effort for solution. However, once the correct conditions for fibre production had been established, the process became relatively routine. The production method described here is only suitable for short fibres and the main drawbacks of the technique are the lack of strength and only adequate uniformity of the final product. The great advantage of the technique is that it requires no sophisticated equipment and is consequently very cheap to operate.

5.2 Production technique for elliptical bore tubes

This section is intended to provide an outline of the short fibre production method described in this chapter.

For optical tests on the elliptical guide, only short lengths of fibre were required - of the order of a few centimetres. It was therefore decided to dispense with the usual mechanisms for feeding preform material into a drawing furnace and for reeling the fibre outfall, and to go instead for a simplified static arrangement. This used a hollow glass preform hung vertically through the centre of a short furnace by means of a screw clamp arrangement. Fibre was then drawn from the furnace hot zone by the force of the weight of material below the hot zone (this is known as drop-loading). Under these conditions, the preform develops a 'neck' in the hot zone itself which governs the instantaneous diameter of the thread leaving the hot zone and thereafter solidifying. The arrangement is shown schematically below.

It must be understood that this method is basically a departure from the standard methods of producing fibre. A basic assumption in all large scale fibre production, irrespective of fibre material or application, is that all variables in the drawing system are at equilibrium; they are constant. Examples of such variables are feed and draw velocities, neck temperature, deformation gradient, etc. This requires in practice that much fibre is pulled and that time has elapsed before the final product is uniform. In the techniques used here, the maximum length of fibre drawn at any one time was no more than a metre and a half. The preform was not fed into the furnace at all and so the system was basically unstable and a

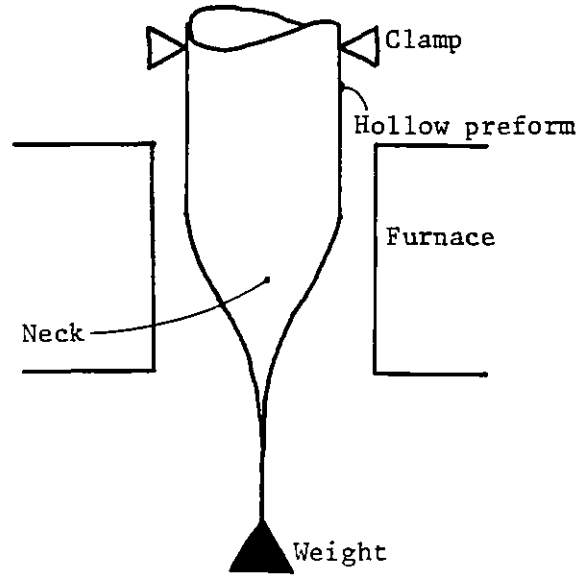

Fig. 5.1 Schematic arrangement of hollow fibre production method

definite value of maximum thread length existed. Some degree of taper in the final fibre was also inevitable. In this way, the technique is more akin to early experimental techniques used to study the spinnability of fluids[1]. (These methods employed the drop-loading of fluid threads suspended from glass rods). Despite the existence of such work and the increases in research effort in this field in the last twenty years, fibre drawing remains as much an art as a science. The early work produced qualitative results only, and while there now exists some foundation of knowledge for the prediction of drawing and spinning behaviour, the production method described here is more appropriately described by qualitative argument than quantitative analysis.

5.3 Preform Material

Elliptical bore capillary tubing was chosen as the preform material from which to draw hollow fibre. In order to satisfy conditions of simplicity and cheapness, a material melting at low temperature was required so that an electric resistance furnace could be used at the drawing stage without need for inert gas purging systems or extensive safety precautions.

Several possible choices for preform material were available. These were silica, lead-glass and Pyrex tubes with varying bore to outer-diameter ratios. Silica was rejected because of the necessarily high working temperature. Lead glass, although more transparent than Pyrex, was rejected because it was only available with very small bore to outer diameter ratios. This would have exacerbated the problem of preserving the bore during drawing and would also have increased the difficulty in launching light into the fibre during the final optical tests. Pyrex was finally chosen as a preform material because it was the easiest material to work with, was available with suitable bore to outer diameter ratios and also because some samples were available with partially elliptical bores as manufactured.

5.4 Furnace Design

Four possible approaches existed for the production of hollow fibre. The first alternative for fibre production was the employment of hand drawing by an experienced glass blower. Although hollow fibres of bore diameters down to 40 microns can be produced by hand, they are not small enough or uniform enough to permit stable single mode operation when filled with a liquid core. The next possible alternative was a hypodermic tube furnace. This was rejected because the hypodermic tube did not heat the fibre evenly and it was impossible to accurately control the internal temperature of such a furnace. The third alternative was the use of a large R.F. induction furnace. This was regarded as being unnecessarily elaborate. The furnace design which was finally evolved is shown below.

The screw clamp system in the brass head cap consists of two levels of three 120° spaced bolts. These provide the necessary adjustability for directing preforms vertically and in the centre of the hot zone.

The alumina tube was chosen to be sufficiently larger than the preforms to provide radially symmetrical heating and so that the hot zone might also accommodate a thermocouple for accurate temperature measurement and control.

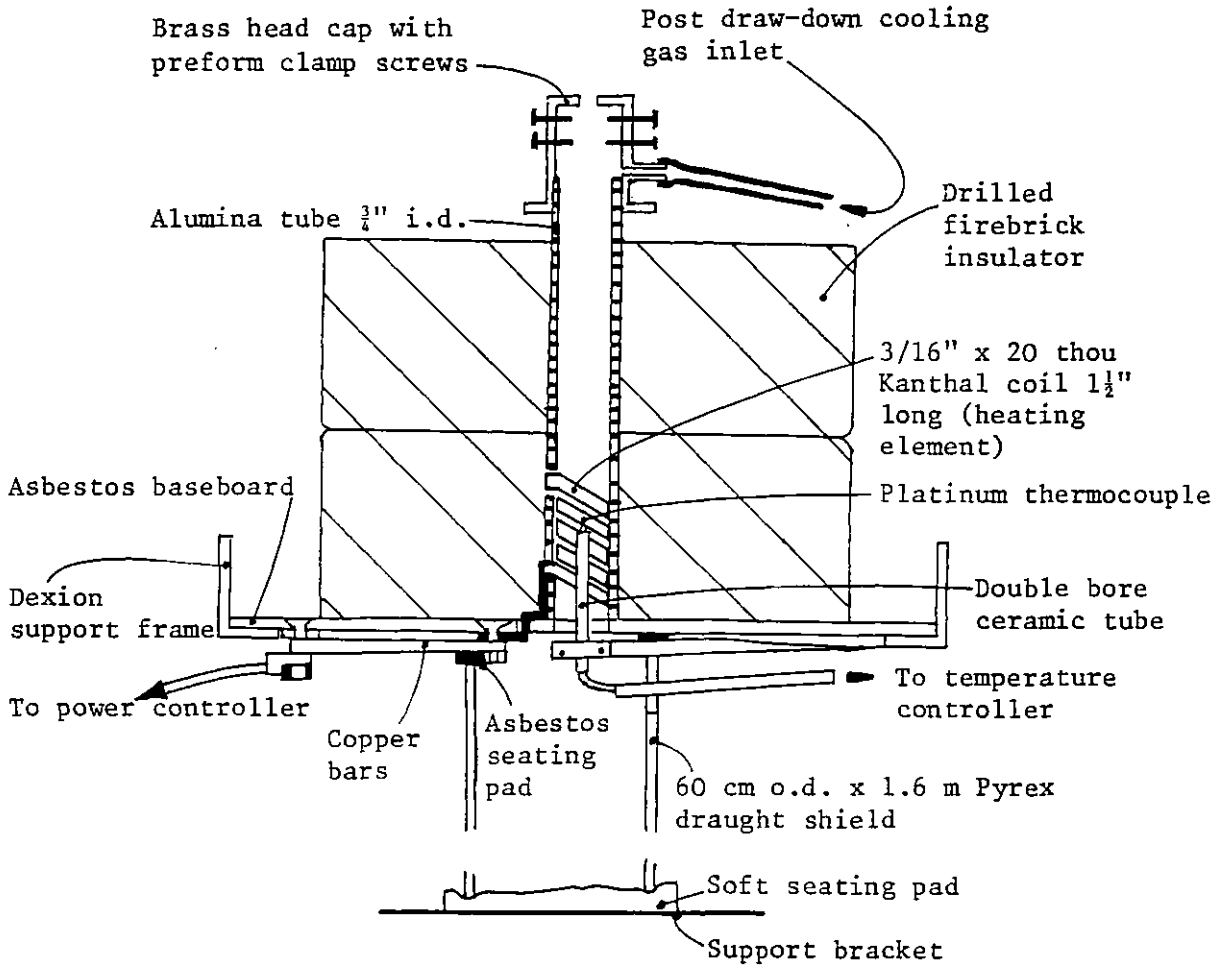

Fig. 5.2 Furnace Design

The Pyrex tube suspended below the furnace had two purposes. Firstly, it was used to prevent draughts from causing short term temperature variations in the furnace and thus to improve the uniformity of the fibre produced. Secondly, the tube was extremely useful for containing and protecting the fibre outfall after the drawing operation.

The heating element consisted of a Kanthal coil fixed inside the alumina tube. It was prewound on a former and slid into the tube. The only protruding elements are the short lengths taken down through holes in the baseboard for connection of power lines. The power is taken via a 200 amp 12:1 stepdown isolating transformer fed from a low current Variac supply and is governed during operation by a thyristor phase angle controller in the secondary of the isolating transformer. The circuit diagram is shown in figure 5.3. The thyristor unit is itself controlled by a feedback signal from the thermocouple in the hot zone. A proprietary temperature controller was used for this purpose, employing proportional plus integral plus derivative terms to maintain a preset temperature to better than approximately 0.5° C in the hot zone. The furnace current could be read at any time on the ammeter and the total available power was set manually at the Variac.

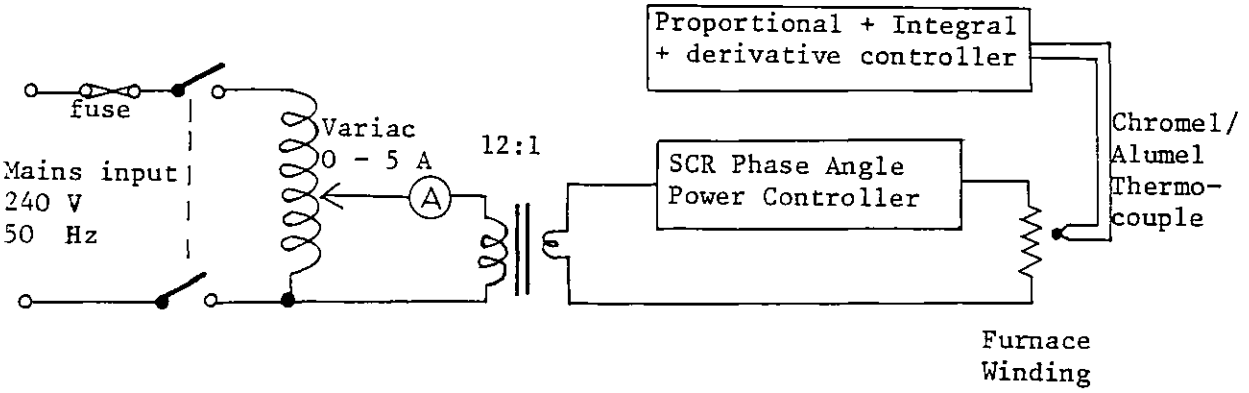

Fig. 5.3 Electrical System of Furnace

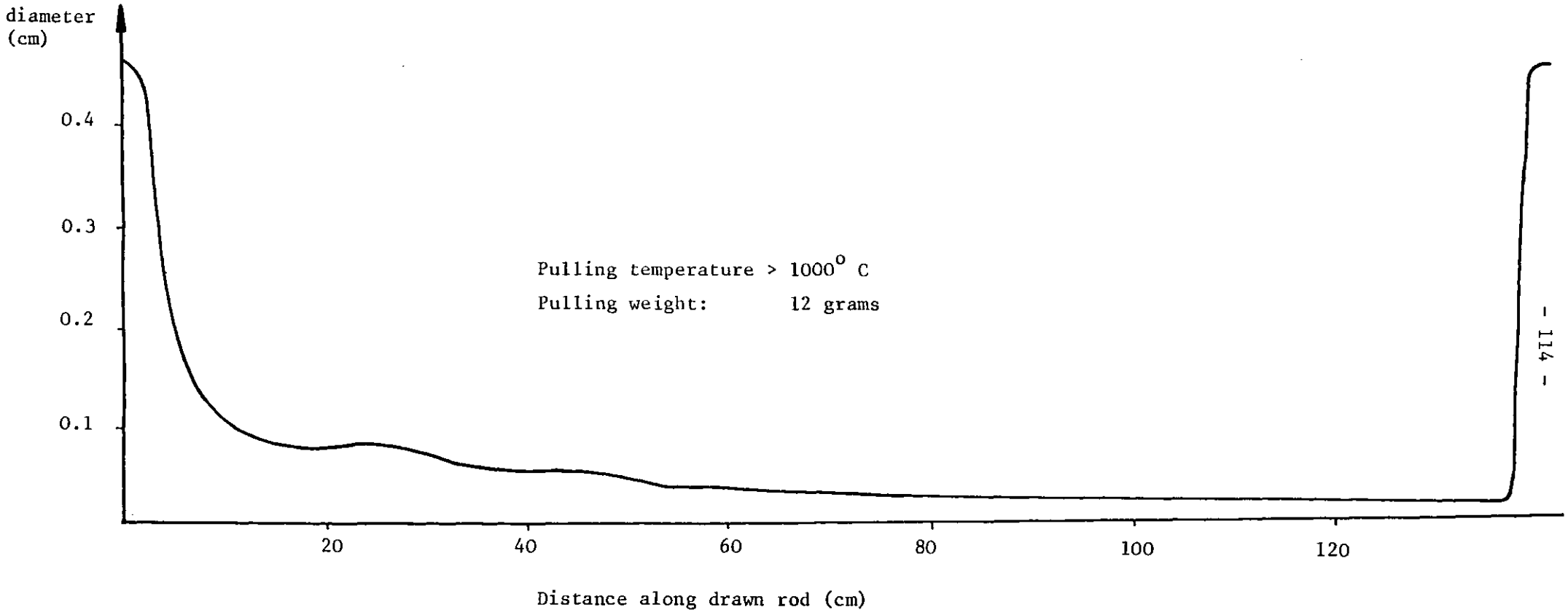

Fig. 5.4 Typical diameter profile of drawn Pyrex rod

5.5 Early Work: Drawing of Pyrex Rod

5.5.1 Method

The aim of the early rod drawing experiments was to investigate the conditions necessary to obtain fibre drawing at a convenient rate with a sensible combination of furnace temperature and pulling force. The pulling force was applied by attaching a weight to the bottom of the preform which was then clamped in the centre of the furnace. As heat was applied, the weight began to fall and was allowed to reach floor level before power was removed. This basic method was found adequate for all successive fibre drawing runs and was not changed.

Early weights used were too large for uniform fibre production. Their effect was to pull hot material from the hot zone of the furnace more quickly than the incoming slightly cooler material could be heated to the same temperature, and this accounts for the slightly uneven tapering of the typical final drawn rod, whose diameter variation with drawn length is shown in figure 5.4. This figure shows the lower end of the preform at the left and the upper end at the right. It will be obvious that the establishment of the neck in the typical case shown here occupied the first half-metre of the pull, the remaining section tapering uniformly toward the end of the fibre.

5.5.2 Necking Process

It was necessary during these experiments to gain some understanding of the drawing process. Now, the essential requirement for fibre drawing, whether transient or steady state, is that the material is continuous between drawn and undrawn sections which are stable in themselves. It is then a kinematic necessity that the velocity distribution along the specimen should be sigmoidal in shape, resembling one of the curves in figure 5.5.

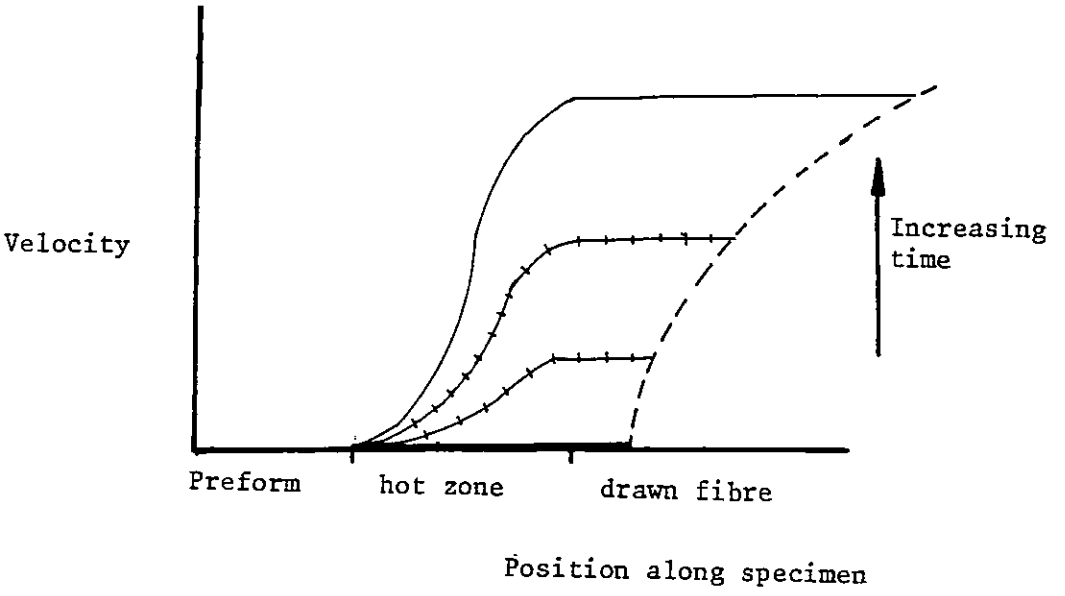

Fig. 5.5 Velocity distribution along drawn specimen

In the experiments reported here, preform velocity is zero, and as the neck approaches stability the shape of the curve changes with time. In standard fibre drawing, only the final curve would be relevant. For many polymeric materials, the undashed curve of figure 5.5 might be determined solely by the material deformation characteristics under the given drawing conditions, but this is not the case for glass under most practical conditions.

This being understood, it remains to be seen why a neck should approach stability as observed in these experiments. First of all, it will be clear that once the drawn section has reduced significantly in diameter with respect to the preform, considerable lengths of fibre can be pulled without removing a significant volume of material from the neck. Consequently its overall shape must be stable and so also its position with respect to its environment, the hot zone. Next, the hot zone has finite length and is placed at the bottom of the furnace. The temperature distribution along the rod is therefore very quickly varying and the viscosity is consequently increasing by many orders of magnitude down the neck. At the bottom of the neck the viscosity must be extremely high, or the fibre would break by local flow causing sudden thinning of the fibre at this point. Finally, the stress pattern may tend to prevent the neck from thinning further at the lower end since it is modified by the shape of the neck to become more nearly parallel with the axis.

This qualitative picture of the drawing process will suffice as background to the observations and discussions in the remaining part of this chapter. A complete analysis of the necking process could not be produced without extensive work and in any case sufficient rheological information about the behaviour of Pyrex may not exist.

5.5.3 Empirical Characteristics

The early experiments showed that, with the existing furnace, pull-down ratios of twenty to one in diameter were possible and that final fibre taper was likely to be better than 0.3% per centimetre. Taper was recognised as an important factor for projected optical experiments since a guide of workable length (1/2 metre) with good mode binding and also single mode over its entire length was necessary. This limited the variation in normalised frequency and hence core diameter to some 20%.

Change in the external ellipticity of the rod was also checked and was found to be better than the limits of simple measurement, i.e. better than 0.2%.

5.5.4 Second Stage Rod Drawing

A further obvious conclusion of the rod experiments was that it would be necessary to produce fibres by a two stage process since the draw-down diameter ratio between initial and final diameters of the Pyrex tubing would need to be nearer 400:1 than 20:1. Two stages of drawing are in any case desirable with the present technique, since there is an opportunity for greater control over the dimensions of the final fibre than with one stage.

Accordingly the rod samples drawn in the previous experiments were used as preforms for drawing down a second time in the same furnace. The existing furnace head clamp was too clumsy to support preforms of 500 microns diameter and so the arrangement of figure 5.6 was used for all second stage pulling experiments. Only modified sections of the furnace arrangement are shown. All other details are as shown in figure 5.2.

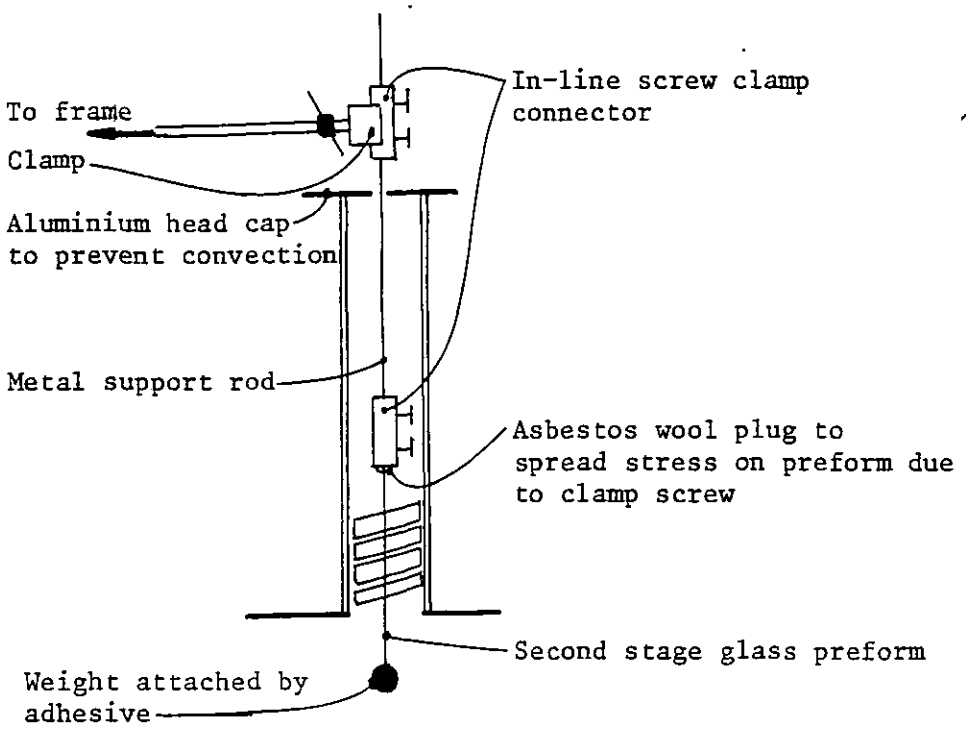

Fig 5.6 Modified preform support for second stage drawing

More care was needed to pull one and a half metre lengths of fibre with this arrangement. It was necessary to reduce pulling temperatures and stress levels. This is probably because the 1.5 m fibre length removed a proportionately much larger volume of material from the neck of the approximately 0.5 mm diameter preform than from the stage one 5 mm diameter preforms. To compensate for this effect, however, it must be remembered that the furnace hot zone length was also unchanged. Hence the proportionate length of the necking region was also longer for the smaller preform. It may be further noted that qualitative agreement with existing findings on the spinning of liquid threads was found here. The glass fibres were subject to breakage by cohesive fracture (i.e. exceeding tensile strength of the fibre) and this occurred at the base of the neck with high drawing velocities.

A typical result of a stage two draw run is shown in figure 5.7.

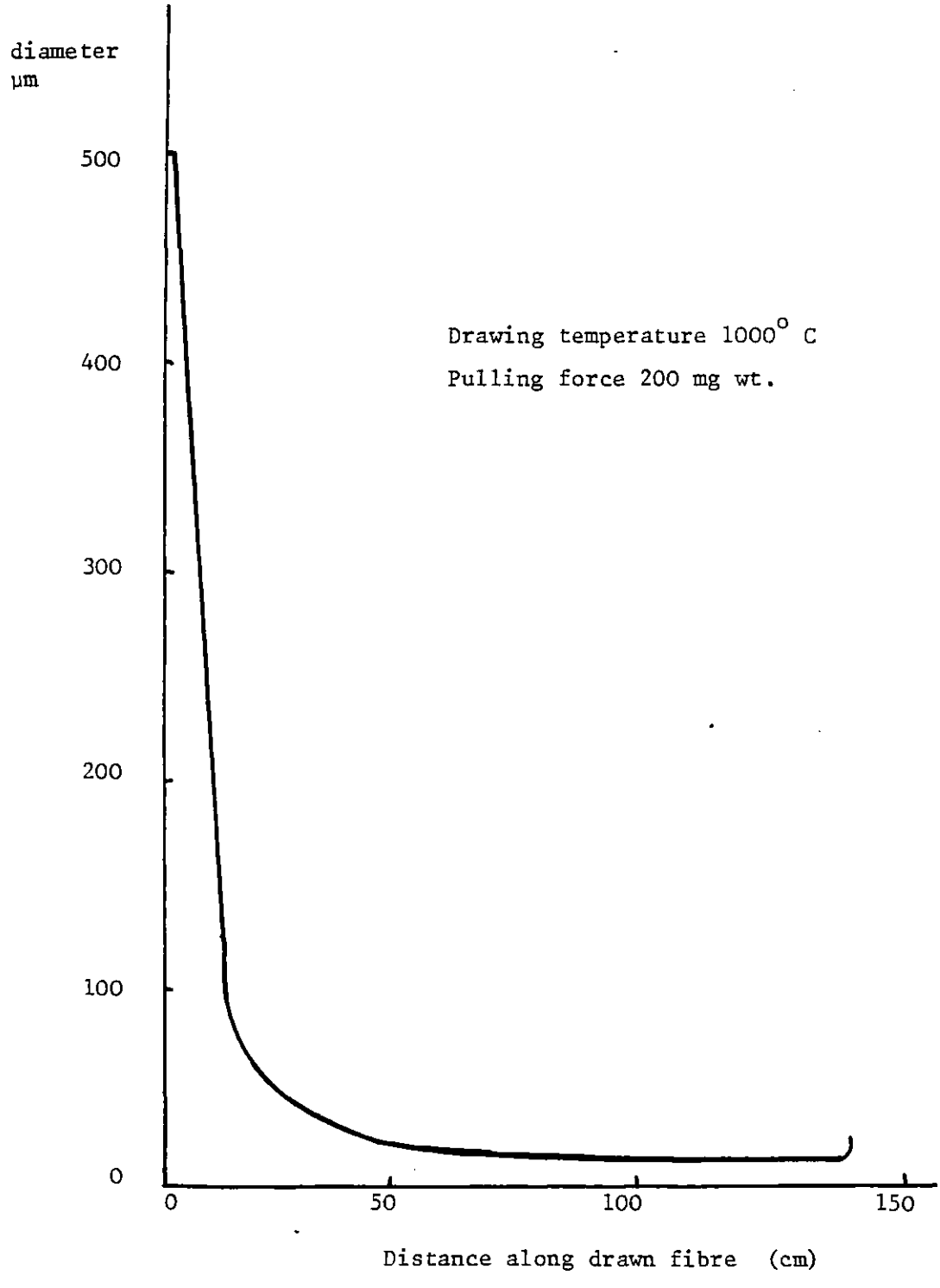

Fig. 5.7 Second stage of draw-down: typical result.

It is very instructive to note that the stability of the neck was found to be very dependent on the scale hot zone length. Experiments indicated that, at a fixed temperature the neck will stabilise very much more quickly with a short than with a long hot zone. In figure 5.7 it will be apparent that the neck did not approach stability until at least 60 mm of fibre had been drawn. This length is equivalent to 1200 preform diameters and the hot zone length in this case was about 50 preform diameters. An experiment carried out at a similar temperature with a 5 mm preform took only 40 diameters to stabilise with a scale hot zone length of 5 preform diameters. This shows that for large draw-down ratios and for limited fibre lengths for laboratory evaluation, short hot zones should be employed. Where very small draw-down ratios are required and again only limited lengths are needed for evaluation, very long hot zone lengths will produce the desired effect. This has been verified by work with hypodermic tube furnaces, where draw-down ratios of two to one are easily obtainable with very low taper - in this case due to the very slow neck formation and extremely extended approach to final stability.

All this is again in qualitative agreement with liquid thread investigations, where the maximum thread length is found to increase as the deformation gradient (inversely proportional to neck length) decreases. (This again assumes cohesive fracture)[1]. It must be stressed that neck formation in glass is entirely due to the method of treatment and is not a fundamental characteristic of the material. It is for this reason that the final fibre characteristics can be controlled to such a high degree.

5.6 First Stage Drawing of Pyrex Capillary Tube

5.6.1 Necking Process

Draw-down of Pyrex capillary tube was then tried. An early result is displayed in figure 5.8. Several salient points emerge here. The diameter profile shows the same behaviour as Pyrex rod. The second graph shows the variation of bore diameter as a fraction of local outer diameter for the drawn tube. Very significant bore shrinkage obviously occurred during the establishment of the neck. This was found to be a serious problem during early experiments.

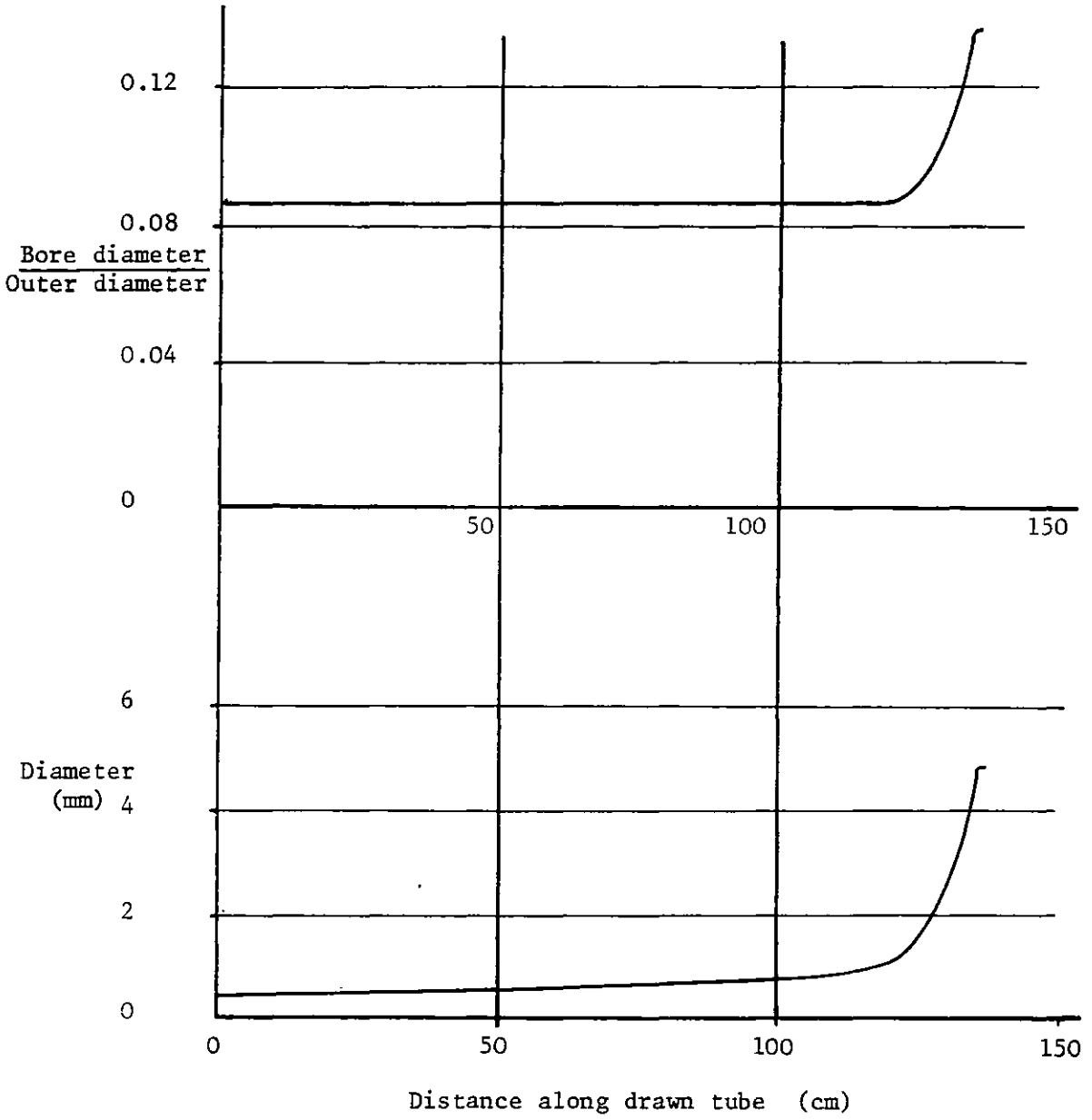

Fig. 5.8 Diameter profile and bore fraction as a function of drawn length for a single tube

The reason for the shrinkage of the bore probably lies partly in the nature of the stress pattern during necking. The stress during initiation of pulling is homogeneously distributed throughout the tube as a parallel stress pattern. This has an automatic shear component acting maximally at 45° to the tensile stress. In a homogeneous body the shear is balanced by symmetry, but at the walls of a bore there is no net force tending to counteract the shear, and since the glass is in a plastic state here, it will deform locally under the shearing action.

It was discovered that the principle effect which stabilises the bore to outer diameter ratio is probably due to the rheology of the material, but this will be discussed under the heading of second stage bore collapse where it assumes far greater practical importance.

5.6.2 Ellipticity Increase

The Pyrex capillary tubes used in the early drawing experiments were inexpensive and the bores were not precisely circular. In some cases the initial ellipticity amounted to as much as 30%. After draw-down, the ellipticity was found to have increased significantly in all cases. This was puzzling at first until an attempt was made to relate this phenomenon to the implications of the already noted bore shrinkage. A simple model for ellipticity increase was arrived at as follows. The argument is illustrated by figure 5.9.

The Pyrex capillary tubes were first assumed to draw down without any deformation of their relative geometry. This would have produced a cross section with a bore shown as contour 'A' in figure 5.9. This contour was compared with that made by the actual bore boundary, labelled 'B' in the diagram. It was found that the absolute shrinkage represented by the radial distance, x, between the two contours was equal on the principal axes of the bore ellipse. Such behaviour is predicted by the argument given to explain bore shrinkage in section 5.6.1. Bore shrinkage was attributed to unbalanced shear forces in the neck. These forces could be expected to be equal around the bore surface since the preform is essentially circular and the uniform stress distribution

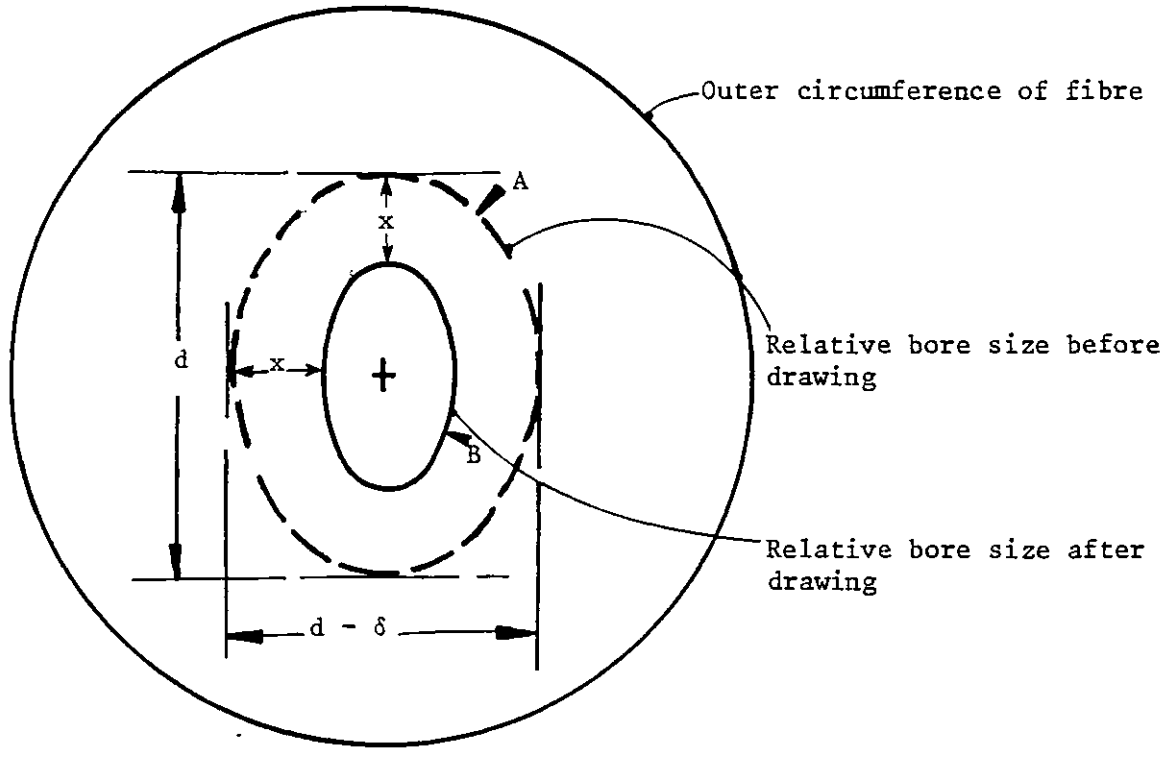

Fig. 5.9 Illustration of ellipticity increase

should not be greatly modified by the presence of a small, slightly elliptical bore. This assumption of symmetrical shrinkage is in agreement with the observations and explains the increase in ellipticity in the following way. The ellipticity ε_1 of the bore in the preform is given by:

$$\varepsilon_1 = \frac{\text{Major axis - Minor axis}}{\text{Major axis}}$$

$$= \frac{\delta}{d} \qquad \text{for contour A}$$

For contour 'B', that of the bore in the drawn fibre, the new bore ellipticity ε_2 is given by:

$$\varepsilon_2 = \frac{\delta}{d - 2x} > \frac{\delta}{d}$$

Thus the symmetrical absolute bore shrinkage has a greater relative effect on the minor axis than on the major axis of the bore.

5.7 Second Stage Capillary Drawing

Using the hollow fibre produced from the experiments described above as preforms for the second drawing stage, further problems were found. This was quite predictable on the basis that the end products from second stage draw-down are so small that even slight irregularities developing in deformation of the preform were bound to produce much greater relative effects on the geometry of the bores of final fibres (c.f. ellipticity change above). Because of this also, greater variation in results was encountered in second stage drawing experiments.

5.7.1 Bore Collapse

The problem of bore shrinkage has already been alluded to in section 5.6.1. Initially, total bore collapse was observed during second stage capillary drawing. It was found that far more care had to be given to drawing conditions to preserve the bore at all.

Various methods of preventing bore collapse were tried, including pressurising the bore and investigating the effects of temperature and stress. By far the most positive effect was that of stress. It was found that increasing the initial stress to levels much higher than used previously was of great benefit in obtaining fibres with continuous bore over the full one and a half metres. Reduction of pulling temperature was also found to be helpful.

With the Pyrex tubing used in this experiment, as much as 7.8 kPa was inadequate to guarantee a completely preserved bore at approximately 900° C hot zone temperature (see photograph of fibre section fig. 5.10, showing point of bore collapse) but at approximately 790° C this initial stress would preserve the bore totally. A section of fibre produced at the lower temperature was photographed (fig. 5.11) at the same diameter as that where bore collapse occurred at the higher temperature. Note the difference in

bore diameter of the two fibres as well as the continuity of the bore in figure 5.11. A section of fibre produced later at 790° C hot zone temperature and initial stress of 19.0 kPa is also included as figure 5.12 for comparison. Note the much greater improvement in bore to outer diameter ratio, which in this case is very close to that of the preform. All preforms used in these runs were between 570 and 580 microns in diameter, with initial bore diameter to outer diameter ratios of 0.22 to 0.27.

The samples of fibre photographed in figures 5.11 and 5.12 were drawn at the same temperature and these indicate that the effect of changing stress by a factor of two can be more important to bore preservation than a change in pulling temperature of 110° C. This evidence is corroborated by experience from stage one tube drawing. The stabilisation of the bore evidenced in figure 5.8 occurred at a stress level in the neck of approximately 28 kPa.

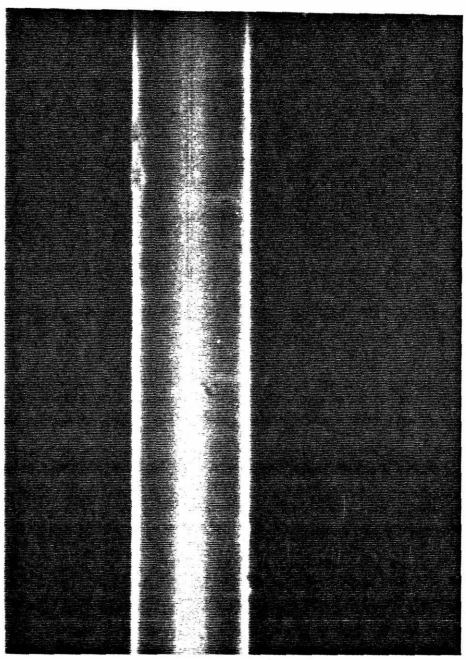

Fig. 5.10 Fibre Section with bore collapse
Fibre produced at 900° C and initial stress 7.65 kPa
(Initial bore/outer = 0.22)

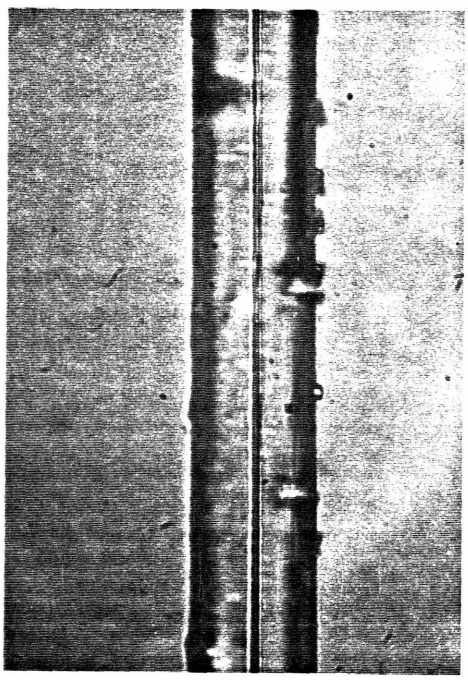

Fig. 5.11 Fibre section produced at 790° C and 7.06 kPa initial stress
(Initial bore/outer = 0.22)

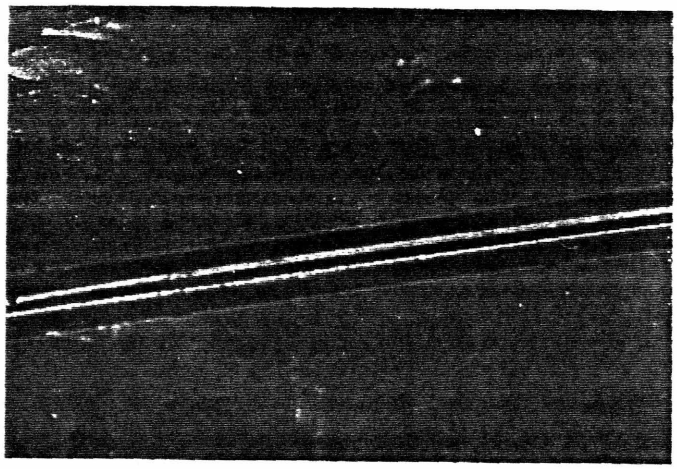

Figure 5.12 Fibre section produced at 790° C and 19.0 kPa initial stress

The behaviour described above was very surprising. Before experiments were begun, it was anticipated that high stress levels in the neck would contribute to, rather than prevent, bore collapse. The reason for this behaviour may be rooted in the rheology of the material. Until recently, it was believed that glass in the transition region and above is a Newtonian liquid (i.e. the viscosity is independent of stress). This is in direct conflict with expectations regarding the material's behaviour based on knowledge of its structure. The paradox was resolved by Bartenev[2] who showed that glass behaves as a Newtonian liquid only at moderate stress levels and above. At low stress levels and temperatures in and above the transition region, glass behaves as a visco-elastic material (i.e. it undergoes reversible deformations which take time to establish themselves and to disappear). Furthermore, the modulus of visco-elasticity is very small - about a thousand times smaller than the normal elastic stress modulus. The early transition between the two states was attributed to the ease of breakdown of the polymeric structure into simpler units.

Thus at low stresses, glass at high temperature can be expected to slowly undergo relatively large deformations. In the case of capillary tube drawing, the deformation of the bore walls due to unbalanced shear may then be quite significant. Thus, as was noted at the beginning of the chapter, a deformation which might go unnoticed in the preform could have a catastrophic effect on the final fibre. At high stresses, such deformation will not occur since the glass will behave in a normal, Newtonian-viscous manner. This argument agrees with Bartenev's findings in that the boundary between viscous and visco-elastic deformation was found to occur at about 9.8 kPa for alkali silicate glass in the transition region - a value fully compatible with the figures from the experiments reported here.

The temperature dependence of this effect is somewhat complex, since the Newtonian-viscous threshold stress increases as temperature is raised, but the deviation from purely Newtonian flow is reduced and the time taken to reach equilibrium is much increased. It may also be that at high temperatures and small sizes surface tension forces become more prominent in aiding bore collapse.

It was found that ellipticity was stabilised when the problem with bore collapse was solved. This was despite the existence of some residual bore shrinkage during second stage drawing. It is conjectured that the remaining bore shrinkage may be due to other effects than those discussed earlier, for example surface tension effects, and these may have a different influence on the bore ellipticity.

5.7.2 Fracture Mechanisms

As might be expected, far more trouble with fracture of the fibre was found in stage two than in stage one. The problem was made critical by the fact that in order to prevent bore collapse, initial stress had to be kept high. Thus the working stress in the neck and fibre during the useful drawing period was very high - of the order of 150 kPa (tensile). This led to considerable liability to cohesive fracture of the fibre at the base of the neck.

A second source of fracture was due to heat generation within the neck. Pulling fibre against viscous resistance in the neck generates heat. Although the total heat generated was small, amounting to some five watts at most, this nevertheless was being generated within a very small volume in the neck and no doubt raised the neck temperature above that of the surrounding hot zone. In early experiments this led to thermal runaway of the drawing process and either fracture of the fibre or total bore collapse.

A third source of fracture and weakness in the fibres produced was due to partial devitrification of the glass. Reference to figure 5.11 will show that the fibre shown there, produced at 790° C has melted incompletely and that there are small irregularities on its surface due to small crystallites that have grown during the drawing process. This has occurred because of the slowness of the drawing process and the proximity of the pulling temperature to the transition region.

5.7.3 Fibre Uniformity

Tests showed that after the problems described earlier had been solved, the drawing process produced fibre which was of sufficiently good quality and had sufficiently predictable characteristics to be used for optical tests. Figure 5.13 shows the result of a test carried out to check fibre uniformity from second stage tube drawing. It is clear that over lengths of up to 10 cm, the diameter of the fibre was stable to about ± 8% with most of the variation in diameter being due to a short range sawtooth diameter fluctuation superimposed on the long range uniform gradual taper. This sawtooth variation was regularly seen and is believed to be the result of residual temperature fluctuations within the furnace and was regarded as a practical limit with the equipment and method used here.

Within the limits of measurement (∿ ± 10%), the ratio of bore major axis to outer diameter (or fibre major axis) remained constant along the fibre length. The bore ellipticity was, however, seen to vary significantly along the length of drawn fibre, these variations being correlated with variations in the fibre diameter. These variations in ellipticity enforced a final direct examination of the particular sections of the fibre used in the optical experiments so as to more accurately determine the actual bore ellipticity. This examination was accomplished by scanning electron microscopy and was necessary for comparison between the predicted and observed propagation characteristics.

5.8 Summary of Short Fibre Production Technique

We have seen that the short fibre production technique can produce lengths of hollow elliptical bore tube suitable for optical experiments. The standard drawing conditions were very critical for second stage drawing to produce the final tubes and were set so that, using the equipment and method described, the initial stress in the preforms was 49 kPa and the furnace temperature was set to an initial value of 780° C. Under these conditions, the elliptical

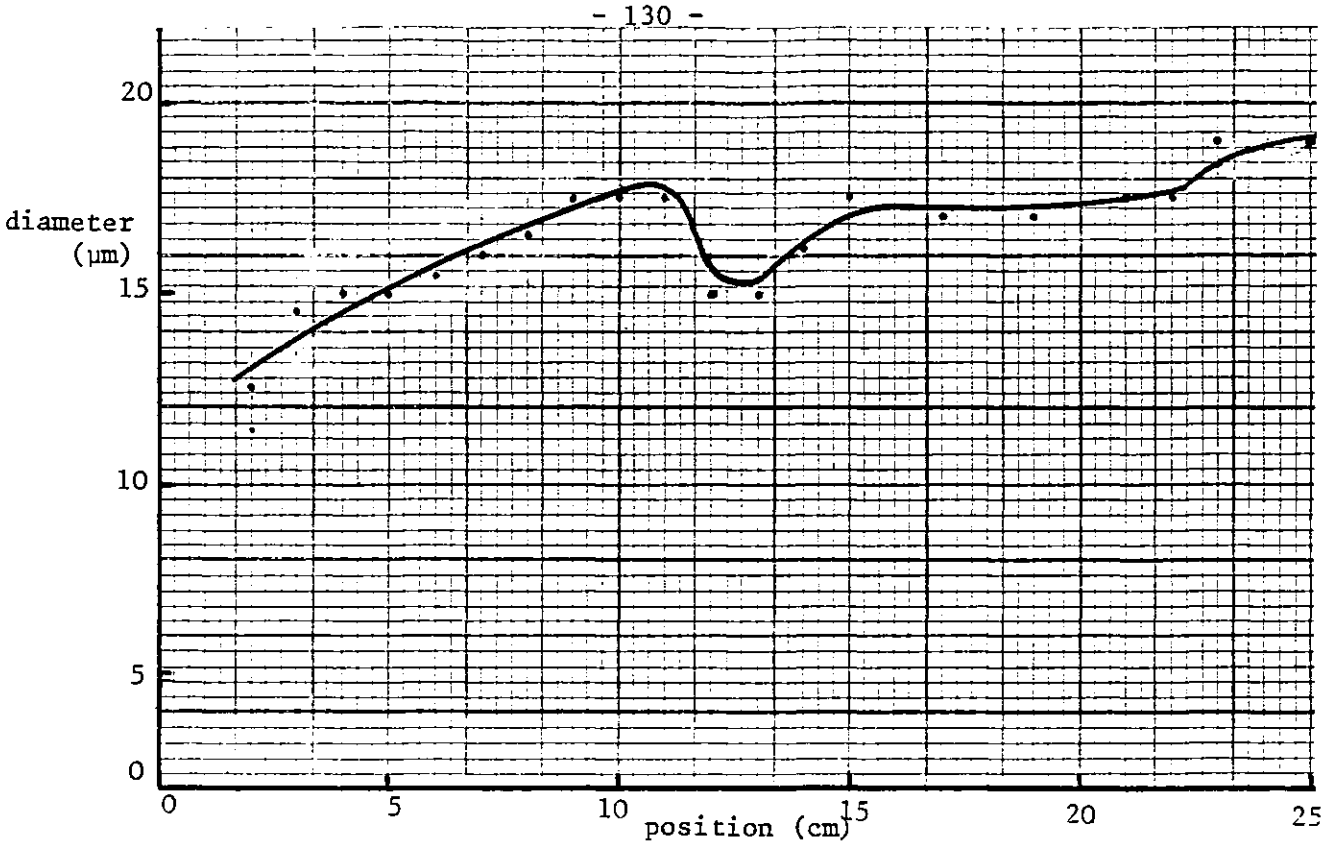

Figure 5.13 Variation of fibre outer diameter with position for a typical Pyrex second stage drawn tube

bores shrank by 20% but did not significantly change in ellipticity. Outer diameter ratios between preform and useful fibre were typically near 30:1.

A range of fibres for optical experiments were made in the following way. Pyrex capillary tubing of 5 mm outer diameter and bore to outer diameter ratio of 0.027 was chosen as the starting material. This tubing was given to a professional glass blower, who partially remoulded the tube into lengths having ellipticity. These lengths were drawn in the furnace described in a first stage process. This first stage tube product was then cut into approximately 10 cm lengths so as to produce batches of preforms each with a particular geometry. Because of the taper involved in the stage one process, a large range of preform diameters were produced within each batch, but within each batch all preforms had similar geometry.

Fibres were next produced from these preforms by first choosing an approximate desired optical design and selecting the particular preform likely to produce fibre of the correct geometry. These

preforms were then drawn in a second stage process, examined with the aid of an optical microscope, and if suitable were wound onto glass cylinders and stored until needed for optical experiments. Figure 5.14 shows an optical micrograph of the cross section of one of the preforms produced by stage one drawing, while figure 5.15 shows an electron micrograph of the final fibre produced from that preform.

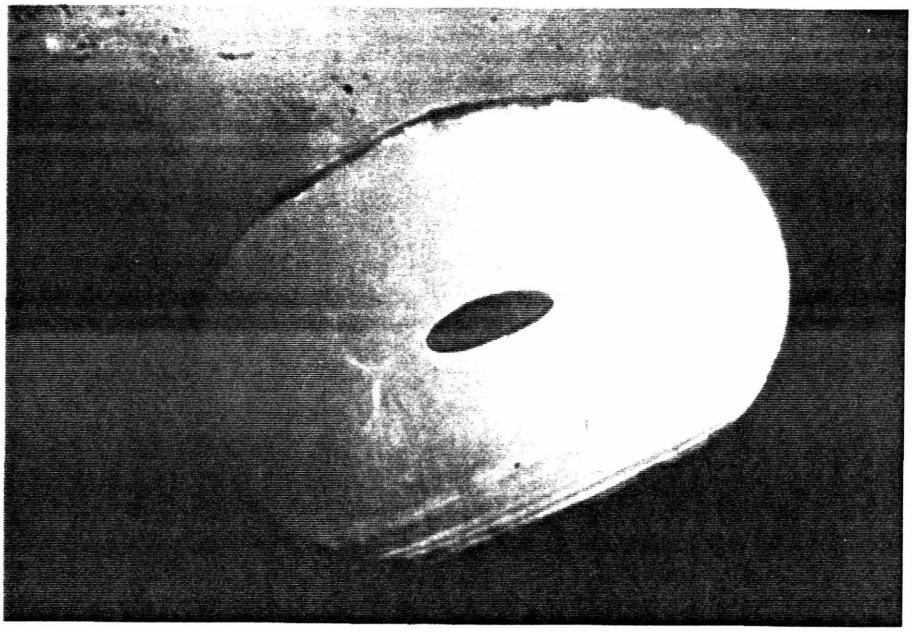

Fig. 5.14 Cross section of preform from stage one drawing

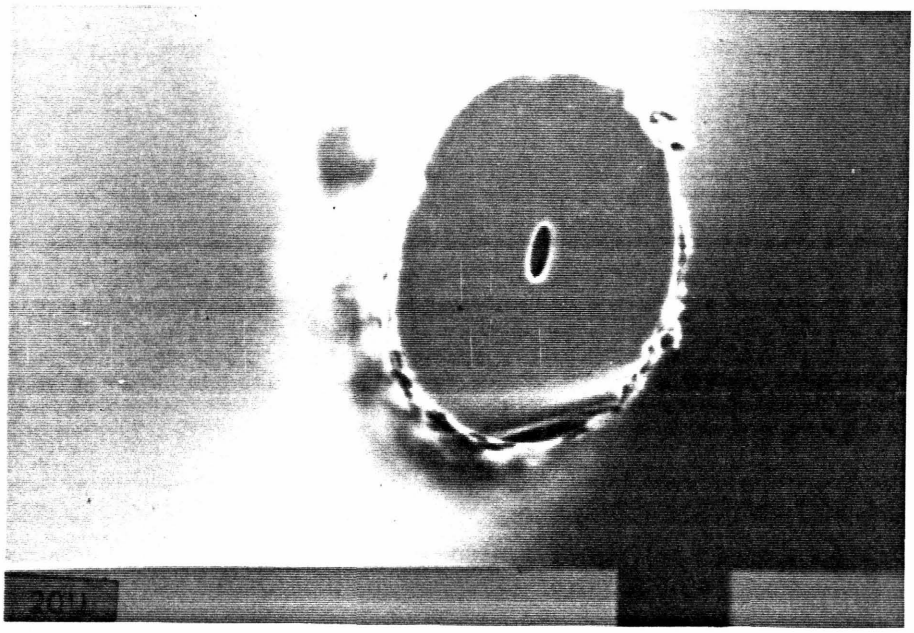

Fig. 5.15 Cross section of fibre produced from preform shown in fig. 5.14

References to Chapter V

1. ZIABICKI, A.
"Fundamentals of fibre formation"
(London, Wiley, 1976) p. 13 et seq.

2. BARTENEV, G. M.
"The structure and mechanical properties of inorganic glasses"
(Groningen, Netherlands: Wolters Noordhoff; 1970)

CHAPTER VI

PRODUCTION AND TESTING OF LIQUID CORED ELLIPTICAL GUIDES

6.1 Design and Production of Liquid Cored Elliptical Guides

Elliptically cored fibres were designed to conform to practical constraints while testing the $\Delta\beta$ calculations over the most important part of the range of interest.

To begin, a target ellipticity was chosen and then a suitable preform was selected from stage one drawn stock. This selection was made on a predictive basis relying on stage two draw-down experience. Reliance was placed on the natural taper inherent in the drawing process to provide a suitable range of fibre and bore diameters for the optical tests. Since control of the drawing process was imperfect, it was necessary to examine the resulting fibre samples with an optical microscope. Bore ellipticities and sizes were estimated for test samples at this stage by optical examination of fibre ends further toward the large end of the tapered section.

Desired index differences were selected to meet two requirements. First, that a particular V value should be achieved in the tested sample of fibre and, secondly, that birefringence should be measurable by the cut-back technique. A liquid of the correct index to produce the desired index difference in the fibre was next produced by carefully mixing liquids of known index in exact proportions. In the final stage of production fibres were filled with the mixed liquid. This was accomplished by driving the liquid into the fibres under pressure.

6.1.1 Selection and Handling of Liquids for Fibre Cores

It was appreciated from the outset that this work would involve extensive, close handling of the liquids needed for the fibre cores. Commercially available refractive index liquids are toxic and unpleasant to work with and so were judged unsuitable for these

experiments and alternative liquids were sought. The refractive index of a Pyrex sample was measured at 633 nm with the aid of an Abbé refractometer. This yielded a value of $1.4725 \pm 2 \times 10^{-4}$. Accordingly, non-toxic liquids with indices higher than this were needed. It was also necessary that they should be mutually miscible without chemical change, have low viscosity for easy fibre filling, should be relatively clear, reasonably pleasant to work with and not be optically active.

It was found that there are certain organic oils normally used in the food, pharmaceutical and cosmetics industries which fulfil these requirements. Four oils were chosen as being particularly suitable for these experiments and samples were procured. The refractive index of each was measured with the Abbé refractometer and the results appear in Table 6.1.

Oil	Refractive index at 633 nm and 20° C
Anise Oil	1.548
Ceylonese Cinnamon Oil	1.531
Palmarose Oil	1.472
Oil of Rue	1.428

Table 6.1 Refractive indices of various oils

To make liquids of desired refractive index, the above liquids were mixed. It was at first assumed, and later verified, that there was a linear dependence of resultant index on the concentration of one liquid within another, i.e. for a mixture of two liquids:

$$\alpha = \frac{(n_F - n_L)}{(n_H - n_L)} \qquad 6.1$$

Here n_F = final index of mixture
n_L = refractive index of lower index liquid
n_H = refractive index of higher index liquid
α = fraction of total volume occupied by liquid n_H

The mixing was accomplished within calibrated hypodermic syringes which were used to extract precise volumes of the oils from their storage bottles. Contamination of the storage bottles was avoided by changing the disposable hypodermic needles between extractions. All mixtures were checked for accuracy of the resultant index by means of the Abbé refractometer. It was found that Palmarose and Cinnamon oil mixtures were stable over periods of weeks. Optical activity of these liquids was checked by passing a polarised laser beam through glass vessels containing the liquids, and it was confirmed that no significant activity was present.

6.1.2 Filling the Elliptical Tubes

Early filling tests relied on surface tension for drawing the liquid into the micron scale bores. These tests showed that this method was impracticably slow and so a pressure assisted filling technique was adopted. A pressure vessel (shown in figure 6.1) was constructed to hold the core liquid and the elliptical bore tube. One end of the tube was open to the atmosphere while the other was sealed beneath the surface of the liquid within the vessel. An indium/tin solder was found to be most suitable for sealing the fibre in position. The fibre was held in a threaded plug which was removed from the main body for insertion, positioning and sealing operations.

The filling operation for each fibre commenced with preparation of a suitable length of chosen fibre. After cutting the inlet end of the fibre, great care was taken to prevent blockage of this end. The fibre was always fed through the plug by placing the outlet end in the reservoir area and pushing the fibre through the plug until it protruded from the outer end of the plug. The fibre was then pulled through from the outer end of the plug until the inlet end was within

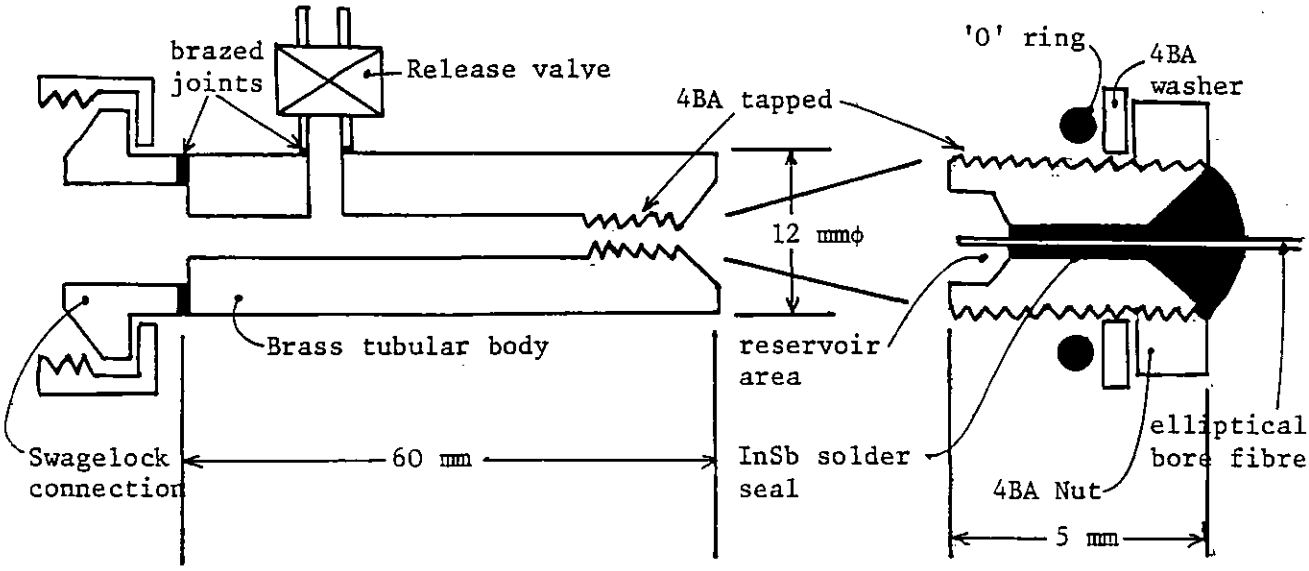

Figure 6.1 Pressure vessel

the reservoir area. This operation was monitored by means of a stereo zoom microscope. The reservoir area of the plug, being recessed, served to protect the inlet end of the fibre from contamination when the plug was screwed into the main body.

After the desired core liquid had been introduced into the pressure vessel by means of a hypodermic syringe, the vessel was connected to a gas supply, as shown in figure 6.2.

Enough mixed liquid was introduced into the pressurised reservoir to cover the inlet end of the fibre with the reservoir held at approximately 45° to the vertical, as shown in the above figure. This allowed the fibre to be led onto the table of a microscope which was in close proximity to the gas system. The microscope was used to follow the progress of the filling operation as it was happening so that blockages and other irregularities could be detected. Obviously it was also possible to detect completion of the filling operation using this instrument. The length of fibre to be filled normally exceeded the available travel of the microscope

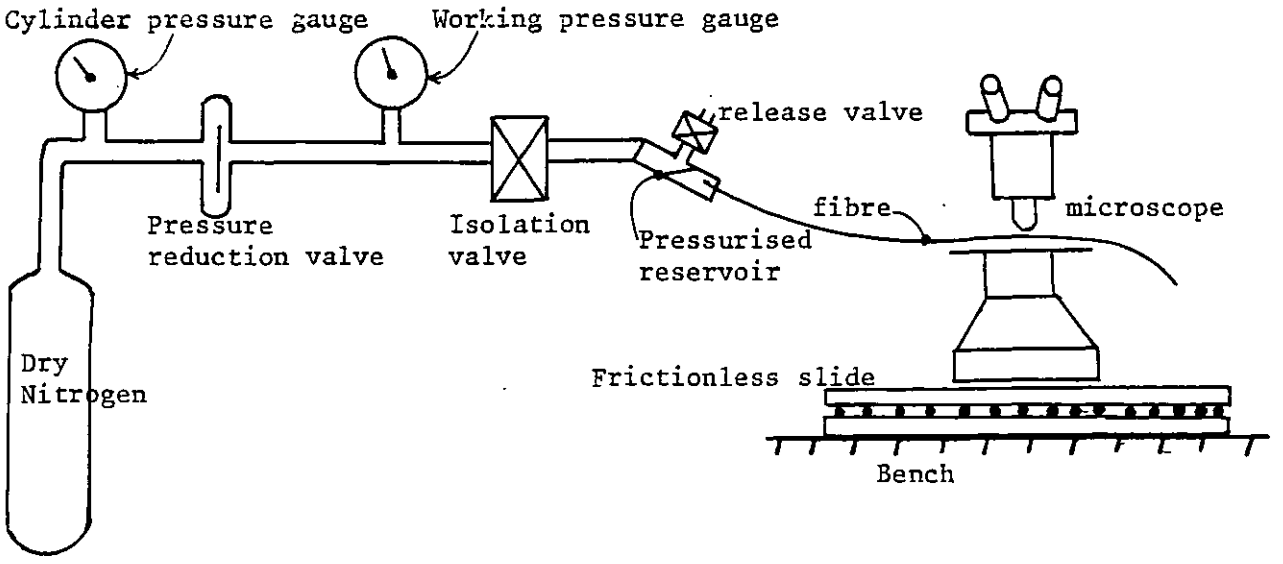

Figure 6.2 Filling System

table. In addition it was not desirable to bend fibres unduly while being filled in case breakage of the fibre occurred at the point where it emerged from the sealing plug. For these reasons, the microscope body was mounted on a linear frictionless slide which allowed the whole operation to be monitored without any danger to the fibre. Reservoir pressure was normally set at seven atmospheres (105 psi) and this was sufficient to fill about 10 cm of fibre with a bore diameter of 2 microns minor axis in about five minutes. After filling, the fibre was normally broken at the point where it emerged from the sealing plug, which was then drilled clear of solder ready for re-use.

6.2 Optical Tests of Normalised Birefringence

6.2.1 Equipment

The optical tests of normalised birefringence were carried out by a cut-back technique developed from that employed for solid core fibres, as described in chapter three. Accordingly, the layout of

the optical train was very similar to the earlier experiments. The arrangement used for the new tests, shown in figure 6.3, embodies only two differences from the equipment of chapter three.

The first major difference is that only short fibre lengths were used - less than 10 cm - due to fabrication and uniformity constraints. The fibres were supported on microscope slides and immersed in benzyl benzoate cladding mode stripping liquid over the entire length of support. Only very short lengths of fibre - a few millimetres - were allowed to protrude from each end of the support. In this way light scattered from the cores of the fibres was prevented from interfering with the measurement, by ensuring that very little cladding light was present at the output ends. These measures were necessary because these fibres were found to scatter guided light strongly, most likely due to interface defects and impurities in the core liquids. Such scattering was not of Rayleigh character and so suppressed the formation of any beat pattern.

Because much light reached the rear end of the supporting microscope slide, it was necessary to visually check that the collimating lens was focused on the fibre end. This was achieved by using the adjustable telescope with eyepiece inserted during alignment. For polarisation measurements, the eyepiece was removed. Both objective lenses were selected for low birefringence, each having a retardation of less than two degrees at 633 nm.

6.2.2 Method

A number of phase delay measurements were necessary on each of many test fibres. However, it was anticipated that the behaviour of these fibres would be much simpler than that for the solid core fibre in chapter three. Also, because of the large number of measurements involved in the liquid core test programme, it was important to minimise the time taken for each measurement. In view of these two considerations it was decided to simplify the measurement technique from that described in chapter three.

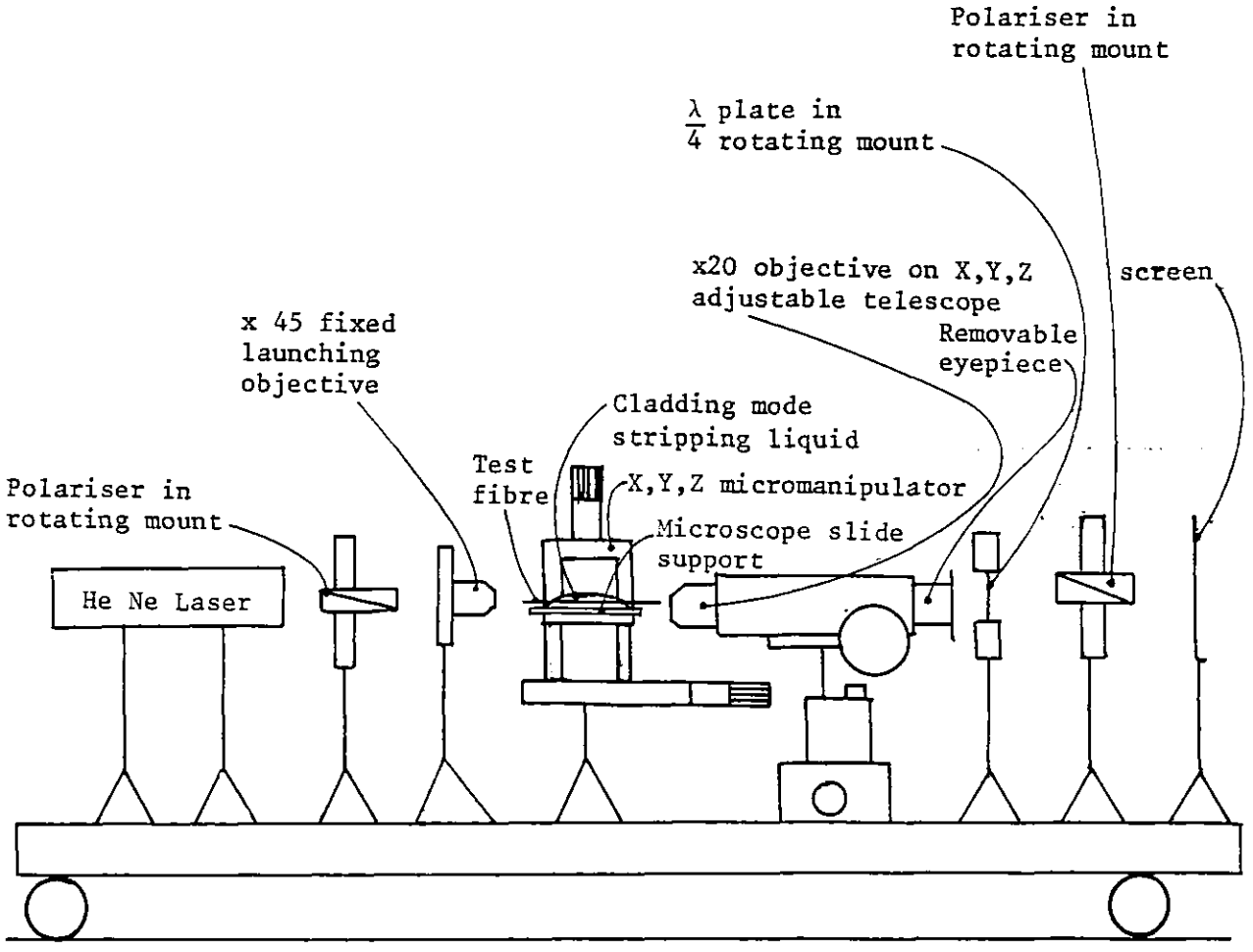

Figure 6.3 Optical layout for normalised birefringence tests

It was found that the privileged axes of the fibres could be located by iteratively adjusting the input and output polarisers to achieve extinction in the absence of the quarter-wave plate. As a check on accuracy, the relative orientation of the polarisers for extinction was checked beforehand and compared to the new relative orientation with the fibre in place. If the two relative orientations disagreed by more than a few degrees, the iteration process was repeated. This was done because the fibres were known to be reasonably uniform, stress free and untwisted so that the privileged axis directions at the launch and radiation ends had to be identical.

The advantage of this technique was to save time by eliminating the necessity of sweeping through a full eighteeen individual extinction measurements in order to identify the privileged axes of a length of fibre.

Once the privileged axes had been found, the input polariser was rotated to launch light at 45° to the privileged axes. The output polariser was then rotated in order to produce minimimum transmitted intensity. The new orientation of the analysing polariser was then used to set the orientation of a quarter-wave plate introduced after the fibre and finally an extinction of the compensated light was obtained. The reason for this sequence is explained in 3.1.2. The difference, θ, between the penultimate and final orientations of the analysing polariser gave the basic retardation angle, δ, in the following manner.

Equation 3.3, the relation between observed intensity ratio and the net phase difference between the two privileged waves, is repeated here:

$$\cos \delta = \frac{(1 - Q)}{(1 + Q)} \qquad 3.3$$

But since $Q = \tan^2 \theta$ (see fig. 3.1), $\delta = 2\theta$ by standard trigonometric manipulation. Thus the retardation of the sample of fibre was immediately derived from the appropriate analyser orientations. As a check, the quarter-wave plate and polarisation analysing crystal were iteratively adjusted for best extinction and the difference in their orientations for the iterated condition was ccompared to the difference for the pre-iterated condition. If these two results differed by more than a few degrees, the measurement was rejected.

Having found the net retardation of the fibre sample, the length of the sample was measured and the fibre was cut back for a further measurement. Cutting back was achieved by sandwiching the fibre between two microscope cover slips and breaking off the unwanted, protruding fibre section against one slip. This technique minimised any bending of the retained section of fibre and was necessary because bending of the fibre tended to expel liquid from the bore near the fibre end. This in turn was undesirable because it would have caused launching difficulties, led to instability in the optical retardation measurement and uncertainty in the length measurement.

The number of retardation measurements made on a particular sample of fibre was not uniform. Fibres with different specific retardance required different numbers of measurements to establish their absolute retardation versus length relations, as explained later.

When measurements were complete, remaining lengths of the samples were cleaned and were examined by scanning electron microscopy (SEM), in addition to any available samples of fibre from immediately adjacent parts of the fibre from which the tested sample was taken. This was done to measure the exact dimensions of the fibre samples. It was mentioned earlier that optical microscope measurements of the fibre dimensions were originally taken further toward the large end of the taper only as a guide for sample design.

Preparation of the specimens for SEM examination was carried out as follows: The fibres were cleaved from the experimental sample in 1 cm lengths and were glued to specimen stubs with araldite. The specimens were then ultrasonically cleaned in baths of isopropyl alcohol and toluene for five minutes each and then were ultrasonically rinsed in absolute alcohol for a further five minutes. Drying was carried out in a vacuum chamber at ambient temperature. Finally the specimens were sputter coated with gold to a thickness of ten Angstroms.

6.2.3 Limitations of Method

The measurement method described above was determined partly by time constraints and equipment availability. In addition, the nature of the fibre samples did not allow more elaborate techniques to be used. It was very difficult to quantify the errors involved in the technique, particularly as these varied from fibre to fibre. The most significant errors were thought to be due to limitations to the determination of the index differences of the fibres. Errors here would affect the calculations of both V and $\Delta\beta_N$. Such errors would have different effects on each fibre sample depending on the index difference of that sample.

In general it appeared that the most reliable results were available from those samples employing the highest index differences. For good stability of the phase measurements, it was necessary to maintain the index difference above 7×10^{-3}. However, it was simultaneously also necessary that the beat length of any sample should be greater than 3.6 cm in order to render the results interpretable in terms of absolute retardation. A further limit was imposed by cladding light preventing measurements on fibre samples less than 1 cm in length.

The major disadvantage of the measurement method employed was that the retardation measurements were relative in nature and not absolute. Retardation values were in principle distributed about integer multiples of 180° retardation. This allowed room for

subjective consideration to influence the results and so ideally all samples should have been measured at length intervals very much less than a beat length. This would have allowed a straightforward derivation of the sample's birefringence. However, practical constraints did not allow this in all cases and it was then necessary to take many measurements of retardation over several beat lengths and to use graphical display of the possible values of absolute retardation to identify a best fit straight line to the experimental points. The best and worst examples of such results so obtained are shown in figures 6.4 and 6.5 respectively.

Two final limitations on the method should be noted here. So far, it has been tacitly assumed that the refractive index of Pyrex in fibre form is identical to the bulk value. This was confirmed to be approximately true for most fibre samples when checked by the immersion method. However, two drawing runs produced fibres of different index which had to be measured from the fibre samples themselves. This was accomplished using the Abbé refractometer to an accuracy of $\pm$ 3 x 10^{-4}. The second limitation also relates to the accuracy of the index difference. The liquids used were all sensitive to temperature, changing their refractive index in a similar way as temperature varied. Experiments were carried out while constantly monitoring the ambient temperature to prevent errors due to temperature fluctuations.

6.2.4 Results

The results of the birefringence measurement experiments are detailed in table 6.2 and are shown graphically in figure 6.6. It is clear that despite variable errors, the effect of large ellipticity is to greatly increase the normalised birefringence of the fibres. In addition, the three results in figure 6.6 labelled 51 A, B and C clearly confirm the correct peaking behaviour of the $\Delta\beta_N$ curves as V is varied.

Fibre No.	SEM Results		Refractive Index Measurements			V	Birefringence Measurement		
	Minor axis core diameter, 2b, (μm)	Ellipticity $\frac{a}{b}$	Core Liquid Index n_1	Clad Index n_2	$\Delta n = n_1 - n_2$		Specific Retardation (°/cm)	$\Delta\beta_N$	Theoretical Computed $\Delta\beta_N$ at same V
44	0.77	1.30	1.4827	1.4725	0.0102	0.66	25	0.042	< 0.01
45B	1.82	1.41	1.4918	1.4725	0.0193	2.16	165	0.078	0.091
45C	1.60	1.36	1.4790	1.4725	0.0065	1.10	3.9	0.029	0.074
45D	2.10	1.32	1.4800	1.4725	0.0075	1.55	29	0.092	0.091
45E	1.60	1.38	1.4870	1.4725	0.0145	1.64	131	0.110	0.103
50C	1.72	2.95	1.4783	1.4730	0.0053	1.07	75	0.353	0.298
51A	1.94	2.99	1.4779	1.4749	0.0030	0.91	11	0.216	0.260
51B	1.50	2.99	1.4849	1.4749	0.0100	1.30	180	0.316	0.286
51C	1.82	2.99	1.4856	1.4749	0.0107	1.62	122	0.196	0.234

Table 6.2 Results of the measurements made on fibre samples for birefringence tests

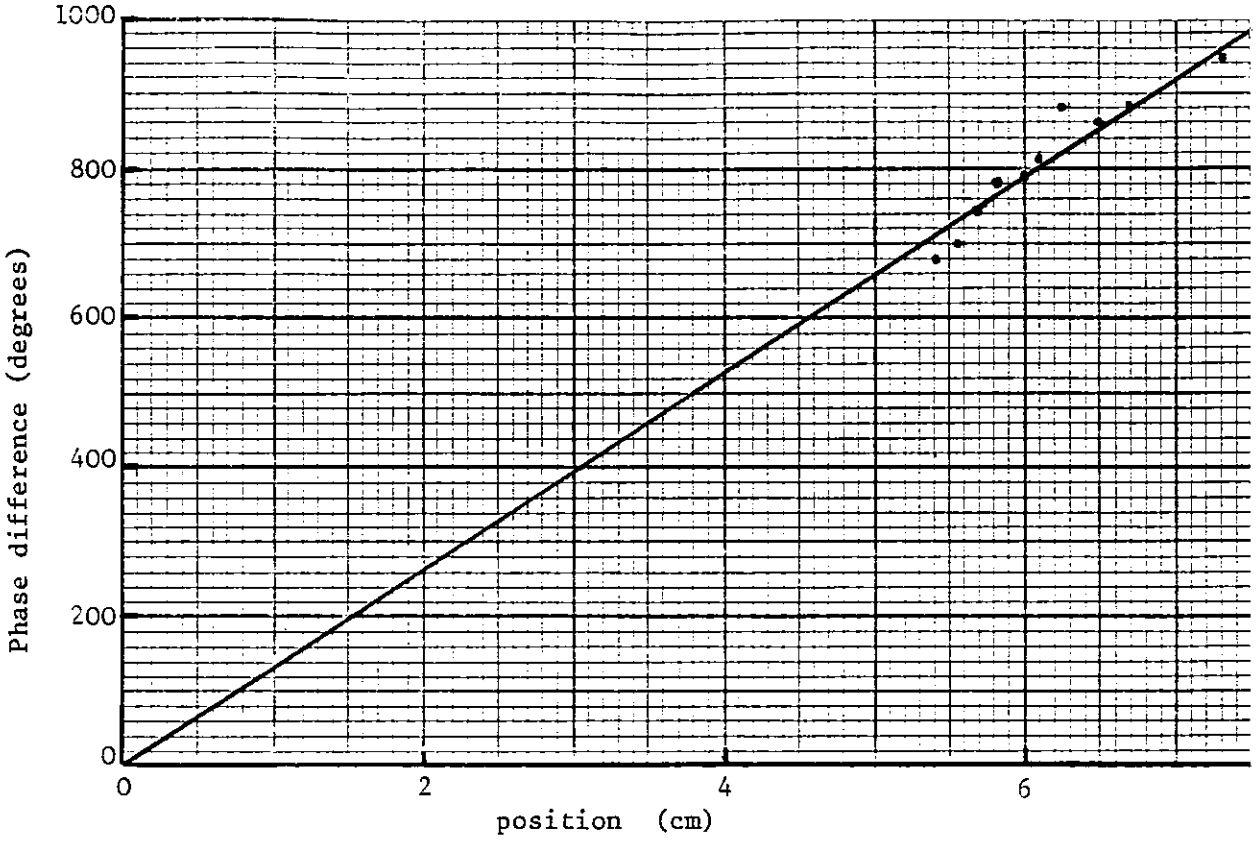

Figure 6.4 High confidence estimation of extended retardation measurements (run 45E)

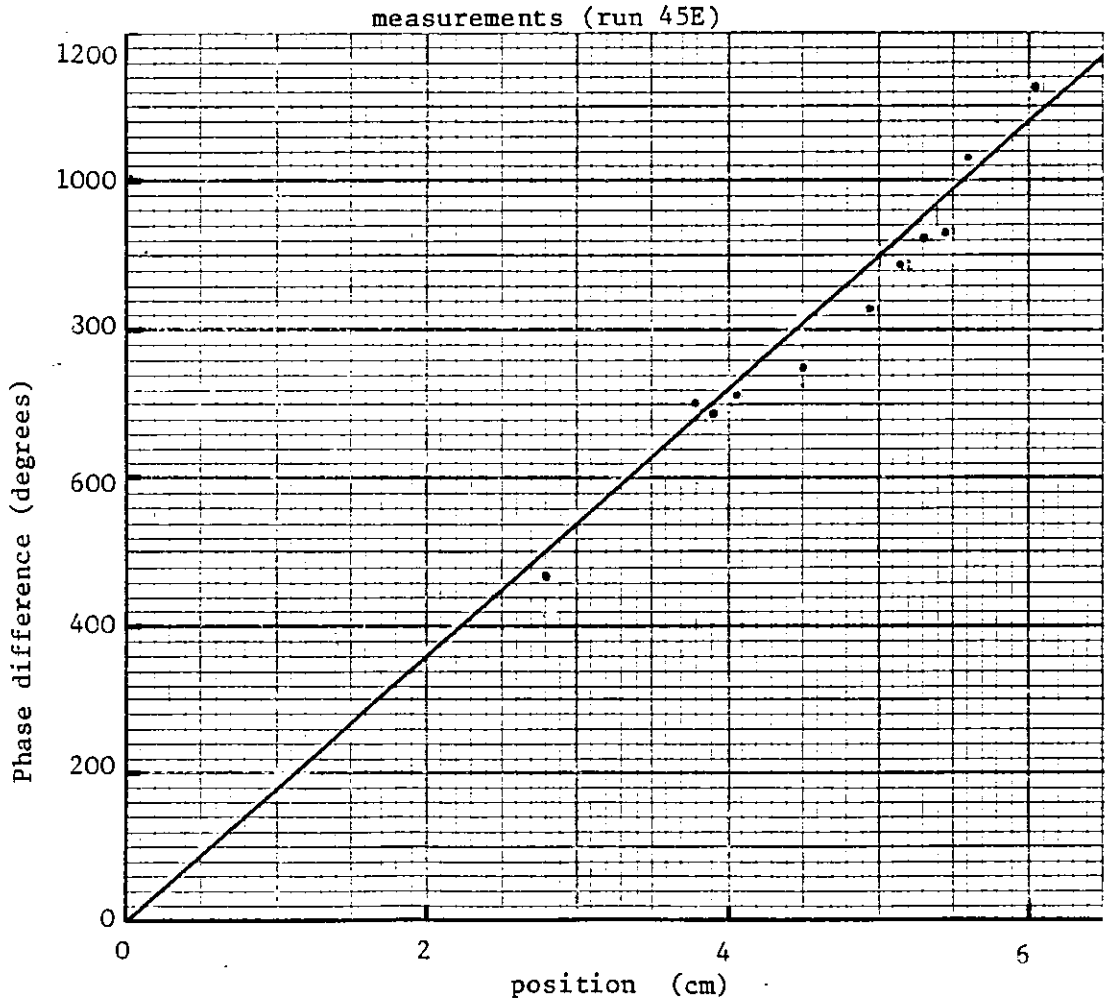

Fig. 6.5 Low confidence estimation of extended retardation measurements (run 51b)

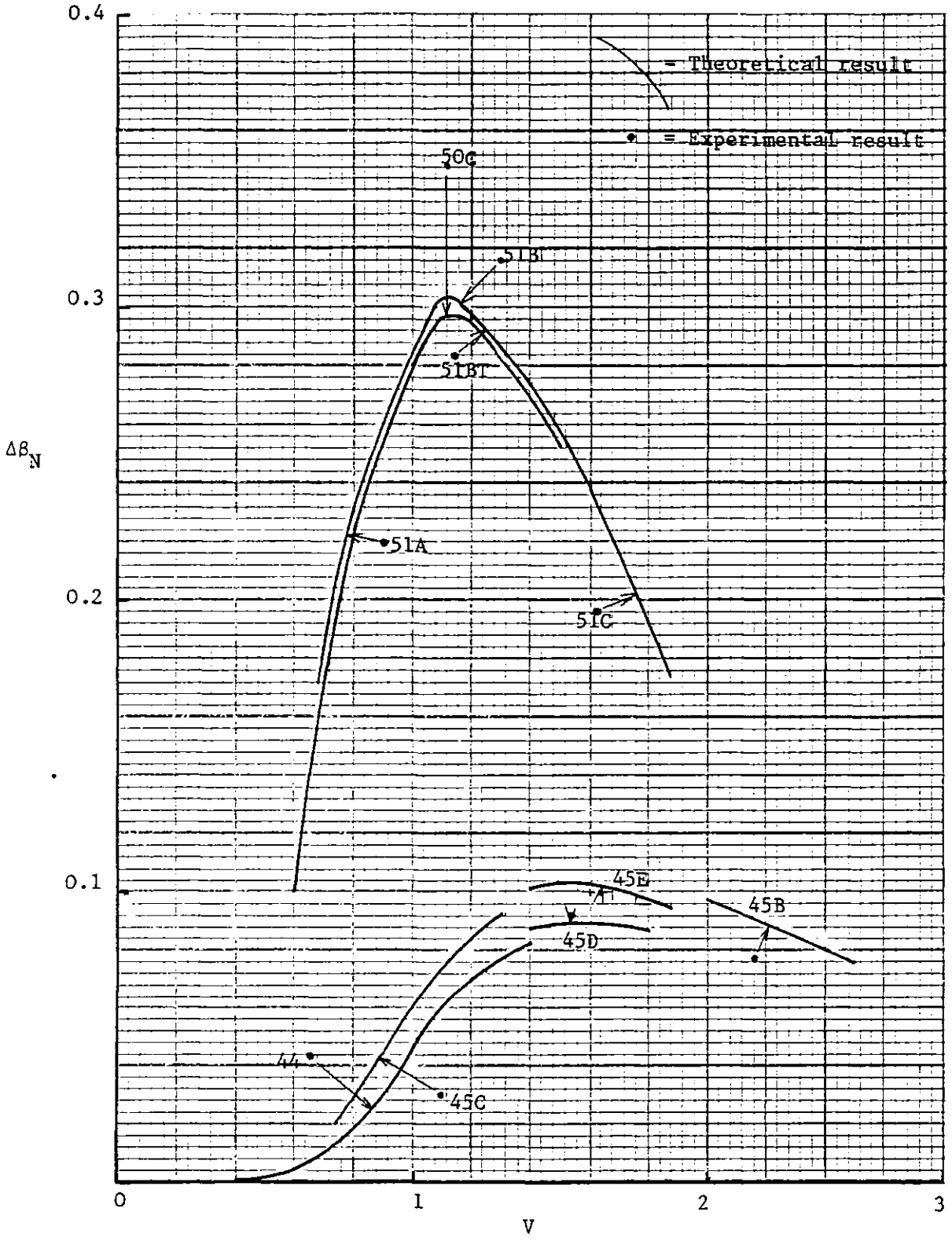

Fig. 6.6 Results of the optical tests of normalised birefringence for various fibres with liquid elliptical cores

The magnitude of $\Delta\beta_N$ agrees well with theory for results 45D, B and E in particular, but the other results are clearly less accurate. It has been explained above that various errors in the simple measurements were not easily quantified but it should be noted that there is no discernible bias in the measured values of $\Delta\beta_N$ in comparison to the theoretically calculated results. When these results are considered alone, this allows us to place some confidence in the computed results, but falls short of a high accuracy confirmation of the exact results of theoretical predictions. However, when the results of the tests on solid core fibres described in chapter four are also considered, it is apparent that the shift in V for peak $\Delta\beta$ remarked upon in that chapter is due to the nature of the solid core fibres tested. The liquid core fibres do not show any clear shift in the $\Delta\beta_N$ curves along the V axis.

With encouragement from these results, it was decided to test using the liquid core fibres the variation of $\Delta\beta$ with Δn for a fixed fibre geometry.

6.3 Optical Test of the Variation of $\Delta\beta$ with Δn

6.3.1 Equipment and Method

It had been noted that the refractive index of the core liquid in a fibre sample was temperature dependent. This is the key characteristic which made the experiment described in this section possible. The fibre identified in the preceding section as 51B was heated in the apparatus shown in figure 6.7 and was allowed to cool back to room temperature. During the heating and cooling operations, which were very slow, readings of phase difference were made on the light emerging from the fibre. These were obtained by the technique described in section 6.2.

The heat source was manually controlled by connecting the soldering iron to the mains through a Variac autotransformer. The glass wool acted as thermal insulation and prevented air convection from

cooling the surface of the glass slide and fibre below the temperature measured by the thermcouple. The large metal block which transmitted heat to the slide served as a comparatively large thermal mass to prevent temperature fluctuations during the experiment.

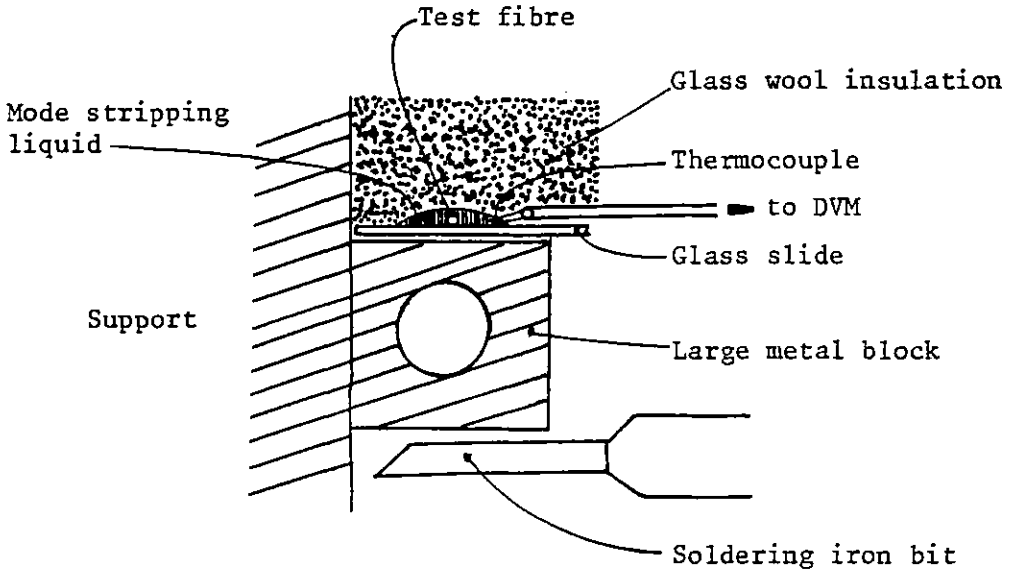

Figure 6.7 Arrangement for heating test fibre

In order to know the index difference of the fibre at different temperatures, it was necessary to measure the temperature dependence of the refractive index of the core liquid. This was achieved by placing a sample of a similar liquid mixture in the Abbé refractometer (Anise oil + Palmarose oil) and employing the integral water jacket to vary the temperature over the necessary range. The results of this preliminary experiment are shown in figure 6.8.

The gradient of this graph gives an index change of -4.3×10^{-4} per degree Celsius rise in temperature.

6.3.2 Results

The experiment was constrained by similar working limitations and errors to those described in section 6.2.3. The measured values are displayed in table 6.3 and compared with a theoretical line in figure 6.9. The value at 19.4° C in the table is taken from an

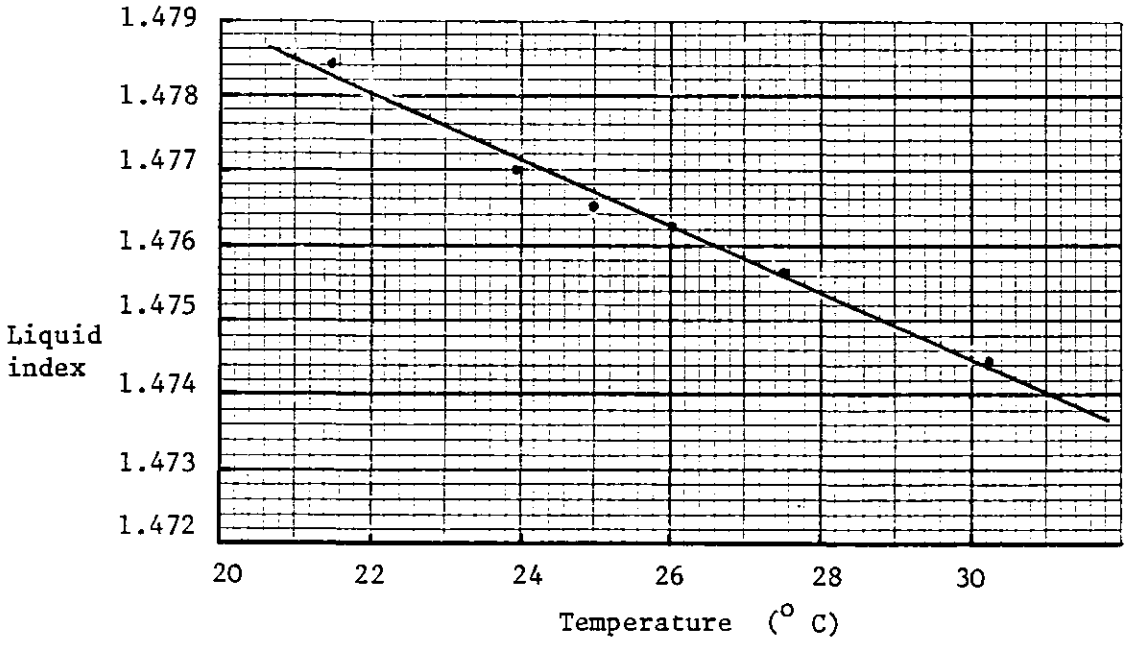

Figure 6.8 Variation of refractive index of Anise/Palmarose Oil mixture with temperature

extrapolation of the $\Delta\beta$ measurement for this fibre and the refractive index at this temperature is taken as the reference from which all other index differences are calculated.

In figure 6.9, the points are the measurements of table 6.3 while the line is calculated from theory, as described below.

Clearly, $\Delta\phi = \Delta\beta.\ell$ where ℓ = fibre length (2.8 cm in this experiment). Hence, using formulae 4.30 and 4.32:

$$\Delta\phi = \frac{\ell\Delta\beta_N}{\lambda_o} 360 \quad (\Delta n)^2 \qquad 6.1$$

Here $\Delta\phi$ is expressed in degrees. Calculations were made by using the calculated Δn from table 6.3 to establish V at that Δn. $\Delta\beta_N$ was then recovered from the theoretical curves and the expression 6.1 was evaluated. Agreement between the calculated and theoretical results is seen from figure 6.9 to be reasonably good over the range and is clearly consistent with the axiom that $\Delta\beta$ is proportional to $(\Delta n)^2$.

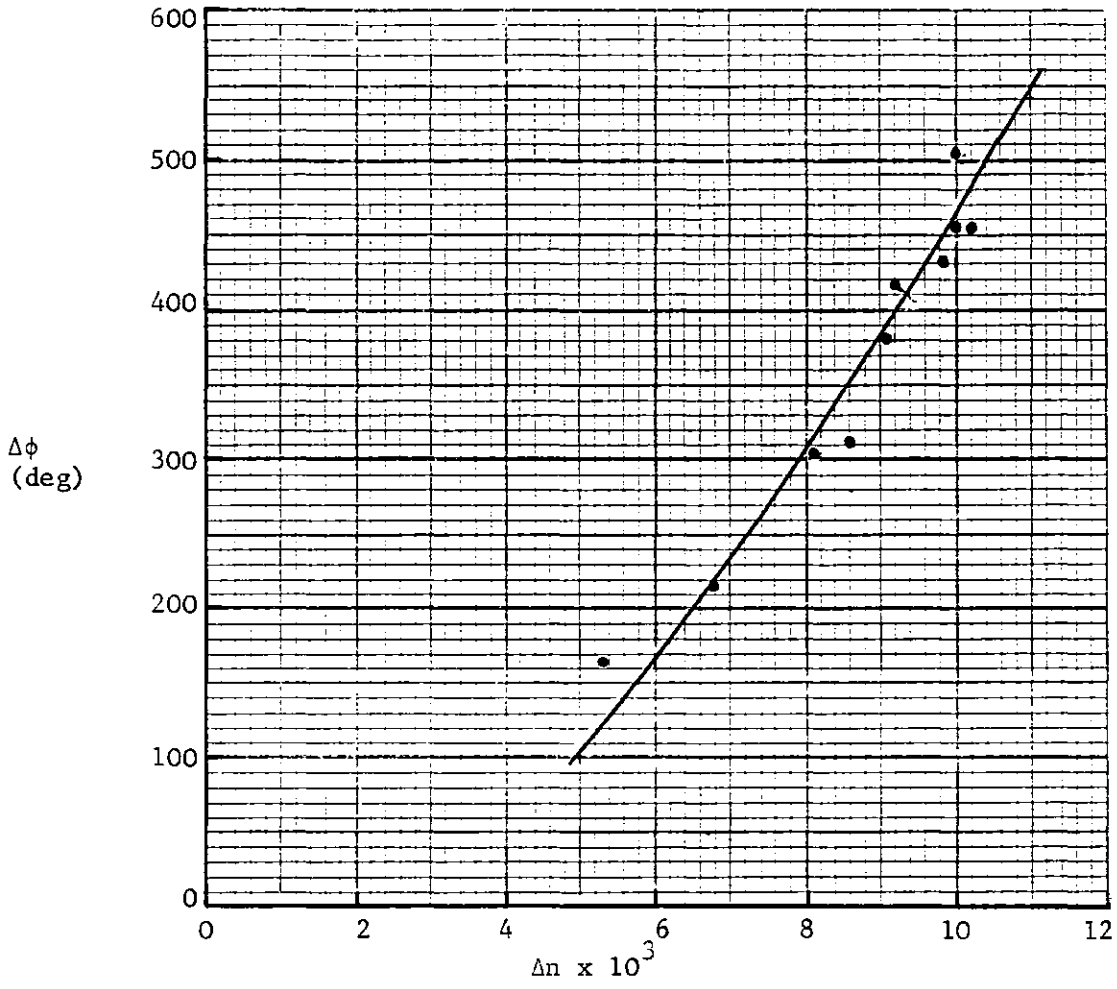

Figure 6.9 Comparison of theoretical and measured phase shifts

Temperature (° C)	Calculated Δn	Phase Shift Δ φ (deg)
18.8	0.0102	454
19.3	0.0100	454
19.4	0.0100	504
19.6	0.0099	432
21.2	0.0092	417
21.3	0.0091	384
22.5	0.0086	313
23.8	0.0081	305
26.9	0.0068	218
30.1	0.0054	168

Table 6.3 Results of phase shift measurement v. temperature

6.3.3 Corroboration of $\Delta\beta_N$ Result

The temperature cycling technique presented here provides an alternative means of establishing absolute phase delay within a fibre. As the fire cools, the index difference increases from a low value, raising the phase delay above π radians. Checking the number of cycles produced until the desired V value is reached provides an absolute measure of the total phase shift between the two fundamental modes. If we regard $\Delta\beta_N$ as an unknown in formula 6.1 and now enter the measured $\Delta\phi$, we have an independent means of checking $\Delta\beta_N$ with reduced error near the middle of the Δn range. Reference to figure 6.9 shows that the phase delays in the region of $\Delta n = 8 \times 10^{-3}$ can be accepted with reasonable confidence of their accuracy. When $\Delta n = 8 \times 10^{-3}$, $V = 1.15$ for fibre 51B, and using formula 6.1 we find that $\Delta\beta_N$ must be 0.285 to produce the observed phase shift. This result is labelled 51BT where it is plotted on figure 6.6 for comparison with the cutback measurements. The agreement is reasonably good for this point, but it was not possible to reliably cycle the fibre over a large range of V to recover the full $\Delta\beta_N$ curve. Further measurements of this type were not made because of practical problems in taking measurements during the temperature cycle.

6.4 Conclusions

This thesis has proposed the use of elliptically cored fibres for polarisation maintenance. Early work with single mode fibre not specifically designed for this purpose (detailed in chapter two) led to this proposal. A detailed consideration of the theoretical aspects of polarisation change has shown that even isotropic ideal single mode fibre is not suitable for maintaining polarisation under bad environmental conditions. As a first step in the development of the elliptically cored polarisation maintaining fibre, effort was directed at predicting and measuring the propagation constants for elliptical guides.

The results given in this chapter show that reasonable confidence can be placed in the calculations of normalised $\Delta\beta$ for the elliptical core fibre when the core is a liquid. The range for which this has been demonstrated covers index differences up to about 2×10^{-2}, ellipticities up to 3 and V values up to 2.2, depending on ellipticity.

It has been shown in earlier chapters through measurements on fibres with solid elliptical cores that similar magnitudes of birefringence can be expected from such fibres, but that performance of these is more variable and may be subject to more subtle effects.

Confirmation of the cut-off conditions for elliptically cored fibres remains undemonstrated. This is an important area for future work, particularly as there has been some dispute concerning these in the literature. (For example, see chapter four, reference 17.)

On the basis of experience gained during the experiments described in this thesis, it is strongly recommended that any further work on elliptically cored fibres should not be made using the liquid core approach. Although performance adequate for checking the propagation constants was secured in these experiments, problems with non-uniformity, fragility and limited length prevent these fibres from being used for more subtle measurements. In addition, the liquid core approach is slow to give results. Apart from these considerations, it is very likely that the more subtle characteristics of elliptically cored fibres (e.g. dispersion, depolarisation performance) will depend crucially on the material properties of the fibres. Since only solid core fibres would have any application, it is important that it is such fibres which are used for future performance tests.

APPENDIX I Measured and calculated results pertaining to the polarisation performance of a length of single mode double crucible drawn fibre

These figures relate to sections 3.1.5 and 3.2

Z cm	R	ϕ degrees	Ω	C	$\frac{dC}{dz}$	S	$\frac{dS}{dz}$	γ	$\frac{d\gamma}{dz} = \omega(z)$ deg. cm^{-1}	r (z) rad m^{-1}	$\theta(z)$ degrees
13	17	105	2.0								
14	13	102	2.2	-3.2	0.6	12.6	-0.9	2.16	0.28	3.9	61.1
15	15	99	2.6	-3.0	-0.2	14.7	+4.1	2.54	0.37	14.3	46.2
16	22	96	3.0	-3.4	-0.7	21.7	+9.3	2.85	0.28	32.6	47.3
17	32	93	3.5	-3.6	1.2	31.8	+9.3	3.13	0.22	14.9	37.2
18	40	88	4.0	-1.4	2.5	40.0	+5.3	3.33	0.21	20.4	32.6
19	45	84	4.5	+1.2	3.2	45.0	+3.8	3.53	0.22	17.3	25.0
20	48	79	5.0	+5.0	4.2	47.8	+2.6	3.77	0.10	17.1	16.0
21	51	74.	5.2	+9.6	5.5	50.2	+1.7	3.75	0.07	20.1	8.6
22	53	67	5.5	+16.0	7.2	50.6	0.0	3.83	0.06	25.0	0.0
23	55	61	5.7								

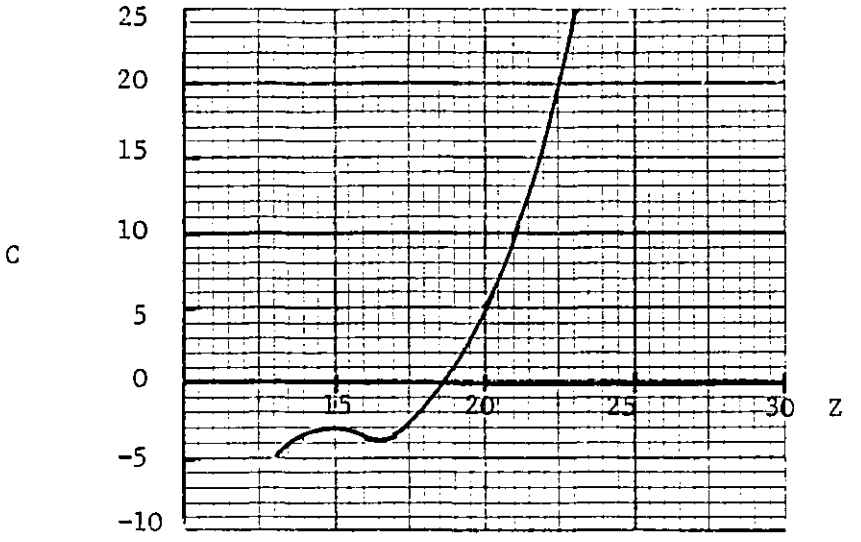

Figure I.1 Variation of C with z

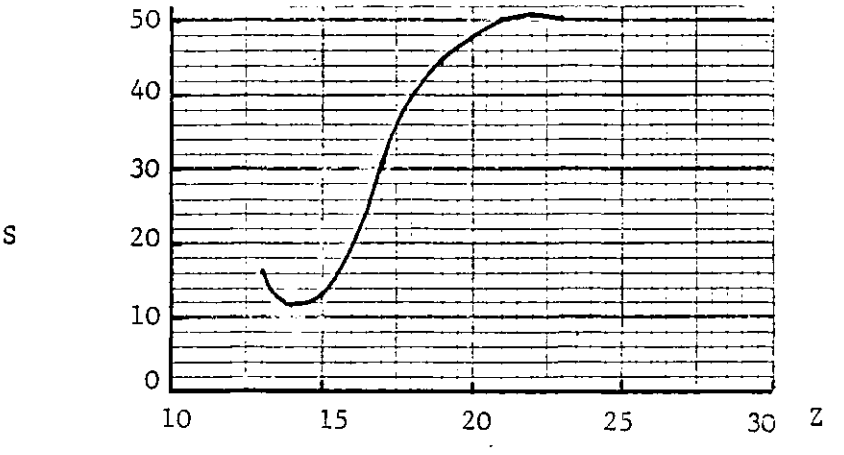

Figure I.2 Variation of S with z

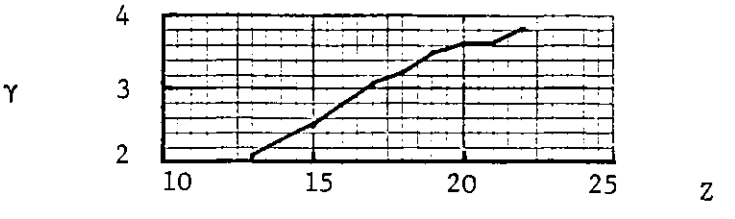

Figure I.3 Variation of γ with z

APPENDIX II

DESCRIPTION OF THE COMPUTER PROGRAM FOR CALCULATING $\Delta\beta$ FOR ELLIPTICALLY CORED FIBRES

(i) Main Program

This reads in the fibre refractive indices RI1 (core index) and RI2 (cladding index) and the ratio of the major/minor core ellipse axes, R. Subroutines are then called to solve the normalised propagation constants of the two orthogonally polarised fundamental modes, BETANO and BETANE, for a range of V from 3.4 down to 0.3 in increments of 0.1. This range is reduced if the program cannot establish the propagation constants to a specified accuracy mentioned later. For each V value the difference, DELBN, between BETANO and BETANE is calculated and printed out together with error parameters, ANSE, ANSO, for the two propagation constants.

(ii) Subroutine ELLIPSE

The purpose of this subroutine is to calculate BETANE and BETANO.

First, a trial value for β is calculated assuming a circular fibre of radius equal to the semi-minor axis of the core ellipse. This is calculated using the Gloge approximation. Since the elliptical core has more high index material than the circular fibre, the true results for both BETANO and BETANE must be lower than this value (i.e. light travels more slowly in the elliptical fibre).

The first trial value for β is substituted into the characteristic equation (reproduced in the FUNCTION subprogram) and the right hand side (which should be zero for correct β) is calculated first for the even mode (specified by MTYPE=1). If the value of the right hand side is non-zero, the current value of β is stored, then U is lowered, lowering β in turn. The calculation is then repeated and the new value of β is stored. This process continues until a sign change occurs in the right hand side of the characteristic equation.

The last two guesses for β are then stored as P and Q to act as limits for an iterative search for the 'exact' β value which is the true root of the characteristic equation. The iterative search is controlled by a library routine available from the operating system. On the Imperial College CDC Cyber 174 machine, the routine C05ACF from the NAG library was used. The end point for the computation is set by the standard parameter ACC, which stops the search when the right hand side of the characteristic equation is less than or equal to ACC. This produces BETANE.

The whole computation is then repeated with the expressions in the FUNCTION subprogram appropriate to the odd mode - selected by MTYPE=2 - finally yielding BETANO.

(iii) FUNCTION F (RR)

This subprogram begins by specifying values for the relevant Mathieu functions (taken from tables). These values are used as reference values from which the NAG library routine E05ADF calculates interpolated values to meet the required arguments for the given case. For values of argument less than one, an alternative calculation of the relevant Mathieu function is made based on a series expression taken from "Theory and application of Mathieu Functions" by N. W. McLachlan (Clarendon Press, Oxford, 1947).

(iv) Subroutines BESJ and BESK

These subroutines return values of the J and K Bessel functions for the ranges of argument and order specified in the comment blocks at the beginning of the respective routines.

(v) Subroutines INUE, IO

These subroutines give the values of the Bessel I_o and I_n functions. These routines, together with the BESJ and BESK routines, are based on routines available from the IBM program library.

```
UNIVERSITY OF MINNESOTA FORTRAN COMPILER (VERSION 5.4 - 79/10/25) ON THE C174 UNDER  N O S 1.1.0 ON 80/01/09 AT 16.27
          MDF5,I=NQVALA,T,6=NQVALB
    1.  0000000B        PROGRAM QVAL(TAPE5,OUTPUT,TAPE6=OUTPUT)
    2.  0031318B        READ(5,*)RI1,RI2,R
    3.  0031378B          DO 200 J1=1,32
    4.  0031410B          V=(35.-FLOAT(J1))/10.
    5.  0031430B        WRITE(6,11)V,RI1,RI2,R
    6.  0031606B  11    FORMAT(/,5X,"V-VALUE=",E15.8,5X,/,5X,"CORE R.I.=",E15.8,/,5X,"
                       +CLADDING R.I.=",E15.8,/,5X,"RATIO=",E15.8,/)
    7.  0031608B        CALL ELLIPSE(V,RI1,RI2,R,BETANE,BETANO,ANSE,ANSO)
    8.  0031638B        DELBN=BETANO-BETANE
    9.  0031646B        WRITE(6,12)BETANE,BETANO,DELBN,ANSE,ANSO
   10.  0032008B  12    FORMAT(5X,"BETANE=",E15.8,5X,"BETANO=",E15.8,5X,"DELBN=",E15.8,
                       +5X,"ANSE=",E15.8,5X,"ANSO=",E15.8,/)
   11.  0032508B  200     CONTINUE
   12.  0032038B        STOP
   13.  0032048B        END
```

```
    1.  0000000B        SUBROUTINE ELLIPSE(A,RIA,RIB,R,BETANE,BETANO,ANSE,ANSO)
    2.  0000008B        EXTERNAL F
    3.  0000308B        COMMON RI1,RI2,V,ANG,MTYPE,MC
C
C     ..................................................................
C     PURPOSE
C        COMPUTE VALUES FOR BETAN OF BOTH EVEN AND ODD HE11 MODES GUIDED
C        BY AN ELLIPTICAL CORED FIBER
C
C     USAGE
C        CALL ELLIPSE(V,RI1,RI2,R,BETANE,BETANO,ANSE,ANSO)
C
C     DESCRIPTION OF PARAMETERS
C        V- V-VALUE OF EQUIVALENT CIRCULAR CROSS-SECTION FIBER HAVING
C        DIAMETER EQUAL TO THE MINOR AXES OF THE ELLIPSE
C        RI1- CORE REFRACTIVE INDEX
C        RI2- CLADDING REFRACTIVE INDEX
C        R- RATIO OF THE MAJOR AXES TO THE MINOR AXES OF THE ELLIPTICAL
C        CROSS-SECTION OF THE FIBER
C        BETANE- COMPUTED VALUE FOR EVEN HE11 MODE
C        BETANO- COMPUTED VALUE FOR ODD HE11 MODE
C        ANSE AND ANSO- GIVE THE ACCURACY OF COMPUTATION OF BETANE AND
C        BETANO RESPECTIVELY. THIS IS DETERMINED BY SUBSTITUTING THE
C        COMPUTED BETAN VALUE INTO THE TRANSCEDENTAL EQUATION.
C
C     METHOD
C        FIRST THE VALUES OF BETAN ARE FOUND WHICH LIE ON EITHER SIDE
C        OF THE ROOT OF THE TRANSCEDENTAL EQUATION , THEN USING
C        SUBROUTINE C05ACF(A,B,EPS,ETA,F,X,IFAIL) OF THE N.A.G.6 LIBRARY
C        THE ROOT(I.E. BETAN) IS CALCULATED
C
C     ..................................................................
```

```
      DO50MTYPE=1,2
      MC=0
      RI1=RIA
      RI2=RIB
      V=A
      ACC=1.0E-08
      ANG=0.5*ALOG((R+1.0)/(R-1.0))
      RI1S=RI1**2
      RI2S=RI2**2
      U=(1.0+SQRT(2.0))*V/(1.0+(4.0+(V**4))**0.25)
      DO1001=1,1000
      BETAN=(RI1S-((U/V)**2)*(RI1S-RI2S))**0.5
      AA=BETAN
      FUN=F(AA)
      IF(I.EQ.1)PREVF=FUN
      IF(FUN)13,14,15
   13 P=BETAN
      IF(PREVF.GT.0.0)GOTO17
      GOTO16
   15 Q=BETAN
      IF(PREVF.LT.0.0)GOTO17

   16 U=U-U*(FLOAT(I)/1000.0)
      PREVF=FUN
  100 CONTINUE
   17 EPS=ACC
      ETA=ACC
      IFAIL=0
      CALL C05ACF(P,Q,EPS,ETA,F,RR,IFAIL)
      IF(IFAIL.EQ.0)GOTO25
      WRITE(6,150)IFAIL
  150 FORMAT(//,25X," IFAIL=",I4)
      GOTO90
   14 AA=BETAN
   25 IF(MTYPE.EQ.1)GOTO220
      BETAND=RR
      MC=1
      ANSO=F(RR)
      GOTO50
  220 BETANE=RR
      MC=1
      ANSE=F(RR)
   50 CONTINUE
   90 RETURN
      END
```

```
1.    0000000B        FUNCTION F(RR)
2.    0000000B         DIMENSION       X2(35),X3(35),X4(35),X5(35),X6(35),Y1(35),Y2(35),Y
     £3(35),Y4(35),Y5(35),Y6(35),W1(35),W2(35),W3(35),W4(35),W5(35),W6(3
     £5),G1(35),G2(35),G3(35),G4(35),G5(35),G6(35),RRA(4),RIB(4),RIC(4),
     £RR0(4),X1(35),W7(35),W8(35),W9(35),W10(35),G7(35),G8(35),G9(35),D1
     £0(35)
3.    0000000B         COMMON R11,R22,V,ANG,MTYPE,MC
4.    0000000B         DATA (X1(J),J=1,31)/0.0,1.0,2.0,3.0,4.0,5.0,6.0,7.0,8.0,9.0,10.0,1
     £1.0,12.0,13.0,14.0,15.0,16.0,17.0,18.0,19.0,20.0,21.0,22.0,23.0,24
     £.0,25.0,26.0,27.0,28.0,29.0,30.0/
5.    0000000B         DATA (X2(J),J=1,31)/0.0,1.0,2.0,3.0,4.0,5.0,6.0,7.0,8.0,9.0,10.0,1
     £1.0,12.0,13.0,14.0,15.0,16.0,17.0,18.0,19.0,20.0,21.0,22.0,23.0,24
     £.0,25.0,26.0,27.0,28.0,29.0,30.0/
6.    0000000B         DATA (X3(J),J=1,31)/0.0,1.0,2.0,3.0,4.0,5.0,6.0,7.0,8.0,9.0,10.0,1
     £1.0,12.0,13.0,14.0,15.0,16.0,17.0,18.0,19.0,20.0,21.0,22.0,23.0,24
     £.0,25.0,26.0,27.0,28.0,29.0,30.0/
7.    0000000B         DATA (X4(J),J=1,31)/0.0,1.0,2.0,3.0,4.0,5.0,6.0,7.0,8.0,9.0,10.0,1
     £1.0,12.0,13.0,14.0,15.0,16.0,17.0,18.0,19.0,20.0,21.0,22.0,23.0,24
     £.0,25.0,26.0,27.0,28.0,29.0,30.0/
8.    0000000B         DATA (X5(J),J=1,31)/0.0,1.0,2.0,3.0,4.0,5.0,6.0,7.0,8.0,9.0,10.0,1
     £1.0,12.0,13.0,14.0,15.0,16.0,17.0,18.0,19.0,20.0,21.0,22.0,23.0,24
     £.0,25.0,26.0,27.0,28.0,29.0,30.0/
9.    0000000B         DATA (X6(J),J=1,31)/0.0,1.0,2.0,3.0,4.0,5.0,6.0,7.0,8.0,9.0,10.0,1
     £1.0,12.0,13.0,14.0,15.0,16.0,17.0,18.0,19.0,20.0,21.0,22.0,23.0,24
     £.0,25.0,26.0,27.0,28.0,29.0,30.0/
10.   0000000B         DATA(Y1(J),J=1,31)/1.0,0.99948078,0.997797415,0.994762441,0.99020
     £2006,0.983974016,0.975980779,0.966811554,0.954718213,0.941626085,0.
     £9271487795,0.9211542898,0.895997662,0.878105937,0.860844074,0.84355
     £0881,0.8264,3024,0.8090682442,0.7933758125,0.7776220592,0.7624263686,
     £0.7479336565,0.7340449321,0.7207078859,0.707867957,0.696138466,0.684
     £68381,0.673775878,0.663385362,0.653482789,0.644039169/
11.   0000000B         DATA(Y2(J),J=1,31)/0.0,-0.032230749,-0.066319917,-0.10216106,-0.13
     £9511475,-0.178047651,-0.217358662,-0.256 6466,-0.29634459,-0.334975
     £0E9,-0.372308603,-0.408107754,-0.441868226,-0.473428867,-0.5026691
     £13,-0.529557082,-0.554132383,-0.576487371,-0.596749608,-0.61506701
     £4,-0.631690318,-0.646894666,-0.659391946,-0.671997281,-0.682877135
     £,-0.692674515,-0.701498949,-0.709443935,-0.716612647,-0.723066798,
     £-0.728887515/
12.   0000000B         DATA(Y3(J),J=1,31)/0.0,0.000339084873,0.001409384 1,0.0032863111,0.0
     £0
     £003319,0.009700561 6,0.014308715,0.019853956,0.026300936,0.0335048
     £07,0.041615769,0.050286223,0.059479.79219,0.0690766 4,0.078966277,
     £0.088954021 ,0.099227989,0.10943 2 ,0.119613301,0.129708321,0.1396
     £84395,0.14951473,0.159177443,0.168658275,0.17794728,0.187038197,0.
     £195927509,0.20461 254,0.21309854,0.221332094,0.229467458/
13.   0000000B         DATA (Y4(J),J=1,31)/1.0,0.999542635,0.998231139,0.996377419,0.99396
     £756,0.991174 3 ,0.988 3477,0.984786 31 ,0.981148305,0.977 13478,0.9
     £74 2 736,0.9756273 2,0.970313 6,0.9634 88,0.95 3 30663,0.95 64577
     £87,0.9503 3 86,0.9496737 6,0.94 3 35 07,0.9431 6374,0.9400 9 2 ,0.9
     £3 4 325 ,0.9339387 ,0.931004 8 ,0.9 2 139839,0.925342769,0.9226118
     £15,0.919945207,0.917341074,0.914797523,0.912312639/
14.   0000000B         DATA (Y5(J),J=1,31)/0.0,-0.030 2 0416,-0.0 522 3 903,-0.085002523,-0.
     £109 8 3791,-0.132432056,-0.153 56902,-0.173372986,-0.19169447,-0.20
     £8752282,-0.224591716,-0.239371304,-0.253162273,-0.266048435,-0.278
     £100 6 6,-0.29 05 190 ,-0.300009891,-0.309976084,-0.319356248,-0.3281
     £97 6 ,-0.336541963,-0.344428547,-0.351892019,-0.358964033,-0.36567
     £3331,-0.372045048,-0.378105969,-0.383874783,-0.389372279,-0.394616
     £56,-0.399624289/
15.   0000000B         DATA (Y6(J),J=1,31)/0.0,0.000311 98 6,0.001194543 ,0.0025703863,0.
     £0043676485,0.006521078,0.008972493,0.011670743,0.01457131,0.01763
     £5777,0.021083118 ,0.024129391,0.027506452,0.031 42053,0.03441901 ,0
     £.037922771,0.041441119,0.045 63 41,0.048481983,0.051988598,0.05547
     £7528,0.059 43735,0.062383041,0.065792 0 ,0.069167802,0.072508154,0
     £.075811225,0.079075571,0.082300072,0.085483893,0.08862664 5/
```

```
      N=29
      IG=N+1
      BETAN=RR
      SB=(BETAN*BETAN-RI2*RI2)/(RI1*RI1-RI2*RI2)
      PI=4.0*ATAN(1.0)
      SANG=SINH(ANG)
      SANGS=SANG**2
      VS=V**2
      GAMMA1S=(VS/(4.0*SANGS))*(1.0-SB)
      GAMMA0S=(VS/(4.0*SANGS))*SB
      GAMMA0=SQRT(GAMMA0S)
      GAMMA1=SQRT(GAMMA1S)
      S0=4.0*GAMMA0S
      S1=4.0*GAMMA1S
      IF(S0.LT.1.)GOTO100
      CALL E01ADF(N,S0,X1,Y1,H1,D1,IG,VAL1)
      A10=VAL1
      CALL E01ADF(N,S0,X2,Y2,H2,D2,IG,VAL2)
      A30=VAL2
      CALL E01ADF(N,S0,X3,Y3,H3,D3,IG,VAL3)
      A50=VAL3
      CALL E01ADF(N,S0,X4,Y4,H6,D6,IG,VAL6)
      B10=VAL6
      CALL E01ADF(N,S0,X5,Y5,H7,D7,IG,VAL7)
      B30=VAL7
      CALL E01ADF(N,S0,X6,Y6,H8,D8,IG,VAL8)
      B50=VAL8
      GOTO110
  100 A10=1.0
      S=S0/16.
      A30=-A10*S*(((S/24.)+(1./4.))*S+(1./2.))
      A50=A10*(S**2)*(((S/96.)+(1./18.))*S+(1./12.))
      B10=1.0
      B30=-B10*S*(((S/24.)-(1./4.))*S+(1./2.))
      B50=B10*(S**2)*(((S/96.)-(1./18.))*S+(1./12.))
  110 IF(S1.LT.1.)GOTO120
      CALL E01ADF(N,S1,X1,Y1,H4,D4,IG,VAL4)
      A11=VAL4
      CALL E01ADF(N,S1,X2,Y2,H5,D5,IG,VAL5)
      A31=VAL5
      CALL E01ADF(N,S1,X4,Y4,H9,D9,IG,VAL9)
      B11=VAL9
      CALL E01ADF(N,S1,X5,Y5,H10,D10,IG,VAL10)
      B31=VAL10
      GOTO130
  120 A11=1.0
      S=S1/16.
      A31=-A11*S*(((S/24.)+(1./4.))*S+(1./2.))
      B11=1.0
      B31=-B11*S*(((S/24.)-(1./4.))*S+(1./2.))
  130 P1=2.0*COSH(ANG)*(GAMMA1S**0.5)
      P2=2.0*SINH(ANG)*(GAMMA1S**0.5)
      D=1.0E-8
      N=0
      CALL BESJ(P1,N,BJ0,D,IE0)
      IF(IE0.EQ.0)GOTO200
      WRITE(6,300)IE0
  300 FORMAT(//,25X," IE0=",I4)
  200 N1=N+1
```

```
      CALL BESJ(P1,N1,BJ1,0,IE1)
      IF(IE1.EQ.0)GOTO201
      WRITE(6,301)IE1
  301 FORMAT(//,25X," IE1=",I4)
  201 N2=N+2
      CALL BESJ(P1,N2,BJ2,0,IE2)
      IF(IE2.EQ.0)GOTO202
      WRITE(6,302)IE2
  302 FORMAT(//,25X," IE2=",I4)
  202 N3=N+3
      CALL BESJ(P1,N3,BJ3,0,IE3)
      IF(IE3.EQ.0)GOTO203
      WRITE(6,303)IE3
  303 FORMAT(//,25X," IE3=",I4)
  203 N4=N+4
      CALL BESJ(P1,N4,BJ4,0,IE4)
      IF(IE4.EQ.0)GOTO204
      WRITE(6,304)IE4
  304 FORMAT(//,25X," IE4=",I4)
  204 CALL BESJ(P2,N,BJ5,0,IE5)
      IF(IE5.EQ.0)GOTO205
      WRITE(6,305)IE5
  305 FORMAT(//,25X," IE5=",I4)
  205 CALL BESJ(P2,N1,BJ6,0,IE6)
      IF(IE6.EQ.0)GOTO206
      WRITE(6,306)IE6
  306 FORMAT(//,25X," IE6=",I4)
  206 CALL BESJ(P2,N2,BJ7,0,IE7)
      IF(IE7.EQ.0)GOTO207
      WRITE(6,307)IE7
  307 FORMAT(//,25X," IE7=",I4)
  207 CALL BESJ(P2,N3,BJ8,0,IE8)
      IF(IE8.EQ.0)GOTO208
      WRITE(6,308)IE8
  308 FORMAT(//,25X," IE8=",I4)
  208 CALL BESJ(P2,N4,BJ9,0,IE9)
      IF(IE9.EQ.0)GOTO209
      WRITE(6,309)IE9
  309 FORMAT(//,25X," IE9=",I4)
  209 CE=A11*BJ1-A31*BJ3
      P1F=(A11*P2/2.0)*(BJ0-BJ2)
      P2F=(A31*P2/2.0)*(BJ2-BJ4)
      CEO=P1F-P2F
      RC=CEJ/CE
      SE=B11*BJ6+B31*BJ8
      P1FD=(B11*P1/2.0)*(BJ5-BJ7)
      P2FD=(B31*P1/2.0)*(BJ7-BJ9)
      SEO=P1FD+P2FD
      RS=SEJ/SE
      SK=SQRT(GAMMA0S)
      U1=SK*EXP(-ANG)
      U2=SK*EXP(ANG)
      CALL IO(U1,BI0)
      CALL INUE(U1,N1,BI0,RIA)
      CALL INUE(U1,N2,BI0,RIB)
      CALL INUE(U1,N3,BI0,RIC)
      CALL INUE(U1,N4,BI0,RID)
      BI1=RIA(N1)
      BI2=RIB(N2)
      BI3=RIC(N3)
      BI4=RID(N4)
```

```
                  CALL BESK(U2,N,BK0,IE15)
                  IF(IE15.EQ.0)GOTO215
                  WRITE(6,315)IE15
  315 FORMAT(//,25X,' IE15=',I4)
  215 CALL BESK(U2,N1,BK1,IE16)
                  IF(IE16.EQ.0)GOTO216
                  WRITE(6,316)IE16
  316 FORMAT(//,25X,' IE16=',I4)
  216 CALL BESK(U2,N2,BK2,IE17)
                  IF(IE17.EQ.0)GOTO217
                  WRITE(6,317)IE17
  317 FORMAT(//,25X,' IE17=',I4)
  217 CALL BESK(U2,N3,BK3,IE18)
                  IF(IE18.EQ.0)GOTO218
                  WRITE(6,318)IE18
  318 FORMAT(//,25X,' IE18=',I4)
  218 CALL BESK(U2,N4,BK4,IE19)
                  IF(IE19.EQ.0)GOTO219
                  WRITE(6,319)IE19
  319 FORMAT(//,25X,' IE19=',I4)
  219 FEK=B10*(BI0*BK1-BI1*BK0)+B30*(BI1*BK2-BI2*BK1)+B50*(BI2*BK3-BI3*B
     &K2)
                  FEKD=(B10/2.0)*(-2.0*U1*BI1*BK1-BI0*(BK0+BK2)*U2+(BI0+BI2)*BK0*U1+
     &2.0*BI1*BK1*U2)+(B30/2.0)*(-1.0*U1*BK2*(BI0+BI2)-BI1*(BK1+BK3)*U2+
     &(BI1+BI3)*BK1*U1+BI2*(BK0+BK2)*U2)+(B50/2.0)*(-1.0*(BI1+BI3)*BK3*U
     &1-BI2*(BK2+BK4)*U2+(BI2+BI4)*U1*BK2+BI3*(BK1+BK3)*U2)
(157) - WARNING ------------------------------------------------------MULTIPLY OR DIVIDE BY 1
                  RFEK=FEKD/FEK
                  GEK=A10*(BI0*BK1+BI1*BK0)+A30*(BI1*BK2+BI2*BK1)+A50*(BI2*BK3+BI3*B
     &K2)
                  SFKD=(A10/2.0)*(-2.0*BI1*BK1*U1-BI0*(BK0+BK2)*U2-(BI0+BI2)*BK0*U1-
     &BI1*2.0*BK1*U2)+(A30/2.0)*(-1.0*(BI0+BI2)*BK2*U1-BI1*(BK1+BK3)*U2-
     &(BI1+BI3)*U1*BK1-BI2*(BK0+BK2)*U2)+(A50/2.0)*(-1.0*(BI1-BI3)*U1*BK
     &3-U2*BI2*(BK2-BK4)-U1*(BI2-BI4)*BK2-U2*BI3*(BK1-BK3))
                  E=GAMMA1S/GAMMA0S
                  IF(MTYPE.EQ.2)GOTO400
                  RIX=RI2
                  RIY=RI1
                  GOTO410
  400 RIX=RI1
                  RIY=RI2
  410 SIDEL=((RI1/BETAN)**2)*RS*RC+E*(((RIX/BETAN)**2)*RC*RGEK+((RIY/BET
     &AN)**2)*RFEK*RS)+(((RI2/BETAN)**2)*(E**2)*RFEK*RGEK)
                  SIDER=(1.0+E)**2
                  F=SIDEL-SIDER
                  IF(MC.EQ.0)GOTO 600
                   GAMMA=(RI1*RI1-BETAN*BETAN)/(BETAN*BETAN-RI2*RI2)
                   IF(MTYPE.EQ.1)GOTO 600
                    OMEGA=(A10*A10*(B10+3*B30+5*B50)*(B10-B30+B50))/(
     &+B10*B10*(A10+A30+A50)*(A10-3*A30+5*A50))
                  DELTA=(RS+GAMMA*RGEK)/((FEK/GEK)*OMEGA*(1+GAMMA))
                  WRITE(6,510)DELTA
  510  FORMAT(5X,"QQQ=",E15.8,/)
                   OMEGA=((B11+3*B31)*A11)/((A11-3*A31)*B11)
                    DELTA=(RS+GAMMA*RGEK)*OMEGA*SE/(C2*(1+E))
                    WRITE(6,520)DELTA
  520      FORMAT(5X,"QQ=",E15.8,/)
                  OMEGA2=(B11+3*B31)/(B11*GAMMA1)
                  OMEGA3=(A10+A30+A50)*(A10-3*A30+5*A50)/(PI*A10*A10*GAMMA0)
                  SE1=SE*OMEGA2
                  GEK1=GEK*OMEGA3
                   SEUGEK=SE1/GEK1
                  WRITE(6,*)SEUGEK
  600  RETURN
                  END
```

```
1.    0000008        SUBROUTINE BESJ(X,N,BJ,D,IER)
                C
                C     ..................................................................
                C
                C     PURPOSE
                C        COMPUTE THE J BESSEL FUNCTION FOR A GIVEN ARGUMENT AND ORDER
                C
                C     USAGE
                C        CALL BESJ(X,N,BJ,D,IER)
                C
                C     DESCRIPTION OF PARAMETERS
                C        X -THE ARGUMENT OF THE J BESSEL FUNCTION
                C
                C        N -THE ORDER OF THE J BESSEL FUNCTION
                C        BJ -THE RESULTANT J BESSEL FUNCTION
                C       D -REQUIRED ACCURACY
                C        IER -RESULTANT ERROR CODE
                C              IER=0 NO ERROR
                C              IER=1 N IS NEGATIVE
                C              IER=2 X IS ZERO OR NEGATIVE
                C              IER=3 REQUIRED ACCURACY NOT OBTAINED
                C              IER=4 RANGE OF N COMPARED TO X NOT CORRECT (SEE REMARKS)
                C     REMARKS
                C        N MUST BE GREATER THAN OR EQUAL TO ZERO. BUT IT MUST BE
                C        LESS THAN
                C        20+10*X-X**2/3        FOR X LESS THAN OR EQUAL TO 15
                C        90+X/2                FOR X GREATER THAN 15
                C
                C     METHOD
                C        RECURRENCE RELATION TECHNIQUE
                C
                C     ..................................................................
                C
2.    0000008        BJ=0.0
3.    0000008        IF(N)10,20,20
4.    0000028     10 IER=1
5.    0000048        RETURN
6.    0000078     20 IF(X)30,33,31
7.    0000128     30 IER=2
8.    0000138        RETURN
9.    0000168     33 BJ=1.0
10.   0000208        RETURN
11.   0000228     31 IF(X-15.0)32,32,34
12.   0000268     32 NTEST=IFIX(20.0+10.0*X-(X**2)/3.0)
13.   0000348        GOTO36
14.   0000358     34 NTEST=IFIX(90.0+X/2.0)
15.   0000428     36 IF(N-NTEST)40,38,38
16.   0000468     38 IER=4
17.   0000508        RETURN
18.   0000538     40 IER=0
19.   0000548        BPREV=0.0
                C
                C     COMPUTE STARTING VALUE OF M
                C
20.   0000558        IF(X-9.0)50,60,60
21.   0000608     50 MA=IFIX(X+6.0)
22.   0000638        GOTO70
23.   0000658     60 MA=IFIX(1.4*X+60.0/X)
24.   0000718     70 MB=N+IFIX(X)/4+2
25.   0000778        MZERO=MAX0(MA,MB)
```

```
                      C
                      CCC     SET UPPER LIMIT OF M
                      C
   25.    0001028B           MMAX=NTEST
   27.    0001038B           DO190M=MZERO,MMAX,3
                      C
                      CCC     SET F(M),F(M-1)
                      C
   28.    0001108B           FM1=1.0E-28
   29.    0001168B           FM=0.0
   30.    0001178B           ALPHA=0.0
   31.    0001208B           IF(M-(M/2)*2)120,110,120
   32.    0001238B       110 JT=-1
   33.    0001258B           GOTO130
   34.    0001278B       120 JT=1
   35.    0001308B       130 M2=M-2
   36.    0001348B           DO160K=1,M2
   37.    0001448B           MK=M-K
   38.    0001458B           BNK=2.0*FLOAT(MK)*FM1/X-FM
   39.    0001518B           FM=FM1
   40.    0001528B           FM1=BNK
   41.    0001538B           IF(MK-N-1)150,140,150
   42.    0001568B       140 BJ=BNK
   43.    0001618B       150 JT=-JT
   44.    0001648B           S=1+JT
   45.    0001658B       160 ALPHA=ALPHA+BNK*S
   46.    0001768B           BNK=2.0*FM1/X-FM
   47.    0002018B           IF(N)180,170,180
   48.    0002028B       170 BJ=BNK
   49.    0002058B       180 ALPHA=ALPHA+BNK
   50.    0002118B           BJ=BJ/ALPHA
   51.    0002138B           IF(ABS(BJ-BPREV)-ABS(D*BJ))200,200,190
   52.    0002208B       190 BPREV=BJ
   53.    0002228B           IER=3
   54.    0002258B       200 RETURN
   55.    0002318B           END

    1.    0000008B           SUBROUTINE BESK(X,N,BK,IER)
    2.    0000008B           DIMENSION T(12)
                      C
                      CCCCCC  ...............................................................
                      CCCCCC
                      CCCCCC  SUBROUTINE BESK
                      CCCCCC
                      CCCCCC  PURPOSE
                      CCCCCC     COMPUTE THE K BESSEL FUNCTION FOR A GIVEN ARGUMENT
                      CCCCCC
                      CCCCCC  USAGE
                      CCCCCC     CALL BESK(X,N,BK,IER)
                      CCCCCC
                      CCCCCC  DESCRIPTION OF PARAMETERS
                      CCCCCC     X -THE ARGUMENT OF THE K BESSEL FUNCTION
                      CCCCCC     N -THE ORDER OF THE K BESSEL FUNCTION
                      CCCCCC     BK -THE RESULTANT K BESSEL FUNCTION
                      CCCCCC     IER -RESULTANT ERROR CODE
                      CCCCCC          IER=0 NO ERROR
                      CCCCCC          IER=1 N IS NEGATIVE
                      CCCCCC          IER=2 X IS ZERO OR NEGATIVE
                      CCCCCC          IER=3 X.GT.170, MACHINE RANGE EXCEEDED
                      CCCCCC          IER=4 BK.GT.10**70
```

```
C
C     REMARKS
C        N MUST BE GREATER THAN OR EQUAL TO ZERO
C
C     METHOD
C        COMPUTES ZERO ORDER AND FIRST ORDER BESSEL FUNCTIONS USING
C        SERIES APPROXIMATIONS AND THEN COMPUTES N TH ORDER FUNCTION
C        USING RECURRENCE RELATION.
C
C     ..................................................................
C
  3.  0000000B      BK=0.0
  4.  0000017B      IF(N)10,11,11
  5.  0000160B   10 IER=1
  6.  0000200B      RETURN
  7.  0000233B   11 IF(X)12,12,20
  8.  0000255B   12 IER=2
  9.  0000278B      RETURN
 10.  0000320B   20 IF(X-170.0)22,22,21
 11.  0000336B   21 IER=3
 12.  0000357B      RETURN
 13.  0000420B   22 IER=0
 14.  0000430B      IF(X-1.0)36,36,25
 15.  0000460B   25 A=EXP(-X)
 16.  0000556B      B=1.0/X
 17.  0000566B      C=SQRT(B)
 18.  0000633B      T(1)=B
 19.  0000648B      DO26L=2,12
 20.  0000678B   26 T(L)=T(L-1)*B
 21.  0001138       IF(N-1)27,29,27
C
C     COMPUTE K0 USING POLYNOMIAL APPROXIMATION
C
 22.  0001158B   27 C0=A*(1.2533141-0.1566642*T(1)+0.08811128*T(2)-0.09139095*T(3)
     &+0.1344596*T(4)-0.2299850*T(5)+0.3792410*T(6)-0.5247277*T(7)
     &+0.5575336*T(8)-0.4262633*T(9)+0.2184518*T(10)-0.06680977*T(11)
     &+0.009189383*T(12))*C
 23.  0001508       IF(N)20,28,29
 24.  0001538   28 BK=C0
 25.  0001568       RETURN
C
C     COMPUTE K1 USING POLYNOMIAL APPROXIMATION
C
 26.  0001608   29 C1=A*(1.2533141+0.4699927*T(1)-0.1468583*T(2)+0.1280427*T(3)
     &-0.1735432*T(4)+0.2847618*T(5)-0.4594342*T(6)+0.6283381*T(7)
     &-0.6632295*T(8)+0.5050239*T(9)-0.2531304*T(10)+0.07880001*T(11)
     &-0.0108241*T(12))*C
 27.  0002138       IF(N-1)20,30,31
 28.  0002178   30 BK=C1
 29.  0002228       RETURN
C
C     FROM K0,K1 COMPUTE KN USING RECURRENCE RELATION
C
 31.  0002248   31 DO35J=2,N
 32.  0002358       CJ=2.0*(FLOAT(J)-1.0)*(C1/X)+C0
 33.  0002438       IF(CJ-1.0E70)33,33,32
 34.  0002468   32 IER=4
 35.  0002508       GOTO34
 36.  0002528   33 C0=C1
 37.  0002568   35 C1=CJ
 38.  0002638   34 BK=CJ
 39.  0002658       RETURN
```

```
                      36 J=X/2.0
                         A=0.57721566+ALOG(B)
                         C=B*B
                         IF(N-1)37,43,37
C
C     COMPUTE K0 USING SERIES EXPANSION
C
                      37 CO=-A
                         X2J=1.0
                         FACT=1.0
                         BJ=0.0
                         DO40J=1,6
                         RJ=1.0/FLOAT(J)
                         X2J=X2J*C
                         FACT=FACT*RJ*RJ
                         BJ=BJ+RJ
                      40 CO=CO+X2J*FACT*(BJ-A)
                         IF(N)43,42,43
                      42 BK=CO
                         RETURN
C
C     COMPUTE K1 USING SERIES EXPANSION
C
                      43 X2J=B
                         FACT=1.0
                         BJ=1.0
                         C1=(1.0/X)+X2J*(0.5+A-BJ)
                         DO50J=2,8
                         X2J=X2J*C
                         RJ=1.0/FLOAT(J)
                         FACT=FACT*RJ*RJ
                         BJ=BJ+RJ
                      50 C1=C1+X2J*FACT*(0.5+(A-BJ)*FLOAT(J))
                         IF(N-1)31,52,31
                      52 BK=C1
                         RETURN
                         END
```

```
                         SUBROUTINE I0(X,RI0)
                         RI0=ABS(X)
                         IF(RI0-3.75)1,1,2
                       1 Z=X*X*7.111111E-2
                         RI0=(((((4.5813E-3*Z+3.607688E-2)*Z+2.659732E-1)*Z+1.206749E0)*Z+3
                        £.0899424E0)*Z+3.515623E0)*Z+1.
                         RETURN
                       2 Z=3.75/RI0
                         RI0=EXP(RI0)/SQRT(RI0)*(((((((((3.92377E-3*Z-1.647633E-2)*Z+2.63553
                        £7E-2)*Z-2.057706E-2)*Z+9.16281E-3)*Z-1.57565E-3)*Z+2.25319E-3)*Z+1
                        £.328592E-2)*Z+3.989423E-1)
                         RETURN
                         END
```

```
 1.    0300000B          SUBROUTINE INUE(X,N,ZI,RI)
 2.    0000000B          DIMENSION RI(100)
 3.    0000000B          IF(N)10,10,1
 4.    0000018B        1 FN=N+N
 5.    0000040B          Q1=X/FN
 6.    0000050B          IF(ABS(X)-5.E-4)6,6,2
 7.    0000110B        2 A0=1.
 8.    0000148B          A1=0.
 9.    0000148B          B0=0.
10.    0000158B          B1=1.
11.    0000168B          FI=FN
12.    0000178B        3 FI=FI+2.
13.    0000246B          AN=FI/ABS(X)
14.    0000260B          A=AN*A1+A0
15.    0000308B          B=AN*Q1+B0
16.    0000330B          A0=A1
17.    0000346B          B0=B1
18.    0000358B          A1=A
19.    0000368B          B1=B
20.    0000378B          Q0=Q1
21.    0000416B          Q1=A/B
22.    0000428B          IF(ABS((Q1-Q0)/Q1)-1.E-6)4,4,3
23.    0000478B        4 IF(X)5,6,6
24.    0000528B        5 Q1=-Q1
25.    0000558B        6 K=N
26.    0000608B        7 Q1=X/(FN+X*Q1)
27.    0000658B          RI(K)=Q1
28.    0000728B          FN=FN-2.
29.    0000738B          K=K-1
30.    0000748B          IF(K)8,8,7
31.    0000758B        8 FI=ZI
32.    0001008B          DO9I=1,N
33.    0001078B          FI=FI*RI(I)
34.    0001148B        9 RI(I)=FI
35.    0001228B       10 RETURN
36.    0001268B          END
```